

PLASMON-ENHANCED WHITE LIGHT GENERATION IN

PHOSPHOR BASED GAN LEDS

BY
WAQAS WASEEM AHMED

A Thesis Presented to the
DEANSHIP OF GRADUATE STUDIES

KING FAHD UNIVERSITY OF PETROLEUM & MINERALS

DHAHRAN, SAUDI ARABIA

In Partial Fulfillment of the
Requirements for the Degree of

MASTER OF SCIENCE

In

ELECTRICAL ENGINEERING

MAY 2014

KING FAHD UNIVERSITY OF PETROLEUM & MINERALS

DHAHRAN- 31261, SAUDI ARABIA

DEANSHIP OF GRADUATE STUDIES

This thesis, written by **Waqas Waseem Ahmed** under the direction his thesis advisor and approved by his thesis committee, has been presented and accepted by the Dean of Graduate Studies, in partial fulfillment of the requirements for the degree of **MASTER OF SCIENCE IN ELECTRICAL ENGINEERING.**



Dr. Mohammad A. Alsunaidi
(Advisor)



Dr. Ali Ahmad Al-Shaiki
Department Chairman



Dr. Hussain Ali Al-Jamid
(Member)



Dr. Salam A. Zummo
Dean of Graduate Studies



Dr. Mohammad A. Gondal
(Member)

Date

27/5/14



© Waqas Waseem Ahmed

2014

Dedicated to my beloved Parents and Siblings

ACKNOWLEDGMENTS

All praise, glory and gratitude is to Allah, the most beneficent, the most merciful.

I express my deep gratitude to my advisor Dr. Mohammad A. Alsunaidi for his conscientious guidance and continuous support throughout my thesis work. I am sincerely grateful to him for providing me a welcoming environment to conduct research and tremendous friendliness.

I am also extremely thankful to my thesis committee members Dr. Hussain Ali Al-Jamid and Dr. Mohammad A. Gondal for valuable suggestions, encouragements and appreciations. I would like to thanks Dr. Boon S. Ooi, KAUST for his kind help, support and appreciations.

I am thankful to my friends and fellow graduate students for providing me a joyful company during my stay at KFUPM. I would also like to thank King Fahd University of Petroleum and Minerals (KFUPM) and Technology Innovation Center (TIC) on Solid State Lighting, KAUST, for supporting this thesis work.

TABLE OF CONTENTS

ACKNOWLEDGMENTS	V
TABLE OF CONTENTS	VI
LIST OF TABLES	IX
LIST OF FIGURES	X
LIST OF ABBREVIATIONS	XII
ABSTRACT	XIII
ABSTRACT (ARABIC)	XV
CHAPTER 1 INTRODUCTION	1
1.1 White light generation approaches	3
1.2 Phosphor and Luminescence	4
1.2.1 Requirement for Phosphor wavelength conversion	6
1.3 LED Modeling Techniques	7
1.4 Literature Review	9
1.5 Thesis Objectives	13
1.6 Thesis Organization	14
CHAPTER 2 THEORITICAL BACKGROUND	15
2.1 Overview of Yellow Phosphor	15
2.1.1 Electron Transition Processes in yellow phosphor	17
2.1.2 Excitation and Emission Spectrum of YAG: Ce³⁺	18
2.2 Working Principle of yellow phosphor converted GaN LEDs	19
2.3 Maxwell’s Equations for light propagation	20

2.4	Material Dispersion Models	22
2.4.1	The Lorentz Model	24
2.4.2	The Drude Model.....	25
2.4.3	The Lorentz-Drude Model.....	26
CHAPTER 3 FINITE DIFFERENCE TIME DOMAIN (FDTD) SIMULATION METHOD		28
3.1	Overview of FDTD	28
3.1.1	Yee's Algorithm	29
3.1.2	Finite Difference expressions for Maxwell's equations.....	30
3.1.3	Grid size, step time and Stability Criterion for FDTD	32
3.2	Auxiliary Differential Equation FDTD (ADE-FDTD)	33
3.3	Total Field /Scattered Field (TF/SF) FDTD Formulation.....	36
CHAPTER 4 MODELING OF YELLOW PHOSPHOR CONVERTED WHITE LEDS..		42
4.1	Modeling of YAG:Ce ³⁺	42
4.1.1	Medium modeling using Lorentzian Function	43
4.1.2	Four Level Rate Equation Model.....	45
4.1.3	Discretization and ADE-FDTD Solution.....	47
4.1.4	Spontaneous emission modeling	49
4.1.5	Emission Line shape.....	50
4.1.6	Luminance Saturation effect Modeling.....	52
4.2	Simulation Results for yellow phosphor converted LEDs.....	54
4.3	Summary and Discussion	63
CHAPTER 5 PLASMONIC STRUCTURES FOR ENHANCED WHITE LIGHT GENERATION.....		64
5.1	Overview of Plasmonics for enhanced field confinement.....	64

5.2 Plasmonics cavities for enhanced field confinement	66
5.2.1 Enhanced Optical Confinement	67
5.3 Scattering Properties of metallic nanoparticles	72
5.3.1 Verification of scattering properties of Silver nanoparticle.....	73
5.4 Metallic nanostructures for enhanced phosphor conversion	76
5.4.1 Silver Rectangular Array Configuration.....	77
5.4.2 Plasmon-enhanced Conversion in phosphor converted GaN LEDs	82
5.5 Summary and Discussion	96
CHAPTER 6 CONCLUSIONS AND FUTURE WORK	97
6.1 Summary.....	97
6.2 Conclusions	99
6.3 Future Work.....	100
REFERENCES.....	102

LIST OF TABLES

Table 4.1 Parameters for rate equation model	55
Table 4.2 Lorentz-Drude parameters for YAG:Ce ³⁺	55

LIST OF FIGURES

Figure 1.1 White Light generation approaches in LEDs.	4
Figure 1.2 Fluorescence and Phosphorescence.....	5
Figure 2.1 Energy Level diagram for free Ce^{3+} ion for YAG: Ce+3 [33].	17
Figure 2.2 Emission and Excitation spectrum of YAG: Ce^{3+} with different Ce^{3+} concentration.....	18
Figure 2.3 Schematic of GaN Chip coated with yellow phosphor.	19
Figure 2.4 Spectral power of phosphor converted white LED.	20
Figure 2.5 Six pole Lorentz Drude Model of Silver metal.	27
Figure 3.1 Yee’s Mesh unit cell.....	30
Figure 3.2 Leap-frog algorithm in time.	31
Figure 3.3 Computation window for TF/SF.	36
Figure 3.4 Flow chart of incorporating TF/SF boundary in general ADE-FDTD algorithm.	41
Figure 4.1 Absorption coefficient of YAG: Ce^{3+}	44
Figure 4.2 Ce^{3+} electron transition accounted in the rate equation model.....	46
Figure 4.3 Spatial location of field components and population densities.	49
Figure 4.4 Schematic of GaN LED coated with yellow phosphor.	54
Figure 4.5 Imaginary part of permittivity of YAG: Ce^{3+}	56
Figure 4.6 Time domain signal of blue source emitted from GaN layer.	57
Figure 4.7 Spectrum of Blue Light Source emitted from GaN layer.....	57
Figure 4.8 Time evolution of N_2 population.	58
Figure 4.9 Amplitude of N_2 as function of emission wavelengths.	59
Figure 4.10 Variation of saturation factor with occupied emission sites.....	60
Figure 4.11 Emission Spectrum of YAG: Ce^{3+} for different occupied Ce^{3+} sites (%) without saturation.....	61
Figure 4.12 Emission Spectrum of YAG: Ce^{3+} for different occupied Ce^{3+} sites (%) with saturation.....	61
Figure 4.13 Output Intensity of YAG: Ce^{3+} for different occupied sites.....	62
Figure 4.14 Output Spectrum of white LED for 5%age occupied sites.....	63
Figure 5.1 Structure of SiO_2 nanoparticles embedded in Ag Film.	66
Figure 5.2 Resonance of Plasmonic cavity.	68
Figure 5.3 Variation of intensity inside plasmonic cavities with position.....	69
Figure 5.4 Intensity profile without the metallic silver film.	70
Figure 5.5 Intensity profile with metallic silver film.....	70
Figure 5.6 Variation of enhancement factor with wavelength.....	71
Figure 5.7 Variation of enhancement factor with interparticle spacing.....	72
Figure 5.8 Time domain signal of modulated Gaussian with cosine.....	75

Figure 5.9 Spectrum of modulated Gaussian with cosine.....	75
Figure 5.10 Scattering Cross-section for 40nm radius single Ag nanoparticle.	76
Figure 5.11 Variation of scattering cross section of silver rectangle with length.....	78
Figure 5.12 Variation of scattering cross section of silver rectangle with height.....	79
Figure 5.13 Variation of scattering cross section with spacing between two silver rectangles.	80
Figure 5.14 Variation of scattering cross section with number of silver rectangles.....	81
Figure 5.15 Optimized Configuration with silver rectangles embedded in phosphor layer.	81
Figure 5.16 Scattering cross section of optimized configuration.	82
Figure 5.17 Structure with silver rectangles for phosphor converted white LEDs.....	83
Figure 5.18 Emission Spectrum of YAG: Ce ³⁺ without saturation and no plasmonic array.	84
Figure 5.19 Emission Spectrum of YAG: Ce ³⁺ without saturation and presence of plasmonic array.	84
Figure 5.20 Emission Spectrum of YAG: Ce ³⁺ with saturation and no plasmonic array.	85
Figure 5.21 Emission Spectrum of YAG: Ce ³⁺ with saturation in presence of plasmonic array.	86
Figure 5.22 Emission Intensity of YAG: Ce ³⁺ with and without plasmonic array.	87
Figure 5.23 Final Output spectrum of white LED without plasmonic array.	87
Figure 5.24 Final Output spectrum of white LED with plasmonic array.	88
Figure 5.25 Comparison of Final Output spectrum of white LED with and without plasmonic array.	88
Figure 5.26 Structure of phosphor converted GaN LED coated with metal doped polystyrene layer.	89
Figure 5.27 Scattering Cross-section of optimized arrangement of silver array in polystyrene media.	90
Figure 5.28 Structure for PS thickness (d) optimization.....	90
Figure 5.29 Spectral power for different PS thickness (d).....	91
Figure 5.30 Emission Spectrum of YAG: Ce ³⁺ without plasmonic array and PS layer. ..	92
Figure 5.31 Emission Spectrum of YAG: Ce ³⁺ with PS layer and no plasmonic array. ..	92
Figure 5.32 Emission Spectrum of YAG: Ce ³⁺ with PS layer and plasmonic array.	93
Figure 5.33 Emission Spectrum of YAG: Ce ³⁺ with saturation in absence of plasmonic array and PS layer.	94
Figure 5.34 Emission Spectrum of YAG: Ce ³⁺ with saturation in presence of PS layer and no plasmonic array.	94
Figure 5.35 Emission Spectrum of YAG: Ce ³⁺ with saturation in presence of PS layer and plasmonic array.	95
Figure 5.36 Comparison of Final Output spectrum of optimized configuration with metal doped PS layer.	96

LIST OF ABBREVIATIONS

LEDs	:	Light Emitting Diodes
GaN	:	Gallium Nitride
YAG:Ce³⁺	:	Cerium (III) doped with Yttrium Aluminum Garnet
FWHM	:	Full Width Half Maximum
SPPs	:	Surface Plasmons Polaritons
FDTD	:	Finite Difference Time Domain
TFSF	:	Total Field Scattered Field
IQE	:	Internal Quantum Efficiency
LSPR	:	Localized Surface Plasmon Resonance
pc-LEDs	:	Phosphor converted Light Emitting Diodes
PS layer	:	Polystyrene layer

ABSTRACT

Full Name : Waqas Waseem Ahmed
Thesis Title : Plasmon-enhanced white light generation in phosphor based GaN LEDs
Major Field : Electrical Engineering
Date of Degree : May 2014

White light emitting diodes (wLEDs) are on the brink of a breakthrough in general illumination, due to their unique properties as compared to conventional lighting sources. Up till now, the main challenges in white LEDs have been to realize high chromatic stability, high luminescence efficiency, and high color-rendering index, which depend considerably on optical light conversion phenomena. The ability of phosphor material for wavelength down conversion has made it possible to explore the novel concepts in phosphor converted white LEDs. In this thesis work, a novel quantum coupled electromagnetic model of most commercially used phosphor Ce^{3+} -doped $\text{Y}_3\text{Al}_5\text{O}_{12}$ is proposed. The electron transition process is integrated using rate equations and the material dispersion and luminance saturation properties are incorporated using Lorentzian and Weibull distribution functions in the proposed model, respectively. Finite Difference Time Domain method (FDTD) is used to numerically solve the coupled model. The resulting FDTD simulator is utilized to study the dynamics of structures consisting of phosphor layer coated on the GaN LED. It is also applied to investigate plasmonic structures for enhanced white light conversion in GaN LEDs. It is found that white light conversion is enhanced significantly via localized surface plasmon resonance by

embedding the silver rectangular array in phosphor layer and also coating the polystyrene doped silver rectangular array on surface of yellow phosphor converted GaN LEDs.

ملخص الرسالة

الاسم الكامل : وقاص وسيم احمد
عنوان الرسالة: استخدام التركيبات البلازمية في انتاج الضوء الأبيض في صمامات الجاليوم الضوئية
التخصص: هندسة كهربائية
تاريخ الدرجة العلمية: رجب 1435 هجرية

من المتوقع ان تشهد تقنية الإضاءة المعتمدة على اشباه الموصلات انطلاقةً قويةً في الأعوام القليلة القادمة متجاوزة كافة تقنيات الإضاءة الأخرى وذلك بسبب خصائصها الفريدة والتميزة. التحدي الأكبر لهذه التقنية هو أن تعطي ثباتا عاليا في لون الضوء الأبيض وشدة إضاءة اعلى. هذه الصفات تعتمد على كفاءة هذه الأجهزة في انتاج الضوء الأبيض من خلال عملية التحويل الضوئي الجزئي من الأزرق الى الأصفر والقائمة على استخدام المواد الفسفورية ومن ثمّ مزج اللونين الأزرق والأصفر.

تعرض هذه الرسالة نموذجا كهرومغناطيسيا كيميا جديدا لدراسة أكثر أنواع اضاءة اشباه الموصلات انتشارا وتداولا في الأسواق. في هذه الدراسة تم التعبير عن عملية التحويل بين الضوء الأزرق والضوء الأصفر عن طريق ربط نموذج ديناميكية انتقال الالكترونات بين مجالات الطاقة في المواد الفسفورية ونموذج توليد ونقل الموجات الضوئية المعتمد على معادلات ماكسويل. تم استخدام طريقة FDTD العددية لحل النموذج المزدوج بشكل عددي. استخدم برنامج المحاكاة الناتج في دراسة كفاءة التحويل الضوئي مع وجود تركيبات بلازمية ناتجة عن وجود جسيمات الفضة النانوية ضمن المادة الفسفورية. وظهرت النتائج إمكانية رفع درجة التحويل الضوئي للون الأصفر مما يشير الى زيادة متوقعة في الضوء الأبيض الناتج.

CHAPTER 1

INTRODUCTION

Over the last few years, light emitting diodes (LEDs) have attracted significant attention in common lighting owing to continuous increase in energy demand that exerted pressure on world energy infrastructure [1]. The phenomenon associated with conventional lighting sources (e.g., flashlight, incandescent light bulb and halogen lamp) result in large energy losses caused by high temperature and large Stokes shifts. It is well acknowledged that the widespread substitute of traditional sources by higher efficiency light sources will lead to a significant reduction in power consumption [2]. In this scenario, white LEDs based light sources provide an alternative way of illumination. These sources have a long list of potential benefits such as small size, energy saving, long operating lifetime, high luminous efficiency and fast switching [3]. To date, the conventional white light sources have nearly approached their physical limit of efficiency, but the desired efficiency of white LEDs has not been achieved yet. Among numerous types of LEDs, GaN based LEDs having blue light emission have attracted attention for development of white LEDs with yellow phosphor. The progress of white LEDs is imperative to expand its use in indoor and outdoor environment. It is predicted that solid state lighting LED technology have a bright future that would lead to replace the existing lighting technologies one day due to its potential market and inherent advantages. However, there are still many issues that need to be further resolved before white LEDs can be used widely for general

illumination. One of major the constraints is how to improve the efficiency of white light with exceptional color quality which mainly depends on the light conversion phenomena. Continuous progress is being made in developing the techniques for white light emission from GaN LEDs. Phosphor materials are considered one of the most optimal solutions for conversion of blue light in GaN LEDs into white light using wavelength down conversion phenomena. In addition to the originally emitted blue light, such phosphors have the ability to emit the necessary red, green or yellow light required for a sun like spectrum. The evolution of highly efficient next generation solid state white LEDs require the discovery of novel down conversion phosphor materials with high photoluminescent quantum yield and thermal stability [4]. Substantial research efforts have been exerted on the development of new phosphor materials due to their importance in solid state lighting technology.

Theoretical understanding of the process of white light generation with numerical modeling of the wavelength down conversion process using phosphor is necessary to study the dynamics of phosphor converted white LEDs. The fundamental physical insights offered by theoretical models can be numerically solved to guide the development of efficient phosphor layers in order to improve the optical proprieties of semiconductor devices. The numerical modeling of underlying physics of light propagation in phosphor materials plays an important role in evolution of new structures, improvement of existing designs and exploring the novel concepts in phosphor converted white LEDs. In this work, the modeling of wavelength down conversion process using yellow phosphor (YAG:Ce³⁺) along with enhanced light conversion using plasmonic structure in GaN LEDs is investigated.

1.1 White light generation approaches

In general, three different approaches are used to produce white light using light emitting diodes as illustrated in Figure 1.1.

1. At least three (red, green, blue) monochromatic LEDs are combined in an appropriate way such that power ratios are adjusted to produce white light with specific temperature. This technique is useful for small light sources which can adapt their emission color and intensity as desired by the user. The demerits of this approach are complex geometry and spectral shifts differences among the different colors.
2. Ultraviolet LED is used to excite the red, green and blue phosphor to obtain white light. This technique is based on multi emitting center phosphor and faces certain limitations due to unavailability of green phosphor in nature.
3. Blue (GaN) LED is used to pump the yellow phosphor to yield white light. The blend of yellow and blue light creates the white light. This scheme is based on single emitting center phosphor YAG:Ce^{3+} and mostly used in commercial white LEDs.

The latter two methods employ the phosphor as wavelength down conversion luminescent materials for generating white light in LEDs. Although there are pros and cons of each strategy, the first two approaches are not commonly used due to certain inherent problems e.g. efficient green phosphors are not common in nature so this

restrains the 3-LED approach and UV with full down conversion is not efficient due to large stoke shift.

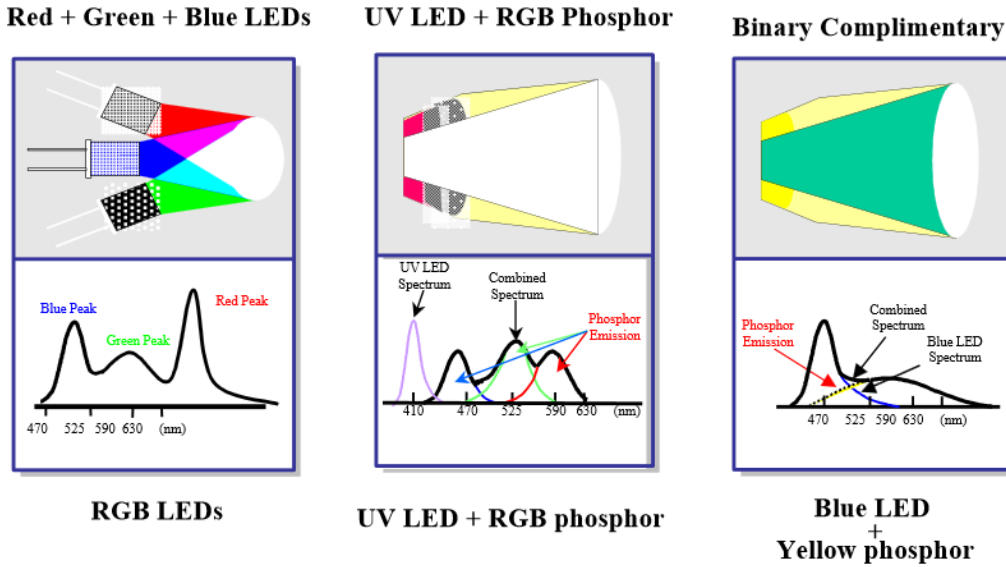


Figure 1.1 White Light generation approaches in LEDs.

1.2 Phosphor and Luminescence

Phosphors, also known as luminescent materials, exhibit the phenomenon of luminescence. Eilhard Wiedemann, a German physicist, used the term ‘Luminescence’ for the first time in 1888 to describe light emission from phosphors under appropriate excitation [5]. Luminescence can be broadly classified into phosphorescence and fluorescence on the basis of decay time as shown in Figure 1.2. The phenomenon of fluorescence takes short decay time for emission in the range of $\sim 10^{-9}$ to 10^{-7} s, whereas longer decay time ($> 1\text{ms}$) is associated with phosphorescence for emission [6]. According to quantum theory, the spin direction of electron does not change in singlet

excited state and transition occurs from the singlet state in fluorescence process. On the other hand, in a phosphorescence process, energy is trapped in triplet state due to change in electron spin. The selection rules consider the triplet state as kinetically unfavorable and forbid the electron transitions from it. Thus, electrons progress at considerably slower time scales with low intensity compared with fluorescence.

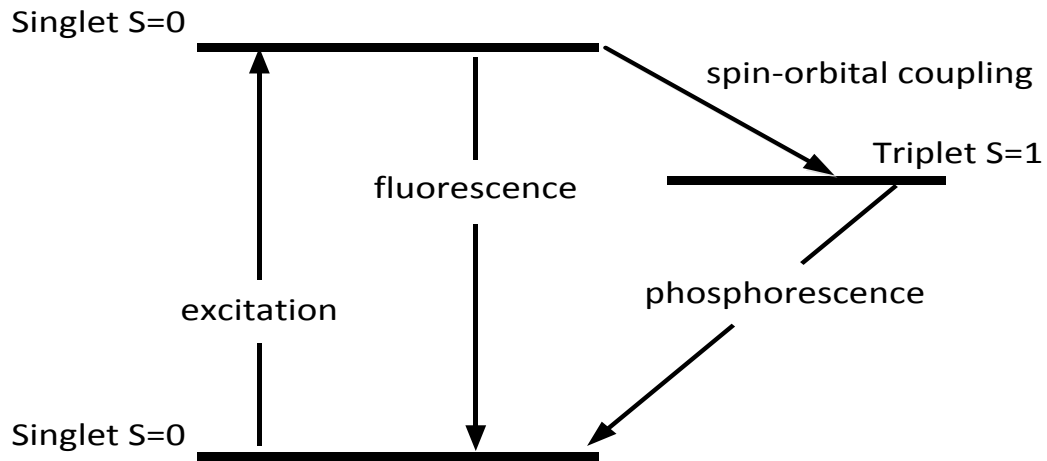


Figure 1.2 Fluorescence and Phosphorescence.

Most of the phosphor materials are organic in nature consisting of dopant, also known as activator, and host crystal. The host crystals are mostly oxide, halide, nitride, oxynitride and oxyhalide selected on the basis of wide band gaps and other key features. The dopants are emissive centers which are normally rare earth and transition metals ions. The incident electromagnetic energy is absorbed by these materials and emission occurs due to intentionally created inhomogeneities in host lattice by addition of dopant. The emission wavelength is dependent on dopant and the surrounding crystal structure [7]. The emitted light usually covers the visible region but it can also fall in the invisible region depending upon the dopant and crystal structure. But the phosphors having emission in the visible spectrum (400 nm-700 nm) are more considered at commercial

level. This fact can be described on the basis of human eye sensitivity to the visible spectrum between 400 nm and 700 nm. Phosphors can be found both in crystalline and amorphous form in nature but it is reported that the quantum efficiencies of crystalline structures are normally higher as compared to amorphous hosts [8].

Phosphors have found extensive application in new areas in last few years. It is mostly used in lighting and display devices, optical amplifiers, X-ray detector systems, solar cells and white-light-emitting LEDs. The properties of phosphors are defined in terms of quantum efficiency, color coordinates, and color temperature for practical lighting and display devices.

1.2.1 Requirement for Phosphor wavelength conversion

Phosphor wavelength conversion is the most popular method for producing white Light in LEDs. There are few phosphor materials recognized as being appropriate for wavelength conversion process. The main performance requirements which must be satisfied for color conversion phosphors are:

- The resulting emission spectrum including the emission of the other components (LED, other phosphors), should produce a pure white emission with a specific color rendering and color temperature.
- The excitation spectrum should be well matched with the pumping LED and have large absorption strength at pumping wavelength.

- The increase in temperature should not affect the emission spectrum, excitation spectrum and quantum efficiency.
- The quantum efficiency should approach unity in order to maximize the overall electrical-to-optical conversion efficiency of the phosphor converted LED.
- The material should show an excellent chemical and temperature stability.
- The phosphor should not show saturation effects for high excitation intensity.

Phosphor should be carefully evaluated keeping in view of above-mentioned parameters for commercial applications. The failure in any one of the above requirements will restrict the phosphor usage in practical applications.

1.3 LED Modeling Techniques

In recent years, continuous efforts have been dedicated to micro and nano fabrication techniques of complex semiconductor devices. These techniques are complicated and their setup incurs huge cost. In this situation, an accurate modeling of semiconductor devices is indispensable for design and optimization, prior the actual fabrication of devices. The modeling of these devices provides an efficient way for reliable design and subsequent optical analysis. The analytical techniques developed in the past are not adequate to model modern devices due to arbitrary geometry. This limitation of analytical methods has made it impossible to optimize the design of such devices. Therefore, numerical techniques provide an alternative way to model the semiconductor devices. It

is found that the results of numerical techniques are more consistent with experiments since it can approximate the exact solutions. In fact, the numerical realization of these devices plays a significant role in industrial development cycle and also affects the behavior of optoelectronic systems. Despite high computational capability, a particular method can be applied to specific class of problems. Therefore, it is crucial to simulate and model the device for appropriate method for optical analysis.

In semiconductors modeling, numerical techniques have been successfully employed for investigating the light matter interaction in LEDs. The performance of LEDs is examined through these techniques to make an optoelectronic system more reliable and efficient. In literature, many numerical techniques have been used to model the light emitting diodes such as Monte Carlo ray-tracing technique, FEM, BPM, FDTD etc. The light extraction characteristics of LEDs were modeled using Monte Carlo techniques as reported in [9]. Monte Carlo ray tracing method provides an appropriate way to simulate and study the ray propagation, light distribution and light extraction efficiency in LEDs dies. In [10], the finite element method was employed to investigate heat dissipation and generation and the current flow paths that can improve the performance of GaN LEDs. This method is extensively used for modeling the complex geometries and irregular boundaries with various element sizes. In [11], Beam propagation method (BPM) was used to study the extraction efficiency of GaN LEDs using 2D periodic metal dielectric patterns. BPM method is more useful in simulating the propagation of light in integrated and fiber-optic photonic devices. Finite Difference Time domain (FDTD) technique is also applied to simulate the GaN LEDs as reported in [12]. This method has many advantages as compared to other computational techniques such as robustness, efficiency, ease of

implementation, etc. Therefore, we will focus on the FDTD method for simulating the yellow phosphor converted GaN LED in this thesis work.

1.4 Literature Review

Solid-state semiconductor lighting technology has made a great progress since the invention of the first semiconductor diode laser by Hall in 1962 [13]. In the past, the applications of semiconductor lasers in lighting were limited due to the fact that its emission wavelengths have usually been beyond visible range. However, Shuji Nakamura's invention of InGaN/GaN blue LED chips in 1994 has made it possible to expand the LED applications in commercial sector [14]. The invention of blue LED paved the way to create white light LED for general illumination. The optical conversion process for white LEDs can be carried out by different methods. In 1996, Nichia Corporation developed the first commercial white LED by combination of InGaN diode chip and the yellow phosphor (YAG: Ce³⁺). The properties of YAG:Ce³⁺ phosphor were investigated first time by Blasse and Brill as reported in [15].

Phosphors have been a subject of very detailed investigations in the context of wavelength conversion in many lighting and display systems [16]. This promoted the rapid development of single and multi-color phosphor materials for light conversion process in LEDs. Rare earth based phosphors were mostly employed in pc-LEDs because of excellent luminescent properties. The dynamics of phosphor materials can be represented by energy levels and electron transition processes. Many studies have been done in literature to model the energy transition. The first insight to model the transition

processes between different energy level in a medium was given by Nagra and York [17]. In this paper, population dynamics of gain and absorbing medium were presented in semi classical rate equation model. The dynamics of spontaneous emission and light amplification has been investigated in silicon based photonics devices using quantum coupled rate equation model [18]. The numerical FDTD modeling of laser based on microstructures was reported in [19]. This paper discusses the introduction of spontaneous emission phenomena in Maxwell equations in terms of the external current density function. It also explains that the optical pumping can be added into rate equation model using medium polarizability. The coupled Maxwell-Bloch equations were used to model the nonlinear gain dynamics of semiconductor microcavities and optical slab waveguide based on FDTD method in [20] . This paper presents the inclusion of spontaneous emission in Maxwell equations by random fluctuation electric field term. A steady state theoretical model for wavelength down conversion process based on Pr^{3+} - Yb^{3+} co-doped fluoride glasses was presented by rate equations and propagation equations to improve solar cell efficiency [21]. In [22] the multicolor phosphor blends excited by ultraviolet light were modeled theoretically by combining the emission and absorption processes with spatial distribution of light intensity. The emission and absorption processes among different energy levels are represented by rate equations while a differential equation is used to represent spatial distribution of light intensity. This steady state model can be utilized in developing the phosphor converted white LED with arbitrary designed light output. A theoretical model of Tb^{+3} - Eu^{+3} - Tm^{+3} co-doped system was reported under 359 nm excitation for generation of white light [23]. In this paper, electron transition processes, energy levels, and power and rate equations of

propagation were used for calculating the fluorescence intensity. Another similar theoretical model of multi rare earth co-doped system ($\text{Yb}^{+3}\text{-Er}^{+3}\text{-Tm}^{+3}$) under 980 nm excitation for generation of white light was presented by Xu et al. [24]. This model is also based on the rate equations of transition processes between different energy levels. YAG: Ce^{3+} phosphor mixed with SiO_2 particles has been modeled analytically as reported in [25]. This paper discusses the optical properties of YAG: Ce^{3+} phosphor including the absorption coefficient, scattering coefficient, asymmetry parameters calculated using Mie scattering theory. It is found that these parameters play a vital role in describing the characteristics of white LED. The optical performance parameters of YAG: Ce^{3+} phosphor calculated by Monte Carlo ray tracing and Mie theory were also reported in [26].

In the last two decades, a lot of research has been conducted to enhance device efficiency and achieve desirable emission color by incorporating different phosphor materials for optical light conversion in GaN LEDs. However, there are some inherent losses associated with LED efficiency such as the difficulty to extract the generated photons and inherent low internal quantum efficiency. The rapid development of phosphor materials for light conversion process in LEDs has made it possible to overcome the color emission and IQE efficiency problems to some extent but still there is need to develop different ways to enhance the efficiency of LEDs. Several techniques have been reported in literature to enhance the emission of LED such as corrugated microstructures, micro-lenses, photonic crystals, nano-gratings, and so on [27]. There are still some challenging issues to use these methods in subwavelength structures. However, Plasmonics offers a unique way of manipulating light in this scenario. Okamoto et al. proposed plasmonic

based InGaN LEDs for the first time to enhance the efficiency of QW based LEDs using Surface plasmon polaritons (SPPs) in 2004 [28]. The resonant behavior of the metallic nanostructures at optical frequencies can be used to enhance the emission characteristics of LEDs. In addition, localized surface plasmon resonances provide a way to enhance light emission via near field interactions and local field enhancement. Plasmonic arrays consisting of aluminum particles showed approximately 60-fold and 70-fold emission enhancements for unpolarized and p-polarized light respectively [29]. Silver nanostructures with ITO grating layer were used to enhance the extraction efficiency of GaN LED three times due to LSP coupling of evanescent field with GaN/ITO interface as reported in [30]. In this thesis, we will use different plasmonic structures to enhance the white light generation and emission in GaN LEDs.

To this point, most of the references on white light generation mainly discussed the different techniques for fabrication of phosphor materials rather than modeling. Most of the presented phosphor models in literature are steady state or analytical which are unable to give physical insight for white light generation process. Due to the importance of phosphor materials for white light generation, a time domain electromagnetic model must be developed for optimizing the design of phosphor converted LEDs. To best of my knowledge, the presented time domain model for the electrodynamics of phosphor material is novel. In this work, we are focused on modeling the YAG:Ce³⁺ based phosphor converted LEDs using the FDTD method.

1.5 Thesis Objectives

The main contribution of this work is to formulate and numerically solve a quantum coupled electromagnetic model representing the electrodynamics of YAG:Ce³⁺ phosphor. It is used to investigate the plasmonic structures for enhanced conversion of light in GaN LEDs. The specific objectives are as follows:

- To perform an extensive literature survey on white light generation using phosphor materials associated with blue GaN LEDs
- To develop a time domain model representing the wavelength down conversion phenomena based on phosphor material. The model also includes spontaneous emission and saturation effect due to density of dopant.
- To develop a 2D-EM simulator that accounts for optical light conversion and spontaneous emission utilizing the ADE-FDTD technique.
- To use the developed simulator to analyze different plasmonic structures for enhanced white light conversion in white LEDs
- To extract important conclusions regarding the white light generation phenomena and their potential applications.

1.6 Thesis Organization

This thesis is organized as follow:

- Chapter 1 describes the fundamental concepts of white light generation in light emitting diodes and also defines the objectives of the thesis.
- Chapter 2 describes the basic theory of phosphor converted white LEDs and also provides the theoretical background of electromagnetic modeling.
- Chapter 3 elucidates Auxiliary Differential equation FDTD method to solve Maxwell's equations based on Yee's Algorithm. It also enlightens the addition of dispersive properties of material and Total field scattered field (TF/SF) boundary conditions in ADE-FDTD
- Chapter 4 explains the rate equation modeling of YAG:Ce³⁺ phosphor material. It also discusses how line shape models and saturation effects are incorporated in the proposed model.
- Chapter 5 discusses plasmonic structures for enhanced electromagnetic field and also sheds light on the enhancement of light conversion process in white LEDs using metallic nanostructures.
- Chapter 6 contains the conclusions and the possible extensions of this thesis as future work.

CHAPTER 2

THEORITICAL BACKGROUND

In this chapter, the basic theory of yellow phosphor will be discussed by presenting the emission and absorption properties of YAG:Ce³⁺. The chapter highlights the importance of yellow phosphor in general illumination and explains the working principle of the phosphor converted white LEDs. The basic concepts of electromagnetic modeling using Maxwell's equations will also be introduced in this chapter.

2.1 Overview of Yellow Phosphor

Cerium (III) doped YAG is a phosphor material firstly used by Nichia Corporation as down conversion phosphor for white light generation in GaN LEDs [13]. The properties which make YAG:Ce³⁺ a suitable candidate for white LEDs are given below:

- YAG: Ce³⁺ has a very broad emission spectrum due to the spin orbital splitting of ground state of Ce³⁺. The FWHM of yellow phosphor is typically 100 nm which covers visible range sensitive to the human eye. The white light is generated in higher Color Correlated range as combination of its yellow emission color and part of the blue emission from the pumping LED.
- YAG:Ce³⁺ has a broad excitation spectrum near 460 nm. It can easily be excited by the blue pumping LED due to good overlap with the LED's emission

spectrum. It has high absorption strength due to spin-allowed 4f-5d energy transition. It has also relatively high optimum dopant concentration of about 5% before concentration quenching.

- The quantum efficiency obtained from YAG:Ce³⁺ is more than 90% which is essential for the fabrication of efficient LED.
- It exhibits an excellent chemical stability and, as a result, phosphor converted LEDs do not undergo any deterioration under high excitation fluxes.
- It shows an excellent thermal quenching behavior and, as a result, emission spectrum of phosphor converted LEDs do not change significantly at high temperature.

Although YAG:Ce³⁺ is a good candidate for phosphor converted GaN LEDs, the main problem of yellow phosphor lies in the lack of emission in the red part of the visible spectrum. The red-shift can be introduced in the emission spectrum by adding the Gd³⁺ or Tb³⁺ [31], while the emission spectrum is blue-shifted by substituting some Al³⁺ sites by Ga³⁺ in the lattice [32]. Some other dopants can also be added in YAG:Ce³⁺ to include the red part in the emission spectrum. Therefore, the more efficient emission can be obtained by adding relatively narrow-emitting rare earth ions.

2.1.1 Electron Transition Processes in yellow phosphor

The electrodynamics of phosphor material can be described by the electron transitions among different energy levels. The energy level diagram of free Ce^{3+} and YAG: Ce^{3+} is shown in the Figure 2.1. The ground state demonstrates a spin orbital splitting into two states, namely $^2F_{5/2}$ and $^2F_{7/2}$ that are associated with $4f^1$ electronic configuration of free Ce^{3+} ion with energy separation of 2000 cm^{-1} . The incorporation of Ce^{3+} ions in host inorganic material (YAG) decreases energy of 5d excited state as compared to free Ce^{3+} ion. The decrease in energy is attributed to phenomenon of crystal field splitting and centroid shift. Therefore, the composition of Ce^{3+} in host material plays a vital role in determining the emission and excitation wavelength of phosphor material. Two lower energy levels of $^2D_{3/2}$ and $^2D_{5/2}$ states are formed due to crystal field splitting. The stoke shift is obtained upon the excitation of electron from 4f to 5d resulting in different absorption and emission wavelengths.

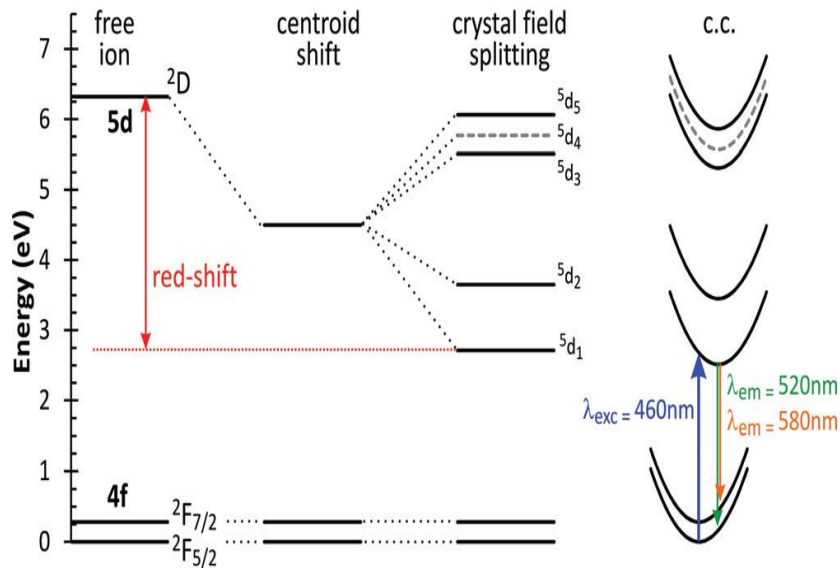


Figure 2.1 Energy Level diagram for free Ce^{3+} ion for YAG: Ce+3 [33].

2.1.2 Excitation and Emission Spectrum of YAG: Ce³⁺

The emission and excitation spectra for YAG:Ce³⁺ is shown in Figure 2.2. It is found that excitation peaks at 338 nm and 460 nm are associated with $^2F_{5/2} \rightarrow ^2D_{3/2}$ and $^2F_{5/2} \rightarrow ^2D_{5/2}$ transitions respectively. The electrons on the energy level of $^2D_{5/2}$ state would relax to $^2D_{3/2}$ state through electron-phonon interaction phenomenon. As a result, the emission band is associated to $^2D_{3/2} \rightarrow ^2F_{7/2}$ or $^2F_{5/2}$ transitions.

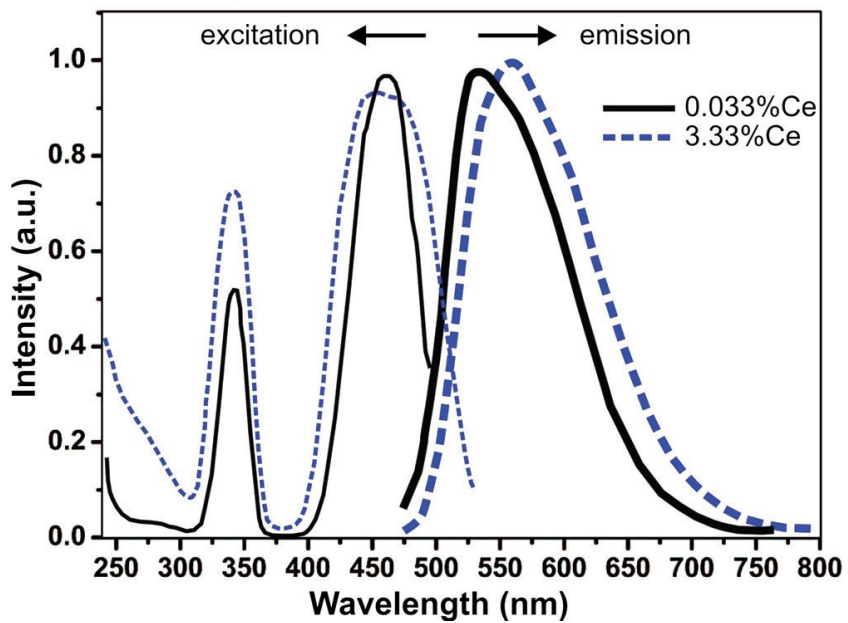


Figure 2.2 Emission and Excitation spectrum of YAG:Ce³⁺ with different Ce³⁺ concentration.

2.2 Working Principle of yellow phosphor converted GaN LEDs

The commercially available white LEDs are produced by coating the surface of blue GaN LED chip with down converting phosphor (YAG:Ce³⁺) layer. The basic principle is based on absorption of blue light and re-emission of yellow light. The structure of blue GaN LED with YAG: Ce³⁺ layer to produce white light is shown in the Figure 2.3. It is well known that yellow phosphor has strong absorption near 460 nm which is well matched with emission wavelength of GaN LED. Part of the blue light emitted from the GaN LED chip coated with yellow phosphor layer is absorbed by YAG:Ce³⁺ layer and the rest of the blue light propagate in air. Phosphor layer converts the absorbed light into yellow light and re-emits it. The un-absorbed blue light from GaN LED will combine with re-emitted yellow light from phosphor to give a radiance of white light as illustrated in Figure 2.4.

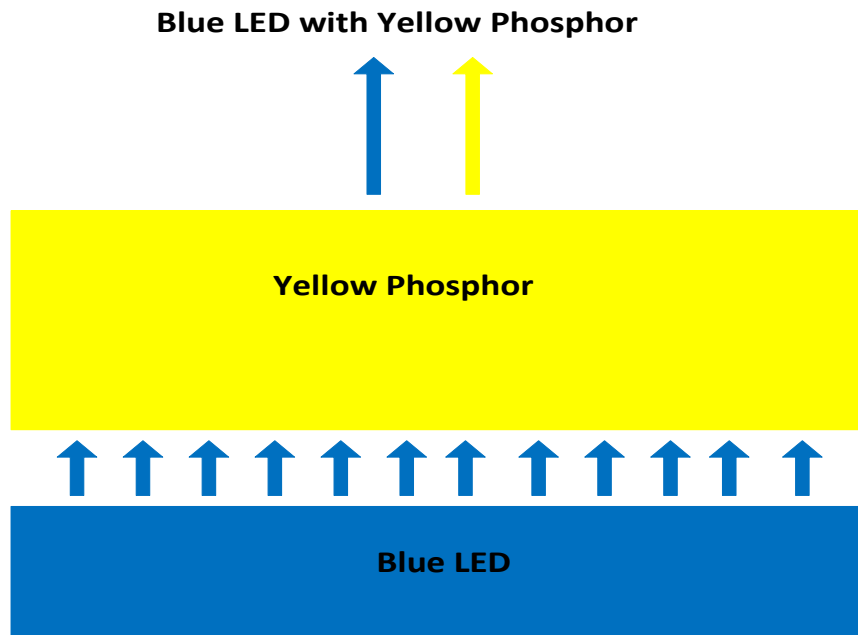


Figure 2.3 Schematic of GaN Chip coated with yellow phosphor.

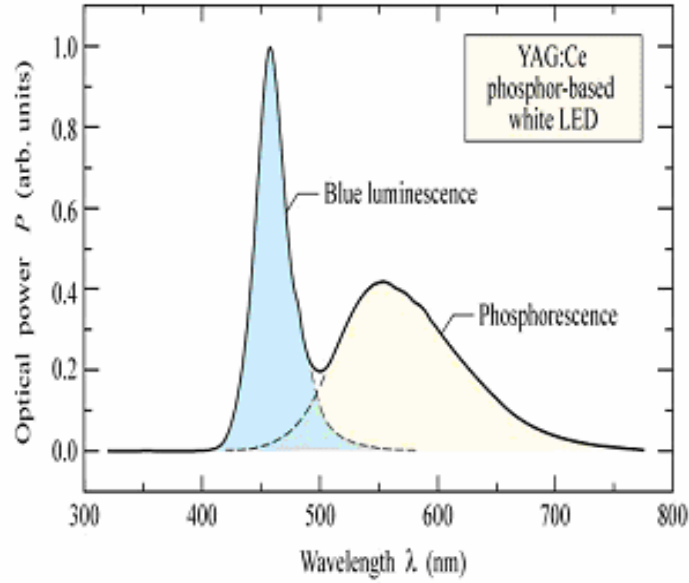


Figure 2.4 Spectral power of phosphor converted white LED.

2.3 Maxwell’s Equations for light propagation

The electromagnetic model to describe the dynamics of white LEDs is based on Maxwell’s equations. Maxwell’s equations in a linear, non-dispersive, and isotopic and source free media are given by

$$\frac{\partial H}{\partial t} = -\frac{1}{\mu} \nabla \times E \tag{2.1}$$

$$\frac{\partial E}{\partial t} = \frac{1}{\epsilon} \nabla \times H \tag{2.2}$$

$$\nabla \cdot D = \rho_{ext} \tag{2.3}$$

$$\nabla \cdot B = 0 \tag{2.4}$$

The six coupled scalar equations derived from basic Maxwell's equations using Faraday's law and Ampere's law in Cartesian coordinate system are given by

$$\frac{\partial H_x}{\partial t} = \frac{1}{\mu} \left(\frac{\partial E_z}{\partial y} - \frac{\partial E_y}{\partial z} \right) \quad 2.5$$

$$\frac{\partial H_y}{\partial t} = \frac{1}{\mu} \left(\frac{\partial E_z}{\partial x} - \frac{\partial E_x}{\partial z} \right) \quad 2.6$$

$$\frac{\partial H_z}{\partial t} = \frac{1}{\mu} \left(\frac{\partial E_x}{\partial y} - \frac{\partial E_y}{\partial x} \right) \quad 2.7$$

$$\frac{\partial E_x}{\partial t} = \frac{1}{\varepsilon} \left(\frac{\partial H_z}{\partial y} - \frac{\partial H_y}{\partial z} \right) \quad 2.8$$

$$\frac{\partial E_y}{\partial t} = \frac{1}{\varepsilon} \left(\frac{\partial H_x}{\partial z} - \frac{\partial H_z}{\partial x} \right) \quad 2.9$$

$$\frac{\partial E_z}{\partial t} = \frac{1}{\varepsilon} \left(\frac{\partial H_y}{\partial x} - \frac{\partial H_x}{\partial y} \right) \quad 2.10$$

Considering 2-dimensional transverse electric (TE) or transverse magnetic (TM) mode, and assuming no variation of the fields in the z-direction, all partial derivatives with respect to z are zero

$$\frac{\partial H_y}{\partial z} = 0, \frac{\partial H_x}{\partial z} = 0, \frac{\partial E_y}{\partial z} = 0, \frac{\partial E_x}{\partial z} = 0 \quad 2.11$$

For TM polarized wave, the equations are expressed as

$$\frac{\partial E_x}{\partial t} = \frac{1}{\varepsilon} \frac{\partial H_z}{\partial y} \quad 2.12$$

$$\frac{\partial E_y}{\partial t} = -\frac{1}{\varepsilon} \frac{\partial H_z}{\partial x} \quad 2.13$$

$$\frac{\partial H_z}{\partial t} = \frac{1}{\mu} \left(\frac{\partial E_x}{\partial y} - \frac{\partial E_y}{\partial x} \right) \quad 2.14$$

For TE polarized wave, the equations are expressed as

$$\frac{\partial H_x}{\partial t} = -\frac{1}{\mu} \frac{\partial E_z}{\partial y} \quad 2.15$$

$$\frac{\partial H_y}{\partial t} = \frac{1}{\mu} \frac{\partial E_z}{\partial x} \quad 2.16$$

$$\frac{\partial E_z}{\partial t} = \frac{1}{\varepsilon} \left(\frac{\partial H_y}{\partial x} - \frac{\partial H_x}{\partial y} \right) \quad 2.17$$

2.4 Material Dispersion Models

The behavior of materials can be described by constitutive parameters which are frequency dependent in reality. Therefore, it is important to know about the frequency response to incorporate the material properties in FDTD. There are certain standard models found in literature that define the frequency response of material. These models are based on the fundamental physical concept of dipole formation by the applied electrical field. Understanding this behavior leads to model the electric susceptibility and permittivity of the medium. The behavior of a dispersive medium can be defined by the following constitutive relations in frequency domain as:

$$D(\omega) = \varepsilon(\omega)E(\omega) \quad 2.18$$

$$P(\omega) = \varepsilon_0 \chi(\omega) E(\omega) \quad 2.19$$

where $P(\omega)$ is the frequency dependent polarization induced in the material due to an applied electric field $E(\omega)$ and χ is the susceptibility of the medium, which represents the ability of the dielectric to polarize in an applied dielectric field.

By combining eq. 2.18 and eq. 2.19, we get

$$D(\omega) = \varepsilon_0 E(\omega) (1 + \chi(\omega)) \quad 2.20$$

The permittivity can be written as

$$\varepsilon(\omega) = \varepsilon_0 (1 + \chi(\omega)) \quad 2.21$$

with relative permittivity as

$$\varepsilon_r(\omega) = 1 + \chi(\omega) \quad 2.22$$

With the above expressions it is now possible to assign a material model depending on the properties of the material.

2.4.1 The Lorentz Model

The Lorentz oscillator model is one of the well know material models that employs the simplest picture of atom-field interaction. It is derived by considering driven harmonic oscillator which assumes atom as a mass (nucleus) attached to smaller mass (electron) through a spring. The incident electric field of electromagnetic wave will set the electron into harmonic motion. The Lorentz model defines the temporal response of a system in terms of polarization of the medium and electric field as:

$$\frac{d^2P}{dt^2} + \Gamma \frac{dP}{dt} + \omega_0^2 P = \varepsilon_0 \omega_p^2 E \quad 2.23$$

where $\omega_0 = \sqrt{\frac{k}{m}}$ and $\omega_p = \sqrt{\frac{Ne^2}{\varepsilon_0 m}}$

k is spring constant in Newton/ meter

N is charges / molecules per unit volume

The response of the system in frequency domain, assuming $e^{-j\omega t}$ time dependence, is given by :

$$P(\omega) = \frac{\varepsilon_0 \omega_p^2}{\omega_0^2 + j\Gamma\omega - \omega^2} E(\omega) \quad 2.24$$

The electric susceptibility can be defined as:

$$\chi_{lorentz}(\omega) = \frac{P(\omega)}{\varepsilon_0 E(\omega)} = \frac{\omega_p^2}{\omega_0^2 + j\Gamma\omega - \omega^2} \quad 2.25$$

The permittivity can be obtained as :

$$\varepsilon_{lorentz}(\omega) = \varepsilon_o(1 + \chi_{lorentz}(\omega)) \quad 2.24$$

The electric flux density can be calculated using

$$D(\omega) = \varepsilon_o \left(1 + \frac{\omega_p^2}{\omega_o^2 + j\Gamma\omega - \omega^2} \right) E(\omega) \quad 2.26$$

2.4.2 The Drude Model

The Drude Model is a simplified form of the Lorentz model that can be derived by neglecting the restoring force in a harmonic oscillator. This model was first proposed by Paul Drude to explain the electron transport properties in the metals. The Drude model defines the temporal response of system under the applied electric field as:

$$\frac{d^2P}{dt^2} + \Gamma \frac{dP}{dt} = \varepsilon_o \omega_p^2 E \quad 2.27$$

The electric susceptibility can be defined as:

$$\chi_{Drude}(\omega) = \frac{P(\omega)}{\varepsilon_o E(\omega)} = \frac{\omega_p^2}{j\Gamma\omega - \omega^2} \quad 2.28$$

The permittivity can be obtained as:

$$\varepsilon_{Drude}(\omega) = \varepsilon_o(1 + \chi_{Drude}(\omega)) \quad 2.29$$

The electric flux density can be calculated using

$$D(\omega) = \varepsilon_o \left(1 + \frac{\omega_p^2}{j\Gamma\omega - \omega^2} \right) E(\omega) \quad 2.30$$

2.4.3 The Lorentz-Drude Model

This model is the most generalized form that describes the interaction of electromagnetic wave with metals. This model is derived by representing the permittivity of material due to free electrons and bounded electrons in metal. The permittivity of Lorentz model is defined by oscillation of bounded electrons in metals and the permittivity of Drude model is defined by oscillations of free electrons in metals. As a result, the permittivity can be defined as:

$$\varepsilon = \varepsilon_{free} + \varepsilon_{bound} \quad 2.31$$

The permittivity of Lorentz Mode is given as

$$\varepsilon_{bound} = \frac{\omega_p^2}{\omega_o^2 + j\Gamma\omega - \omega^2} \quad 2.31$$

The permittivity of Drude Mode is given as

$$\varepsilon_{free} = 1 + \frac{\omega_p^2}{j\Gamma\omega - \omega^2} \quad 2.32$$

The electric flux density can be defined as

$$D(\omega) = \epsilon_o \left(1 + \frac{\omega_p^2}{j\Gamma\omega - \omega^2} + \frac{\omega_p^2}{\omega_o^2 + j\Gamma\omega - \omega^2} \right) \quad 2.33$$

In this thesis, Silver is used for plasmonic structures whose permittivity is modeled using the six-pole Lorentz-Drude model [34]. The relative permittivity of silver using this Lorentz-Drude model is shown in Figure 2.5.

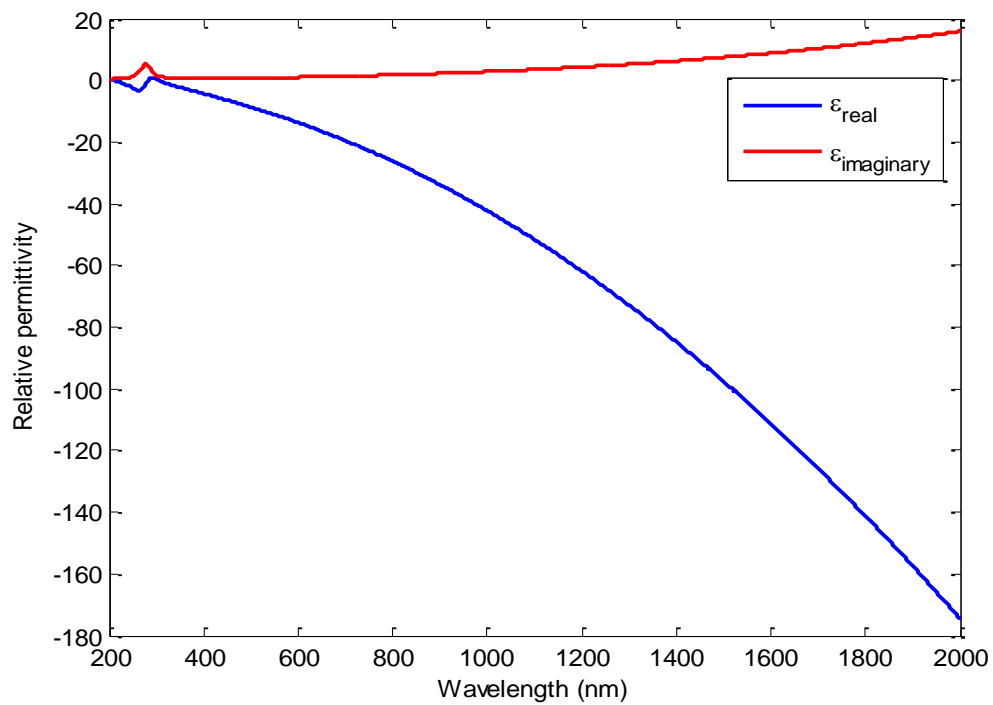


Figure 2.5 Six pole Lorentz Drude Model of Silver metal.

CHAPTER 3

FINITE DIFFERENCE TIME DOMAIN (FDTD)

SIMULATION METHOD

In this chapter, the basics of Finite Difference Time Domain method will be introduced for the solution of Maxwell's equation using Yee's Algorithm. The inclusion of dispersive properties of materials in FDTD will also be explained along with the stability conditions of FDTD. The incorporation of Total field scattered field (TF/SF) technique in FDTD will also be discussed in this chapter.

3.1 Overview of FDTD

The Finite Difference Time Domain (FDTD) method is arguably the most versatile computational electrodynamics modeling method, both conceptually and in terms of implementation. The solutions obtained by this technique cover a wide range of frequency due to the time dependence in the analysis. It has become a popular method to solve numerous problems with extensive applications in new areas in recent years. In 1966, the basic algorithm of FDTD was presented by Kane Yee for the first time. Later on, numerical stability of this algorithm was improved by A. Taflove and M. E. Brodwin with the introduction of the correct stability criteria in 1975. In 1981, G. Mur introduced the first numerically stable absorbing boundary condition (ABC). Later on, J. P. Berenger

published the perfectly matched layer (PML) in 1994. The PML is the most commonly boundary conditions used due to its frequency independent and easy implementation features.

3.1.1 Yee's Algorithm

Yee's Algorithm has been developed by K Yee in 1966 which employs the second order central difference approximation for discretization of Maxwell's curl equations [35]. It provides a robust solution by solving the coupled electric and magnetic field equations simultaneously rather than solving the electric or magnetic fields separately in the wave equation. Yee's mesh is defined by an orthogonal cubic spatial grid whose unit cell is shown in Figure 3.1. It is based on a 3-dimensional Cartesian grid in which E and H components are placed in such a way that every H component is enclosed by four circulating E components and vice versa. Each field components is sampled and evaluated at a particular grid point. The material properties are specified at each grid point such that the continuity of tangential field is maintained at the interfaces of different materials. The E and H components are updated using leapfrog time-stepping algorithm as shown in Figure 3.2. The time advancing algorithm is explicit which calculates the field at each time instant from previously computed field components. The magnetic and electric fields are calculated at time instants staggered by half the sampling time step.

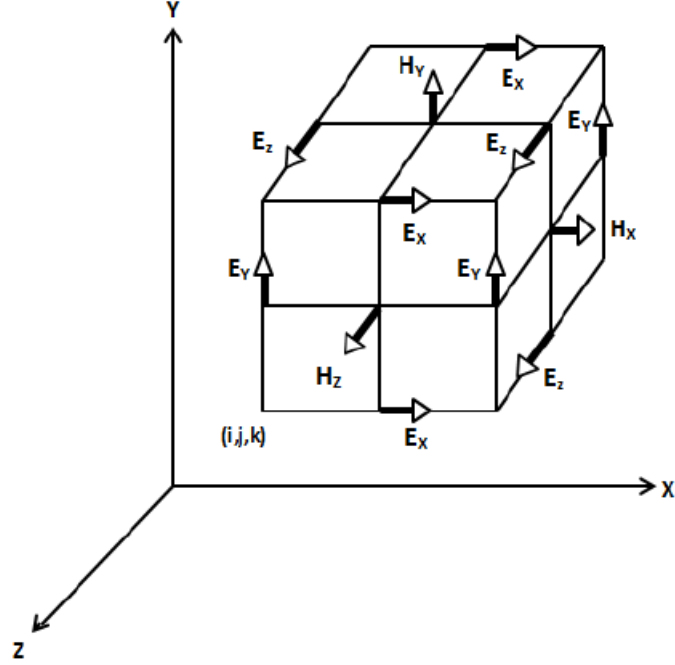


Figure 3.1 Yee's Mesh unit cell.

3.1.2 Finite Difference expressions for Maxwell's equations

To formulate the FDTD solution, the equations for TM polarized wave are approximated by using central difference approximation and then, discretize simultaneously both in space and time utilizing Yee's Algorithm. The resulting equations are

$$\frac{\partial E_x}{\partial t} = \frac{1}{\epsilon} \frac{(H_z(i, j) - H_z(i, j - 1))}{\Delta y} \quad 3.1$$

$$\frac{\partial E_y}{\partial t} = -\frac{1}{\epsilon} \frac{(H_z(i, j) - H_z(i - 1, j))}{\Delta x} \quad 3.2$$

$$\frac{\partial H_z}{\partial t} = \frac{1}{\mu} \left(\frac{(E_x(i, j + 1) - E_x(i, j))}{\Delta y} - \frac{(E_y(i + 1, j) - E_y(i, j))}{\Delta x} \right) \quad 3.3$$

The electric and magnetic field is again computed using Yee's algorithm and leapfrog time-stepping scheme as shown in Figure 3.2. In this scheme, the E and H fields are off-set in time by half time step.

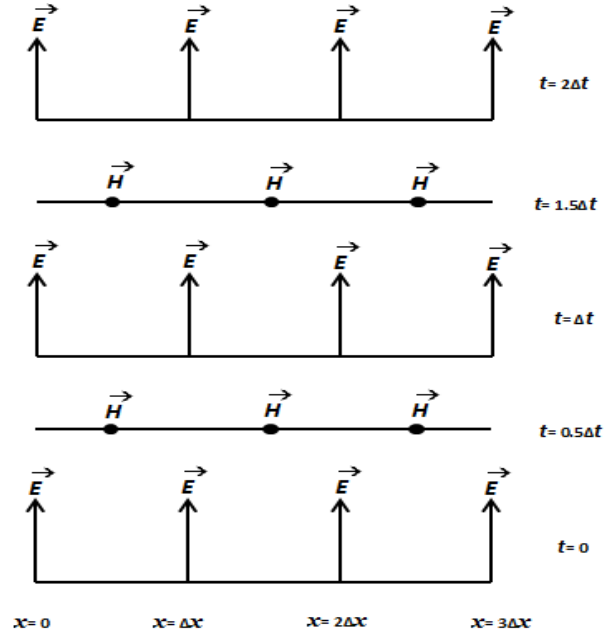


Figure 3.2 Leap-frog algorithm in time.

The update equations for calculating the electric and magnetic field components for a TM polarized wave are given as

$$\begin{aligned}
 E_x^{n+1}\left(i + \frac{1}{2}, j\right) &= E_x^n\left(i + \frac{1}{2}, j\right) \\
 &+ \frac{\Delta t}{\Delta y \cdot \epsilon} \left(H_z^{n+1/2}\left(i + \frac{1}{2}, j + \frac{1}{2}\right) - H_z^{n+1/2}\left(i + \frac{1}{2}, j - \frac{1}{2}\right) \right)
 \end{aligned}
 \tag{3.4}$$

$$\begin{aligned}
E_x^{n+1}\left(i + \frac{1}{2}, j\right) &= E_x^n\left(i + \frac{1}{2}, j\right) \\
&+ \frac{\Delta t}{\Delta y \cdot \varepsilon} \left(H_z^{n+1/2}\left(i + \frac{1}{2}, j + \frac{1}{2}\right) - H_z^{n+1/2}\left(i + \frac{1}{2}, j - \frac{1}{2}\right) \right)
\end{aligned} \tag{3.5}$$

$$\begin{aligned}
H_z^{n+1}\left(i + \frac{1}{2}, j + \frac{1}{2}\right) &= H_z^n\left(i + \frac{1}{2}, j + \frac{1}{2}\right) + \frac{\Delta t}{\Delta y \cdot \mu} \left(E_z^{n+1}\left(i + \frac{1}{2}, j + 1\right) - \right. \\
&\left. E_z^{n+1}\left(i + \frac{1}{2}, j\right) \right) - \frac{\Delta t}{\Delta x \cdot \mu} \left(E_y^{n+1}\left(i + 1, j + \frac{1}{2}\right) - E_y^{n+1}\left(i, j + \frac{1}{2}\right) \right)
\end{aligned} \tag{3.6}$$

where Δx , Δy , Δt are discretized steps in space and time.

3.1.3 Grid size, step time and Stability Criterion for FDTD

Space grid size and time step are most important grid parameters in defining the FDTD model for a given problem. These parameters must be chosen according to certain rules to avoid any instability in the algorithm. The restrictions on the space grid size are due to numerical dispersion in the FDTD algorithm which causes some non-physical effects such as broadening of pulses, anisotropy and pseudo reflections. The rule of thumb is that space grid size must be a fraction of wavelength so that electromagnetic field does not change significantly over one increment in space grid size. To resolve the principle wavelength of propagation mode (λ_p), the grid density per wavelength should follow

$$\Delta_{max} \leq \frac{\lambda_p}{10} \quad \text{and} \quad \Delta_x, \Delta_y \leq \Delta_{max} \tag{3.7}$$

Once the space grid sizes are chosen, the time step is bounded via computational stability criteria. For constant ε and μ , the computational stability requires that

$$\sqrt{(\Delta x)^2 + (\Delta y)^2} > c\Delta t = \sqrt{\frac{1}{\varepsilon\mu}} \Delta t \quad 3.8$$

where c is the speed of light. If v_{max} is the maximum speed of light in given medium, then the stability criteria is

$$\sqrt{(\Delta x)^2 + (\Delta y)^2} > v_{max}\Delta t \quad 3.9$$

where Δx , Δy , Δt are discretized steps in space and time.

3.2 Auxiliary Differential Equation FDTD (ADE-FDTD)

The modeling of material properties is one of the most important subjects in the analysis of photonic devices. The FDTD has the potential to easily incorporate the dispersive nature of material in it using different methods. The auxiliary differential equation FDTD (ADE-FDTD) was proposed by Taflove [36] to introduce the dispersive relation of metals and dielectrics in the FDTD. In this method, the dispersive relation is converted from frequency domain to time domain using inverse Fourier transform and as a result, electric field is computed from pervious values of E and D. Finally, the relation is added into FDTD method to update the electric field.

In order to introduce multiple dispersion relations for a material in the FDTD, the general algorithm proposed by Alsunaidi and Al-Jabr [37] is used. This algorithm can be applied to dispersion relation of any material. The general form of dispersion relation having N -poles can be defined as

$$D = \varepsilon_o \varepsilon_\infty E + \sum_{i=1}^N P_i \quad 3.10$$

After the discretization, we get

$$D^{n+1} = \varepsilon_o \varepsilon_\infty E^{n+1} + \sum_{i=1}^N P_i^{n+1} \quad 3.11$$

The equation can be re-arranged to compute the E field:

$$E^{n+1} = \frac{D^{n+1} - \sum_{i=1}^N P_i^{n+1}}{\varepsilon_o \varepsilon_\infty} \quad 3.12$$

The Lorentz model in the frequency domain can be written as:

$$P(\omega) = \frac{a}{b + jc\omega - d\omega^2} E(\omega) \quad 3.13$$

After taking the inverse Fourier transform, we get

$$bP(t) + cP'(t) + dP''(t) = aE(t) \quad 3.14$$

The polarization field can be discretized as:

$$bP^n + c \frac{P^{n+1} - P^{n-1}}{2\Delta t} + d \frac{P^{n+1} - 2P^n + P^{n-1}}{\Delta t^2} = aE^n \quad 3.15$$

After re-arranging to compute P^{n+1} , we get;

$$P^{n+1} = \frac{4d - 2b\Delta t^2}{2d + c\Delta t} P^n + \frac{-2d + c\Delta t}{2d + c\Delta t} P^n + \frac{2a\Delta t^2}{2d + c\Delta t} E^n \quad 3.16$$

It can be written in simplified form as

$$P^{n+1} = C_1 P^n + C_2 P^{n-1} + C_3 E^n \quad 3.17$$

The constants C_1 , C_2 and C_3 are calculated using :

$$C_1 = \frac{4d - 2b\Delta t^2}{2d + c\Delta t} \quad C_2 = \frac{-2d + c\Delta t}{2d + c\Delta t} \quad C_3 = \frac{2a\Delta t^2}{2d + c\Delta t}$$

For the multi-pole Lorentz model the values of C_1 , C_2 and C_3 are different for different materials. These values of a, b, c and d are obtained by fitting the experimental data of dielectric constant for a certain material into Lorentz model.

3.3 Total Field /Scattered Field (TF/SF) FDTD Formulation

The total field / scattered field formulation is a versatile method to generate uniform plane wave by incorporating incident source conditions in the FDTD algorithm. The linearity principle on Maxwell's equations is applied to compute the field components. The 2-dimensional computational domain is shown in Figure 3.3. The simulation domain is subdivided into total field (TF) and scattered field (SF) regions which are isolated by nonphysical virtual boundary called TF/SF boundary. The scattering objects having arbitrary shapes are placed in the total field region. Perfectly Matched layer (PML) is defined on four sides of the computational space by applying the absorbing boundary conditions. It is a hypothetical medium that absorbs the incident electromagnetic waves with minimal reflection.

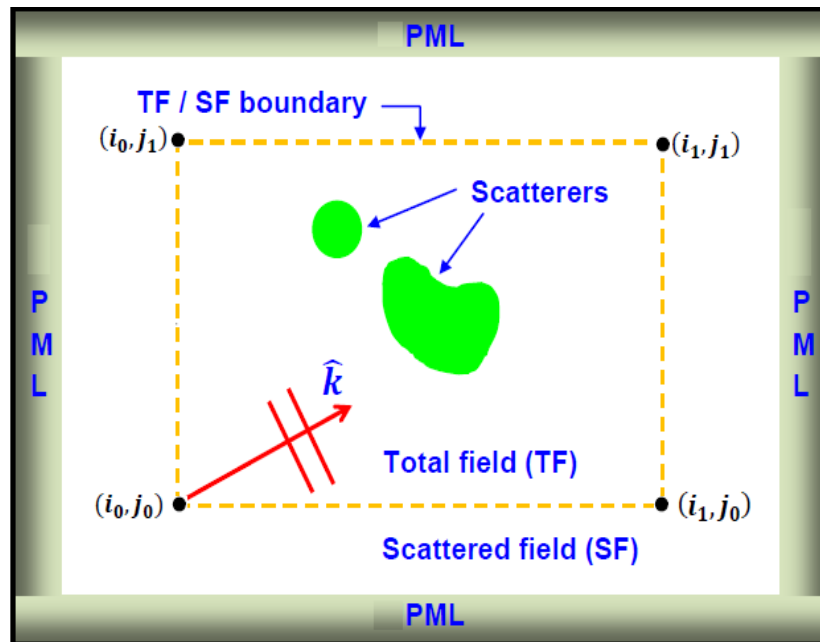


Figure 3.3 Computation window for TF/SF.

In TF/SF formulation, the total field is represented by the field components computed in the TF region and the scattered field is represented by the field components computed in the SF region. The field components are divided into incident and scattered field which are used to calculate the total electric and magnetic field given as

$$E_{total} = E_{inc} + E_{scat} \quad H_{total} = H_{inc} + H_{scat} \quad 3.18$$

Yee's Algorithm is applied to compute the field components in both regions via FDTD update equations. The only difference is that they will be operating on two different set of fields. As a result, the inconsistency would arise by applying FDTD update equations at the TF/SF boundary. At the TF/SF boundary, the field in TF region is total field composed of incident and scattered field components and on the other side of boundary is scattered field. The inconsistency exists due to taking the difference between these fields components to update the field quantity on the boundary. This inconsistency can be removed by using the value of incident field at TF/SF boundary points at the current time.

In TF region, the FDTD solution for E_x would be

$$E_{x,total}^{n+1} \left(i + \frac{1}{2}, j \right) = \quad 3.19$$

$$E_{x,total}^n \left(i + \frac{1}{2}, j \right) - \frac{\Delta t}{\epsilon \Delta y} \left(H_{z,total}^{n+\frac{1}{2}} \left(i + \frac{1}{2}, j + \frac{1}{2} \right) - H_{z,total}^{n+\frac{1}{2}} \left(i + \frac{1}{2}, j - \frac{1}{2} \right) \right)$$

and correspondingly in SF region, it would be

$$E_{x,scat}^{n+1} \left(i + \frac{1}{2}, j \right) = \tag{3.20}$$

$$E_{x,scat}^n \left(i + \frac{1}{2}, j \right) - \frac{\Delta t}{\epsilon \Delta y} \left(H_{z,scat}^{n+\frac{1}{2}} \left(i + \frac{1}{2}, j + \frac{1}{2} \right) - H_{z,scat}^{n+\frac{1}{2}} \left(i + \frac{1}{2}, j - \frac{1}{2} \right) \right)$$

Consider the bottom interface, the solution for E_x at TF/SF boundary can be found as:

$$E_{x,total}^{n+1} \left(i + \frac{1}{2}, j_0 \right) =$$

$$E_{x,total}^n \left(i + \frac{1}{2}, j_0 \right) - \frac{\Delta t}{\epsilon \Delta y} \left(H_{z,total}^{n+\frac{1}{2}} \left(i + \frac{1}{2}, j_0 + \frac{1}{2} \right) - H_{z,scat}^{n+\frac{1}{2}} \left(i + \frac{1}{2}, j_0 - \frac{1}{2} \right) \right) \tag{3.21}$$

The inconsistency seen in the eq. 3.21 can be removed by substituting eq. 3.18 for H fields giving the equation

$$E_{x,total}^{n+1} \left(i + \frac{1}{2}, j_0 \right) =$$

$$E_{x,total}^n \left(i + \frac{1}{2}, j_0 \right) -$$

$$\frac{\Delta t}{\epsilon \Delta y} \left(H_{z,total}^{n+\frac{1}{2}} \left(i + \frac{1}{2}, j_0 + \frac{1}{2} \right) - H_{z,total}^{n+\frac{1}{2}} \left(i + \frac{1}{2}, j_0 - \frac{1}{2} \right) \right) + \frac{\Delta t}{\epsilon \Delta y} H_{z,inc}^{n+1/2} \left(i + \frac{1}{2}, j_0 - \frac{1}{2} \right) \tag{3.22}$$

It can be simplified as:

$$E_{x,total}^{n+1} \left(i + \frac{1}{2}, j_0 \right) = E_{x,total}^n \left(i + \frac{1}{2}, j_0 \right) + \frac{\Delta t}{\epsilon \Delta y} H_{z,inc}^{n+1/2} \left(i + \frac{1}{2}, j_0 - \frac{1}{2} \right) \tag{3.23}$$

At TF/SF boundary, the solution for E_x by considering the top interface $j = j_1$

$$E_{x,total}^{n+1} \left(i + \frac{1}{2}, j_1 \right) = E_{x,total}^{n+1} \left(i + \frac{1}{2}, j_1 \right) - \frac{\Delta t}{\epsilon \Delta y} H_{z,inc}^{n+1/2} \left(i + \frac{1}{2}, j_1 + \frac{1}{2} \right) \quad 3.24$$

At TF/SF boundary, the solution for E_y by considering the left interface $i = i_0$

$$E_{y,total}^{n+1} \left(i_0 + 1, j + \frac{1}{2} \right) = E_{x,total}^{n+1} \left(i_0 + 1, j + \frac{1}{2} \right) + \frac{\Delta t}{\epsilon \Delta y} H_{z,inc}^{n+1/2} \left(i_0 + \frac{1}{2}, j - \frac{1}{2} \right) \quad 3.25$$

At TF/SF boundary, the solution for E_y by considering the top interface $i = i_1$

$$E_{y,total}^{n+1} \left(i_1 + 1, j + \frac{1}{2} \right) = E_{x,total}^{n+1} \left(i_1 + 1, j + \frac{1}{2} \right) - \frac{\Delta t}{\epsilon \Delta y} H_{z,inc}^{n+1/2} \left(i_1 + \frac{3}{2}, j - \frac{1}{2} \right) \quad 3.26$$

A similar procedure is followed for the correction of H_z fields.

One-dimensional auxiliary computational domain is considered to calculate the expressions for $H_{z,inc}$, $E_{x,inc}$ and $E_{y,inc}$ using FDTD as:

$$E_{1D,inc}^{n+1}(m) = E_{1D,inc}^n(m) + \frac{\Delta t}{\epsilon \Delta x} \left(H_{1D,inc}^{n+\frac{1}{2}}(m - 1/2) - H_{1D,inc}^{n+\frac{1}{2}}(m + 1/2) \right) \quad 3.27$$

$$H_{1D,inc}^{n+1/2} \left(m + \frac{1}{2} \right) = H_{1D,inc}^{n-\frac{1}{2}} \left(m + \frac{1}{2} \right) + \frac{\Delta t}{\mu_o \Delta x} (E_{1D,inc}^n(m) - E_{1D,inc}^n(m + 1)) \quad 3.28$$

$$H_{z,inc}^{n+1/2}(d) = H_{1D,inc}^{n+1/2}(d) \quad 3.29$$

$$E_{x,inc}^{n+1}(d) = E_{1D,inc}^{n+1} \cos\phi$$

$$E_{y,inc}^{n+1}(d) = -E_{1D,inc}^{n+1} \sin\phi$$

where d is the representative location of the field and ϕ is the angle at which the incident plane wave is oriented. Figure 3.4 illustrates the step by step procedure for incorporating TF/SF boundary condition in the General ADE FDTD algorithm.

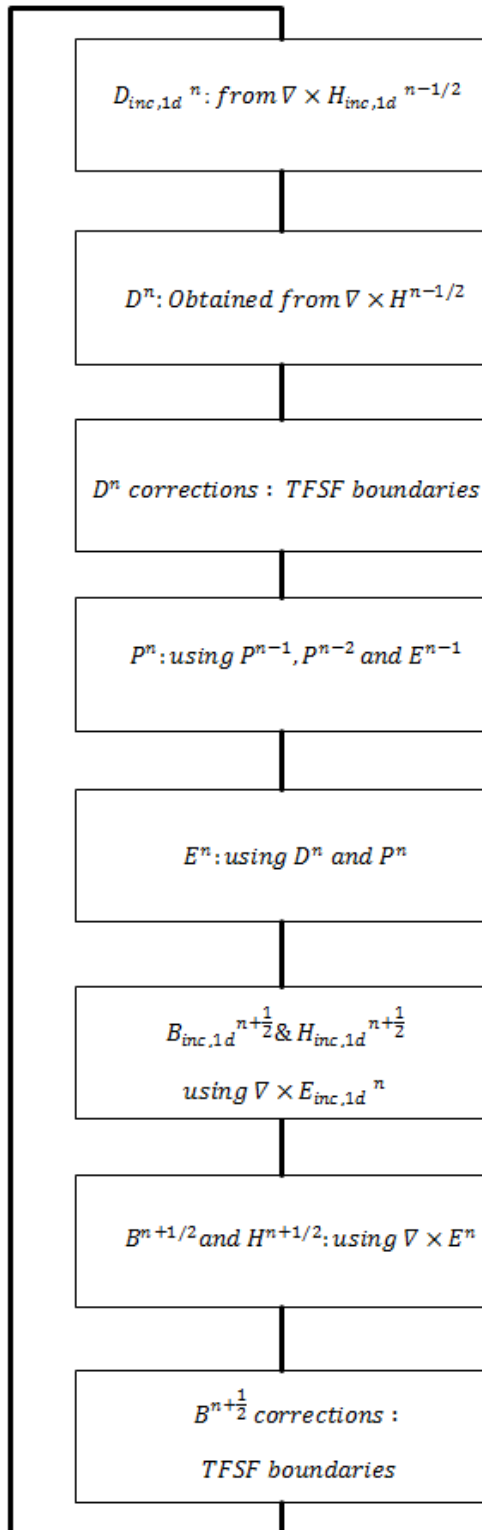


Figure 3.4 Flow chart of incorporating TF/SF boundary in general ADE-FDTD algorithm.

CHAPTER 4

MODELING OF YELLOW PHOSPHOR CONVERTED

WHITE LEDS

This chapter investigates the modeling of white light conversion process using commercially available yellow phosphor material (YAG:Ce³⁺) for GaN LEDs. The electrodynamics of yellow phosphor is translated into quantum coupled electromagnetic model by incorporating the absorption and emission properties. The spontaneous emission and luminance saturation modeling is also explained in this Chapter.

4.1 Modeling of YAG:Ce³⁺

Phosphors have been realized as a key and technologically important component of white LEDs. The efficiency of a white LED mainly depends on optical light conversion phenomena associated with phosphor materials. The most popular commercial phosphor is Cerium doped yttrium aluminum garnet (YAG:Ce³⁺) used in GaN LEDs to produce white light. The modeling of the electrodynamics of YAG:Ce³⁺ phosphor is necessary to gauge the optical performance of white LEDs. There are different steps involved in modeling the yellow phosphor converted white LEDs which are described in this section.

4.1.1 Medium modeling using Lorentzian Function

Lorentzian functions are extensively used for modeling the non-linear, non-isotropic and dispersive media by selecting the appropriate parameters. Special Schemes of FDTD are needed to model the media with complex $\varepsilon(\omega)$ as discussed in previous chapter. ADE-FDTD methodology with a Lorentzian function will be used to represent the polarization of the medium in this thesis work. The complex permittivity of the medium can be represented as

$$\varepsilon(\omega) = \varepsilon'(\omega) + j\varepsilon''(\omega) \quad 4.1$$

where $\varepsilon'(\omega)$ is the real part of permittivity which represent energy stored in the medium and $\varepsilon''(\omega)$ is the imaginary part of permittivity which represent loss or gain in the medium depending on the sign. The Lorentzian function in terms of medium polarization can be written as:

$$P(\omega) = \frac{a}{b + jc\omega - d\omega^2} E(\omega) \quad 4.2$$

where $P(\omega)$ is frequency dependent medium polarization, $E(\omega)$ is frequency dependent electric field, and a , b , c and d are Lorentzian parameters describing the medium polarization. The Lorentzian function in complex permittivity can be represented as:

$$\varepsilon(\omega) = \varepsilon_0\varepsilon_\infty + \frac{a}{b + jc\omega - d\omega^2} \quad 4.3$$

In this thesis work, yellow phosphor is modeled using Lorentzian function. The complex form of refractive index of YAG:Ce³⁺ phosphor crystal is defined as;

$$n_{pc} = n'_{pc} - jn''_{pc} \quad 4.4$$

where n'_{pc} and n''_{pc} are real and imaginary parts of refractive index of phosphor crystal.

The n'_{pc} of phosphor crystal does not vary significantly with wavelength in visible region and is considered constant i.e 1.843. The imaginary part n''_{pc} can be calculated using

$$n''_{pc} = \frac{\alpha(\omega)\lambda}{4\pi} \quad 4.5$$

where α is the absorption coefficient of phosphor crystal and calculated experimentally as shown in Figure 4.1. The absorption coefficient depends on the wavelength of light for YAG: Ce³⁺ [38].

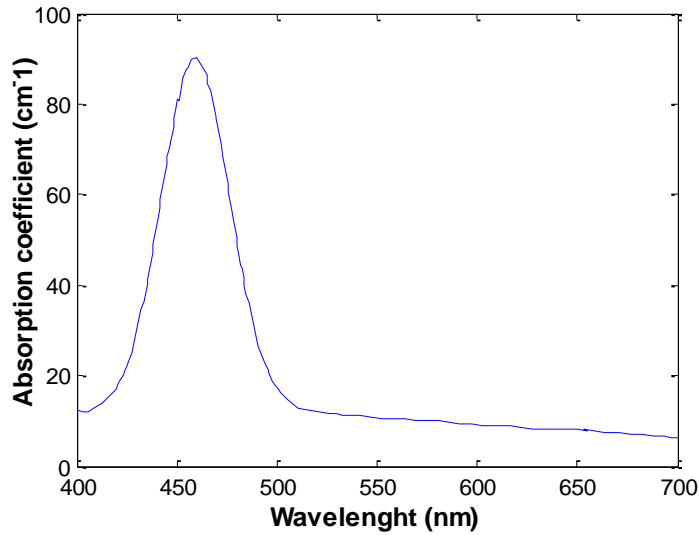


Figure 4.1 Absorption coefficient of YAG: Ce³⁺.

In order to model the YAG:Ce³⁺ medium, the refractive indices are translated into complex permittivity form using the relations:

$$\varepsilon' = (n'_{pc})^2 - (n''_{pc})^2 \quad 4.6$$

$$\varepsilon'' = 2n'_{pc}n''_{pc} \quad 4.7$$

The Lorentzian parameters (a, b, c, d) are used to add the material properties of YAG:Ce³⁺ using general algorithm in ADE-FDTD model.

4.1.2 Four Level Rate Equation Model

The ADE-FDTD method is used to study the mutual interaction of electromagnetic field and phosphor material. In this method, material specific rate equations are used to model the quantum mechanics based light emission. The schematic of energy level, electronic transition process of YAG:Ce³⁺ is illustrated in the Figure 4.2. The 4-Level electromagnetic quantum coupled model with energy levels E₀, E₁, E₂ and E₃, is proposed which describes the electron population dynamics at each level described by the rate equations. The optical pumping mechanism is included in the model by adding the medium polarization which transfers the energy from ground to upper energy level via stimulated absorption.

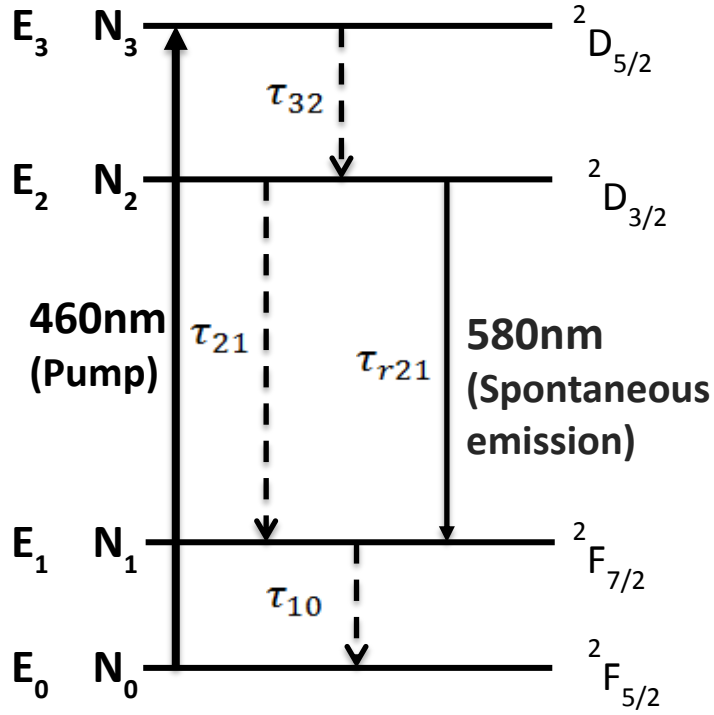


Figure 4.2 Ce³⁺ electron transition accounted in the rate equation model.

$$\begin{aligned}
 \frac{dN_3(t)}{dt} &= -\frac{N_3(t)}{\tau_{32}} + \frac{1}{\hbar\omega_p} E(t) \cdot \frac{dP_p(t)}{dt} \\
 \frac{dN_2(t)}{dt} &= \frac{N_3(t)}{\tau_{32}} - \frac{N_2(t)}{\tau_{21}} - \frac{N_2(t)}{\tau_{r21}} \\
 \frac{dN_1(t)}{dt} &= \frac{N_2(t)}{\tau_{21}} + \frac{N_2(t)}{\tau_{r21}} - \frac{N_1(t)}{\tau_{10}} \\
 \frac{dN_0(t)}{dt} &= \frac{N_1(t)}{\tau_{10}} - \frac{1}{\hbar\omega_p} E(t) \cdot \frac{dP_p(t)}{dt}
 \end{aligned} \tag{4.8}$$

where N_0, N_1, N_2 and N_3 are the population values in the ground level, level 1, level 2 and level 3 respectively and τ_{ij} are the relaxation times from levels i to j . The energy

levels of Ce^{3+} are ${}^2F_{5/2}$, ${}^2F_{3/2}$, ${}^2D_{3/2}$ and ${}^2D_{5/2}$ that correspond to E_0 , E_1 , E_2 and E_3 respectively. The introduction of the term $1/(\hbar\omega_p)E(t).dP(t)/dt$ in rate equations represents energy transfer from N_0 to N_3 with ω_p corresponds to pumping wavelength of 460 nm.

4.1.3 Discretization and ADE-FDTD Solution

The equations are discretized using ADE-FDTD method in the following way;

$$\begin{aligned}
N_3^{n+1} &= \frac{2\tau_{32} - \Delta t}{2\tau_{32} + \Delta t} N_3^n + \frac{2\tau_{32}\Delta t}{2\tau_{32} + \Delta t} \frac{(E^{n+1} + E^n) \cdot (P_p^{n+1} - P_p^n)}{\hbar\omega_p \Delta t} \\
N_2^{n+1} &= \frac{2\tau_{21}\tau_{21r} - \tau_{21r}\Delta t - \tau_{21r}\Delta t}{2\tau_{21}\tau_{21r} + \tau_{21r}\Delta t + \tau_{21r}\Delta t} N_2^n \\
&\quad + \frac{2\tau_{21}\tau_{21r}\Delta t}{2\tau_{21}\tau_{21r} + \tau_{21r}\Delta t + \tau_{21r}\Delta t} (N_3^{n+1} + N_3^n) \\
N_1^{n+1} &= \frac{2\tau_{10} - \Delta t}{2\tau_{10} + \Delta t} N_1^n + \frac{\tau_{10}\Delta t(\tau_{21r} + \tau_{21})}{\tau_{21}\tau_{21r}(2\tau_{10} + \Delta t)} (N_2^{n+1} + N_2^n) \\
N_0^{n+1} &= N_0^n + \frac{\Delta t}{2\tau_{10}} (N_1^{n+1} + N_1^n) - \frac{(E^{n+1} + E^n) \cdot (P_p^{n+1} - P_p^n)}{\hbar\omega_p}
\end{aligned} \tag{4.9}$$

The N_0 (ground level) is assumed to be an infinite reservoir having a very large population density as compared to other energy levels.

The dot product in eq. 4.9 can be expanded to make it consistent in time as follow:

$$E^{n+1} = E^{n+1} \hat{a}_x + E^{n+1} \hat{a}_y \tag{4.10}$$

$$E^n = E^n \hat{a}_x + E^n \hat{a}_y \quad 4.11$$

The \hat{a}_x and \hat{a}_y are unit vectors along the x-axis and y-axis respectively.

$$\begin{aligned} (E^{n+1} + E^n) \cdot (P_p^{n+1} - P_p^n) \\ = (E_{xavg}^{n+1} + E_{xavg}^n) \cdot (P_{p,xavg}^{n+1} - P_{p,xavg}^n) \\ + ((E_{yavg}^{n+1} + E_{yavg}^n)) \cdot (P_{p,xavg}^{n+1} - P_{p,xavg}^n) \end{aligned} \quad 4.12$$

The population densities $N_i (i = 0, 1, 2, 3)$ at different energy levels are defined at spatial location $(i + 1/2, j + 1/2)$ of Yee's grid to make them consistent in space by defining the $E_{xavg}^n, E_{yavg}^n, P_{p,xavg}^n$ and $P_{p,yavg}^n$ as follows

$$\begin{aligned} E_{xavg}^n(i + 1/2, j + 1/2) &= \frac{E_x^n(i + 1/2, j) + E_x^n(i + 1/2, j + 1)}{2} \\ E_{yavg}^n(i + 1/2, j + 1/2) &= \frac{E_y^n(i, j + 1/2) + E_y^n(i + 1, j + 1/2)}{2} \\ P_{p,xavg}^n(i + 1/2, j + 1/2) &= \frac{P_{p,x}^n(i + 1/2, j) + P_{p,x}^n(i + 1/2, j + 1)}{2} \\ P_{p,yavg}^n(i + 1/2, j + 1/2) &= \frac{P_{p,y}^n(i + 1/2, j) + P_{p,y}^n(i + 1, j + 1/2)}{2} \end{aligned} \quad 4.13$$

Similarly, $E_{xavg}^{n+1}, E_{yavg}^{n+1}, P_{p,xavg}^{n+1}$ and $P_{p,yavg}^{n+1}$ can also be defined.

The spatial location of fields and populations densities in Yee's grid is illustrated in Figure 4.3.

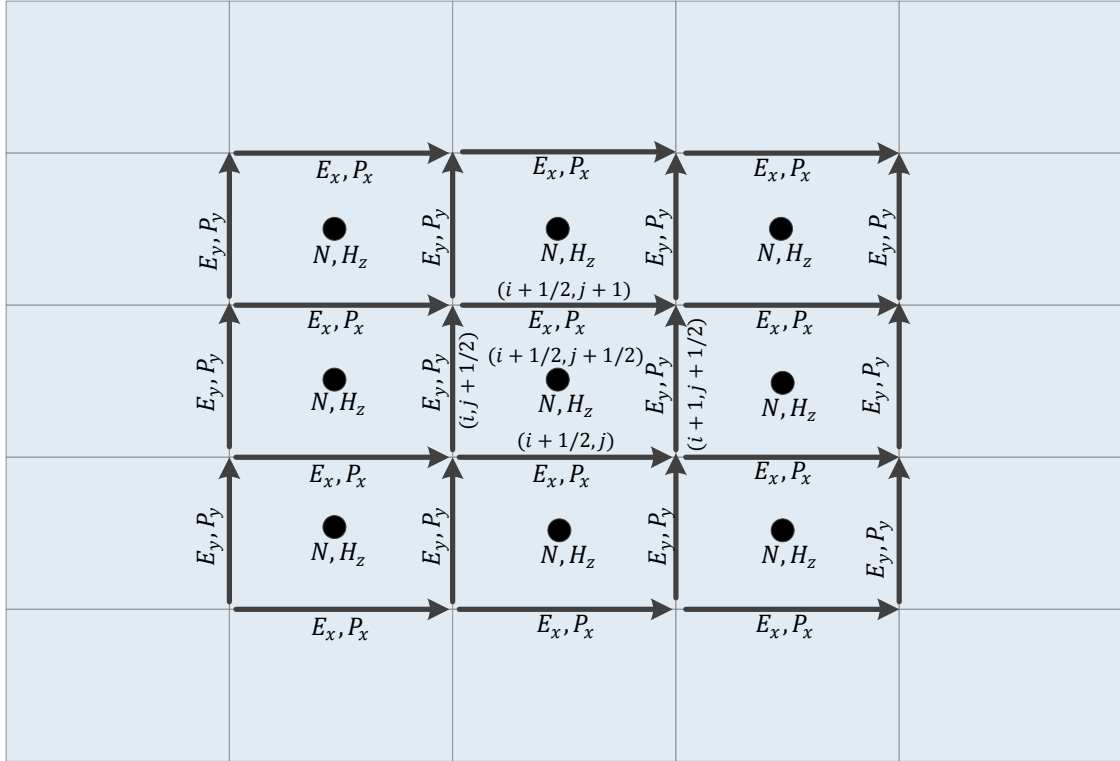


Figure 4.3 Spatial location of field components and population densities.

4.1.4 Spontaneous emission modeling

The phenomenon of spontaneous emission is included in Maxwell equations in terms of external current density function.

$$\nabla \times H = \frac{\partial D}{\partial t} + j(t) \quad 4.14$$

The expression for current density in terms of population is derived and expressed as;

$$j(t) = \eta_c k_p \frac{N_2}{E_{local}} \exp\left[-\frac{(t-t_0)^2}{\sigma^2}\right] \sin(\omega t - \phi) \quad 4.15$$

The spontaneous emission is studied by distributing the dipole sources randomly throughout the phosphor medium. The phase and polarization is assigned randomly as a function of space. The E_{local} represents the electric field strength corresponding to each site in phosphor layer. The η_c represents the conversion efficiency whose value varies between 0 and 1. The k_p represents the proportionality constant determined by equating the absorbed power in material and emitted power by the phosphor material due to N_2 . It is found that proportionality constant can be expressed as;

$$k_p \sim 10^5 \frac{\hbar\omega_a}{\tau_{r21}} \text{ (I/s)} \quad 4.16$$

4.1.5 Emission Line shape

There are numbers of line shape functions that could be used to model the spectral data. The most appropriate function is that which associate the parameters of line shape model with the physical phenomena. The important parameters of line shape function are peak position, peak width, peak area and asymmetry. The physical phenomena that contribute to the final line shape of emission spectrum are Doppler broadening, collision broadening and radiation damping [39].

Gaussian lineshape can be used to describe the Doppler broadening as;

$$G(v) = \frac{A}{\gamma_0} \sqrt{\frac{4 \ln 2}{\pi}} \exp \left[-4 \ln 2 \left(\frac{v - v_0}{\gamma_0} \right)^2 \right] \quad 4.17$$

Lorentzian lineshape can be used to describe the collision broadening and radiation damping phenomena as;

$$L(v) = \frac{2A/\gamma_0\pi}{1 + 4 \left[\left(\frac{v - v_0}{\gamma_0} \right)^2 \right]} \quad 4.18$$

where v is frequency in wavenumber, v_0 is the peak position and γ_0 is the full width half maximum (FWHM) and A is the area under the peak.

The final lineshape of the emission spectrum is defined as a combined effect of Doppler broadening, collision broadening and radiation damping. Thus, the final lineshape is the sum of fractional contributions of Lorentzian and Gaussian lineshape functions as;

$$y(v) = fL(v) + (1 - f)G(v) \quad 4.19$$

where f is the fractional Lorentzian contribution to the final lineshape. The final shape depends on the value of f which can be varied between 0 and 1. The final lineshape is reduced to pure Gaussian and pure Lorentzian corresponding values of $f=0$ and $f=1$ respectively.

The emission spectrum of the YAG:Ce³⁺ is not uniform over the visible band, so it is necessary to include some asymmetric profile in the lineshape model. The best approach is to replace the γ_0 with well-behaved function in which width is varied sigmoidally as;

$$\gamma(\nu) = \frac{2\gamma_0}{1 + \exp [a_{asym}(\nu - \nu_0)]} \quad 4.20$$

The asymmetry in the final line shape is measured by the values of a_{asym} parameter. The positive values of the a_{asym} skew the spectrum towards higher wavelength while negative values of a_{asym} skew the spectrum towards lower wavelength. The lineshape model $\gamma(\nu)$ is reduced to symmetric standard Gaussian and Lorentzian profile when $a_{asym} = 0$.

4.1.6 Luminance Saturation effect Modeling

Phosphor materials exhibit the phenomena of luminance intensity saturation. There are many factors that contribute to this intensity saturation in phosphor. The major factors are concentration of activators in the host, temperature, decay time, non-radiative transitions etc. YAG:Ce³⁺ has a high radiative transition time (ns), so the intensity saturation due to decay time is not significant. The Ce³⁺ concentration plays a significant role in determining the output intensity of yellow phosphor based GaN LEDs. Therefore, it is essential to use optimal concentration of Ce³⁺ to avoid the performance degradation of yellow phosphor based white LEDs. The phenomena of luminance saturation due to activator concentration can be included in the model using different ways. In this thesis, we are incorporating the intensity saturation effect using the density of Ce³⁺ ions in the proposed model. The density of Ce³⁺ ions is defined on the number of occupied emitting

sites in the active phosphor layer. Weibull distribution function is used to add the saturation effect due to density of Ce^{3+} ions. This function is widely used in studying the breaking strength of engineering devices and materials [40]. Many application of this function can be found in electronics, aerospace, material and automotive industry. The Weibull distribution function used for intensity saturation can be defined as;

$$C_{sat}(n) = \frac{k}{b^k} n^{k-1} e^{-\left(\frac{n}{b}\right)^k} \quad 4.21$$

k is shaping parameter

b is scaling parameter

n is density of Ce^{3+} ions in phosphor layer

The scaling factor can be determined using

$$b = \frac{n_s}{\left(\frac{k-1}{k}\right)^{k-1}} \quad 4.22$$

where n_s is the percentage of occupied emitting sites at saturation point.

After introducing the saturation factor in the current density function, the expression for spontaneous emission coupled with Maxwell's equations can be written as;

$$j(t) = \eta_c k_p C_{sat} \frac{N_2}{E_{local}} \sum_{\omega=\omega_1}^{\omega_2} y(\omega) \exp\left[\frac{(t-t_0)^2}{\sigma^2}\right] \sin(\omega t - \phi) \quad 4.23$$

4.2 Simulation Results for yellow phosphor converted LEDs

The proposed model is implemented by considering a simple structure shown in Figure 4.4. The Finite Difference Time Domain (FDTD) method is used to simulate and analyze the dynamics of the structure. The structure consists of three layers in which phosphor layer coated on the blue LED layer. The white light is emitted in to air layer containing both the unabsorbed blue light and broad band yellow light. When the light emitted from blue light source strikes the interface between the phosphor layer and light source, some light is absorbed by the YAG: Ce medium and some is reflected back. After absorption of blue light, the phosphor material convert light into yellow light depending upon the density of Ce^{3+} ions in YAG and rest of light remain blue in phosphor layer. At the end, the white light is produced by intermixing of input blue light and converted yellow light in the phosphor medium.

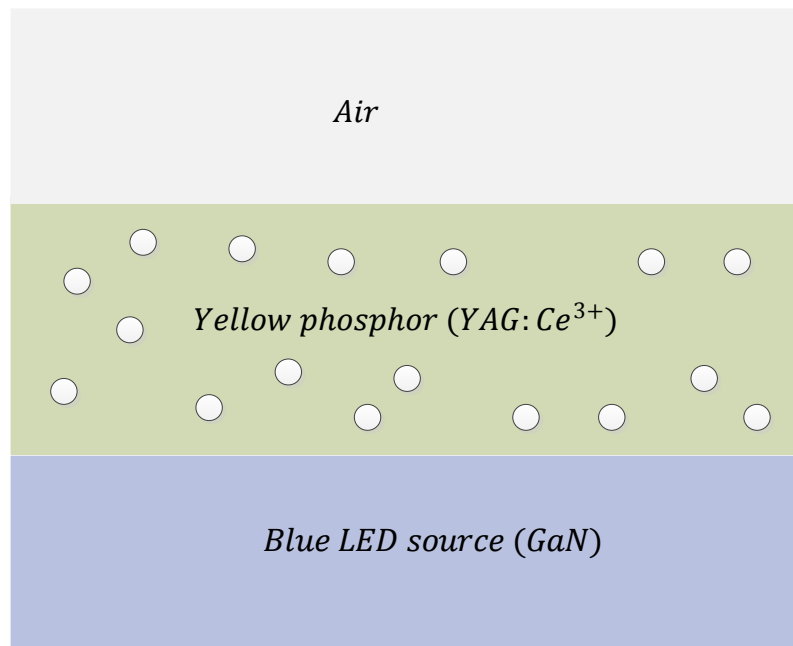


Figure 4.4 Schematic of GaN LED coated with yellow phosphor.

The discretized equation with $\Delta t = 10^{-17}s$ and with the proposed model parameters mentioned in the table are run for 1ns for determining the steady state population densities in different energy levels. The steady state values of population densities are different at each spatial location in the phosphor layer in accordance with incoming blue light from randomly polarized point sources in the GaN layer.

Table 4.1 Parameters for rate equation model

Pump wavelength (nm)	460
Peak Emission Wavelength (nm)	560
$\tau_{32}(s)$	10^{-15}
$\tau_{21r}(s)$	10^{-9}
$\tau_{21}(s)$	10^{-5}

The medium polarization is modeled using the Lorentz-Drude model. The Lorentzian parameters (a, b, c, d) are obtained using curve fitting in MATLAB for ADE-FDTD model. The fitting parameters for imaginary part of permittivity are shown in Table 4.2.

Table 4.2 Lorentz-Drude parameters for YAG:Ce³⁺

Parameter	Value
<i>a</i>	-2.189×10^{27}
<i>b</i>	1.691×10^{31}
<i>c</i>	4.31×10^{14}
<i>d</i>	1.00
ϵ_{∞}	3.40

The fitting result for imaginary part of permittivity is shown in Figure 4.5.

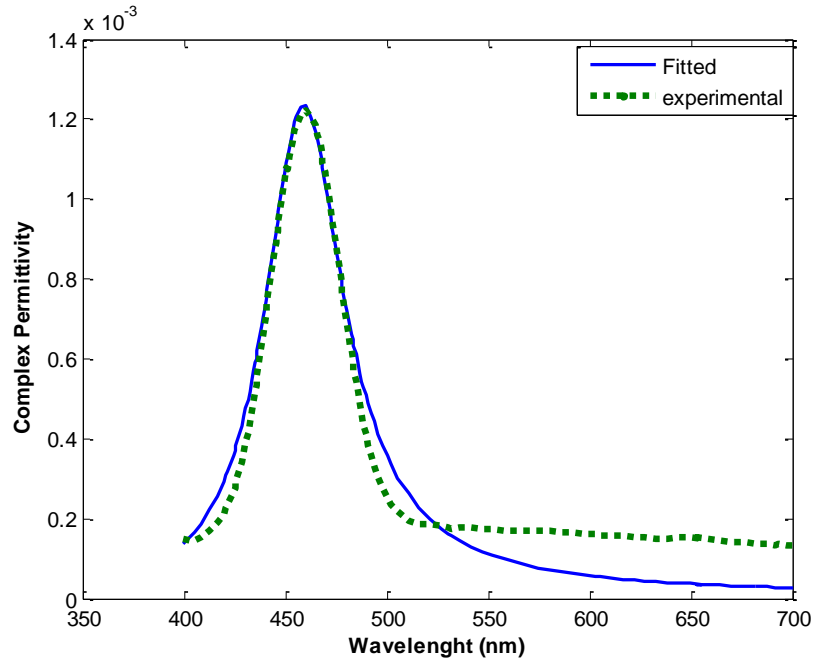


Figure 4.5 Imaginary part of permittivity of YAG: Ce³⁺.

The source of blue light is modeled by considering the dipole sources with random phases in the GaN layer. The linewidth of emission spectrum of blue GaN source is 20 nm which is defined by line shape functions. The time domain signal of blue GaN source is shown in the Figure 4.6. It is obvious that source is a continuous wave having range of frequencies components with its own amplitude defined by line shape models. The spectrum of source is also shown in the Figure 4.7.

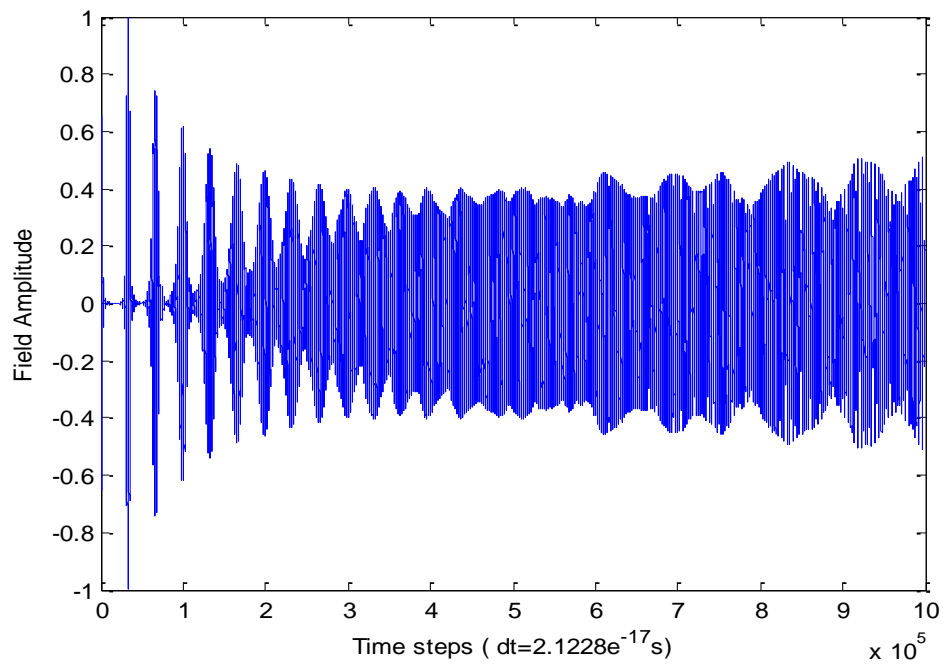


Figure 4.6 Time domain signal of blue source emitted from GaN layer.

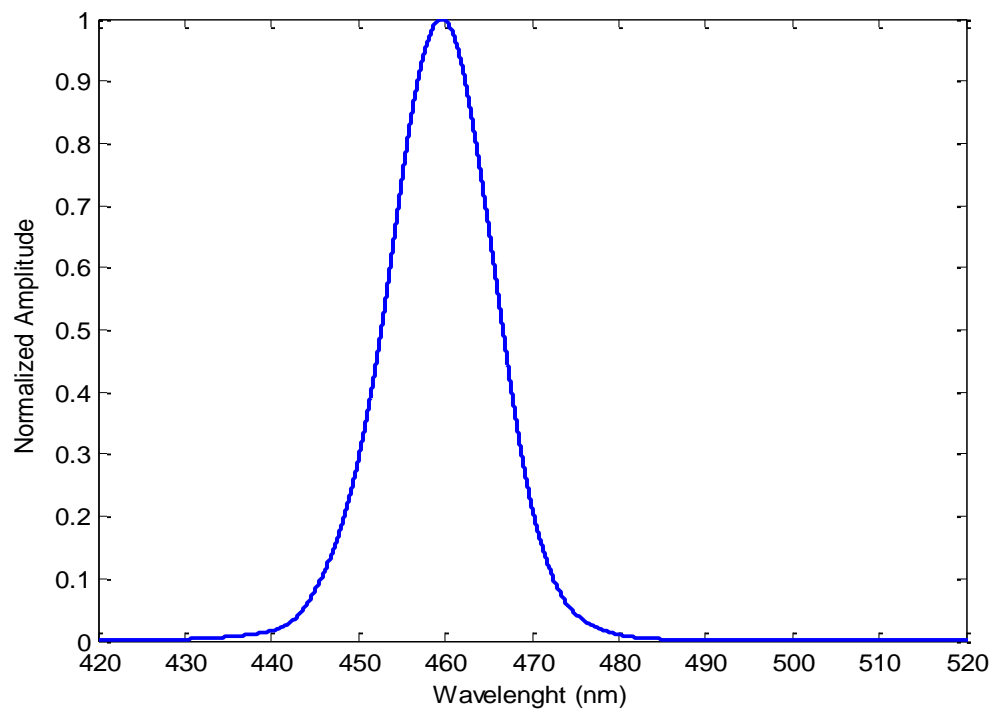


Figure 4.7 Spectrum of Blue Light Source emitted from GaN layer.

The yellow phosphor material defined by four level rate equation model is pumped with blue GaN source via optical pumping mechanism to observe the population dynamics of different energy levels. The time evolution of the population density N_2 at certain spatial location in the phosphor layer is shown in Figure 4.8. It is obvious that the population density increases with time and reaches the steady state values according to the relaxation time between the energy states responsible for emission. The steady states values of population densities in the phosphor layer are different at each spatial location due to different absorption. The light absorbed by phosphor layer at each spatial location is different due to incoming random light emitted by GaN layer.

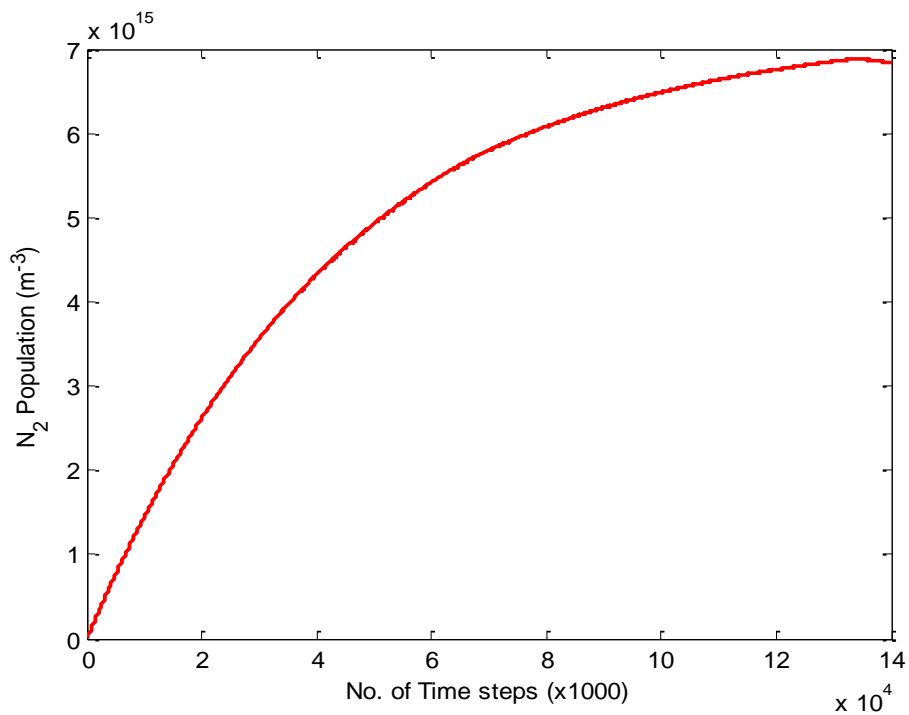


Figure 4.8 Time evolution of N_2 population.

The energy levels in four level rate equation model are quantized in nature. As a result, the emitted light from E_2 contains a set of emission wavelengths instead of single

wavelength. There are certain factors that contribute to broadening the final emission spectrum as explained in lineshape models section of this chapter. The strength of spontaneous emission is determined by the population density of N_2 . Therefore, it is assumed that the amplitude of N_2 population is varied as a function of wavelength. The variation in amplitude of N_2 is defined by lineshape functions using combined contribution of Gaussian and Lorentzian functions as shown in Figure 4.9. The central emission wavelength has maximum amplitude as compared to the others.

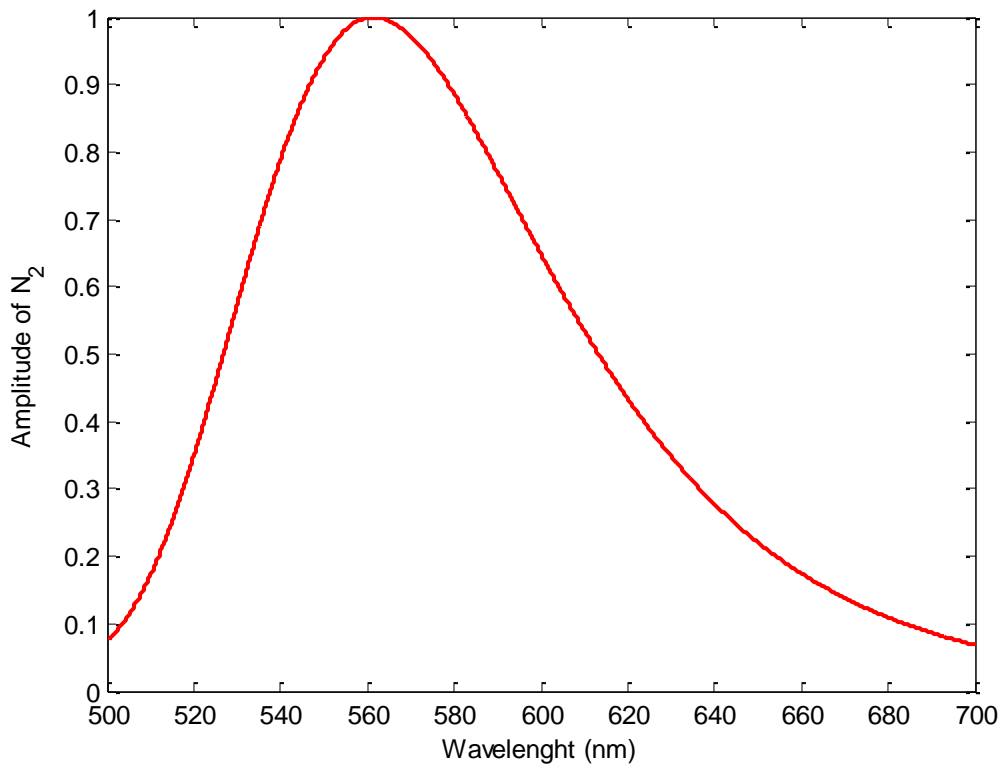


Figure 4.9 Amplitude of N_2 as function of emission wavelengths.

The luminance saturation effect is modeled by Weibull distribution function using the density of Ce^{3+} sites in phosphor layer as shown in Figure 4.10. The intensity of emitted light is increased with the increase in number of emission sites in phosphor layer. To

saturate the intensity, the number of emitting Ce^{3+} sites at saturation point (n_s) are defined in the function. The shaping parameter is defined in such a way that the saturation factor C_{sat} is decreased with the increasing the Ce^{3+} sites to make the output intensity constant after the saturation point. The shaping parameter value is varied between 1 and 2 in this distribution function. The saturation factor with the occupied Ce^{3+} sites at saturation level 5% and shaping parameter 1.4 is considered in this work as shown in Figure 4.10.

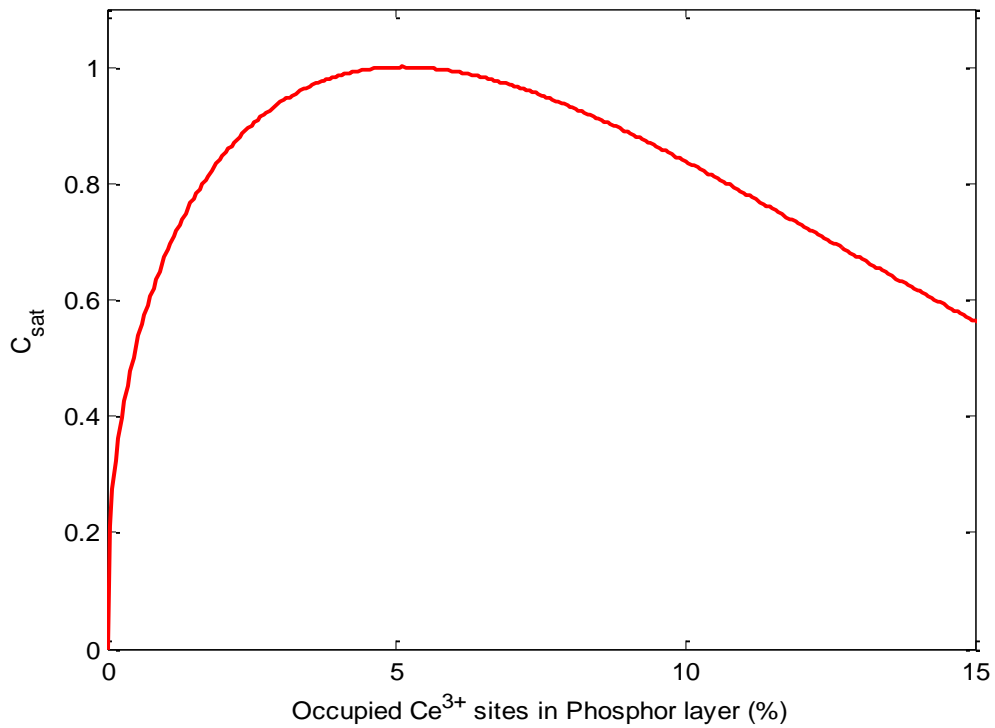


Figure 4.10 Variation of saturation factor with occupied emission sites.

The emission spectrum of $\text{YAG}:\text{Ce}^{3+}$ is calculated with and without saturation factor. In the absence of saturation factor, the spectral emission power is continuously increased with increasing number of Ce^{3+} sites in the phosphor layer as shown in Figure 4.11. On the other hand, the emission is not increased after saturation density of Ce^{3+} due to introduction of the saturation factor in the current density as shown in Figure 4.12.

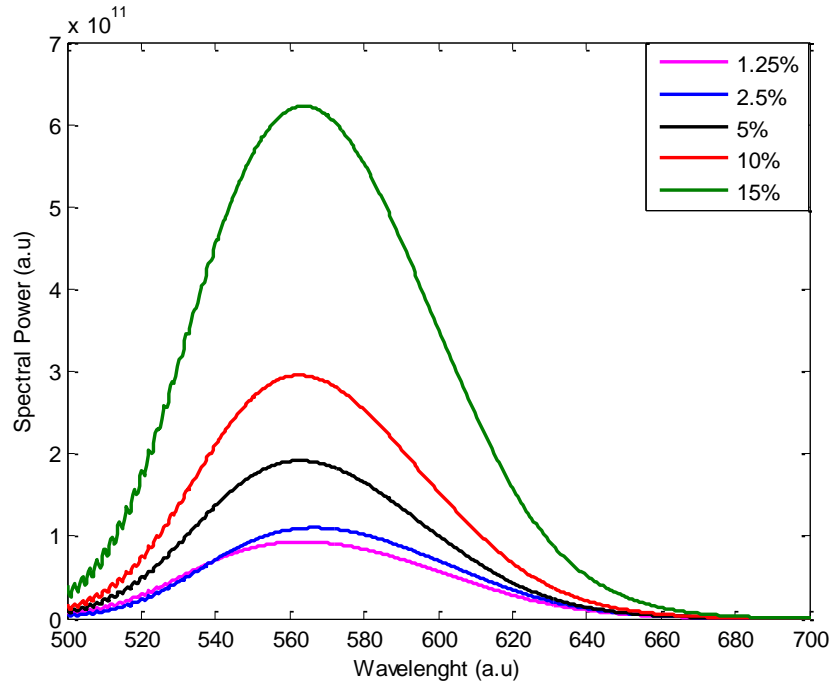


Figure 4.11 Emission Spectrum of YAG: Ce³⁺ for different occupied Ce³⁺ sites (%) without saturation.

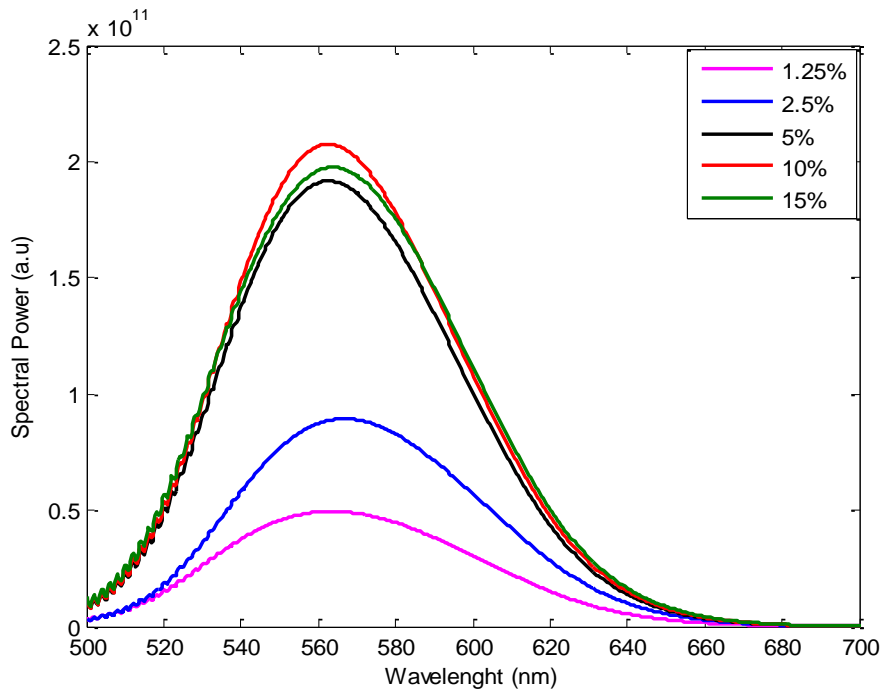


Figure 4.12 Emission Spectrum of YAG: Ce³⁺ for different occupied Ce³⁺ sites (%) with saturation

The final output intensity of yellow phosphor is also shown in Figure 5.13. It is obvious that the output intensity is first increased with number of occupied emitting Ce^{3+} sites and after saturation point, the output intensity is constant irrespective of the number of occupied Ce^{3+} sites in the phosphor layer.

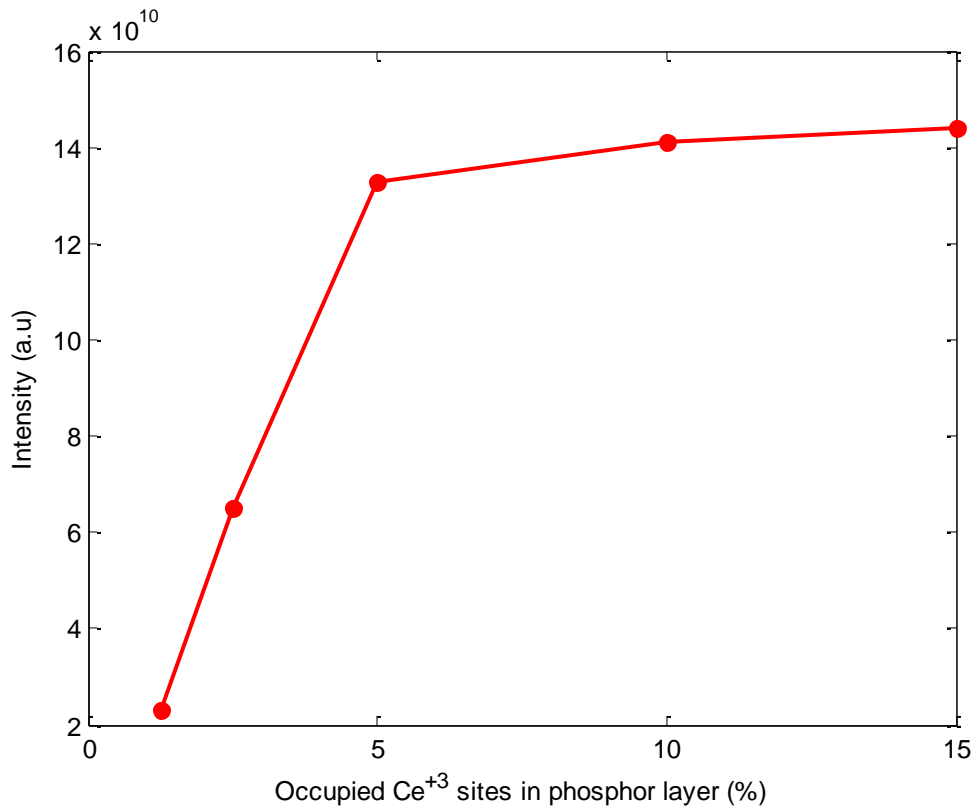


Figure 4.13 Output Intensity of YAG: Ce^{3+} for different occupied sites.

The final output spectrum of phosphor converted white LED is calculated as shown in Figure 4.14. It is obvious that output light contain both the unabsorbed blue light of GaN layer and converted broadband yellow light emitted from YAG: Ce^{3+} layer. As a result, the output covers the entire visible region which makes these LEDs useful for many indoor and outdoor applications.

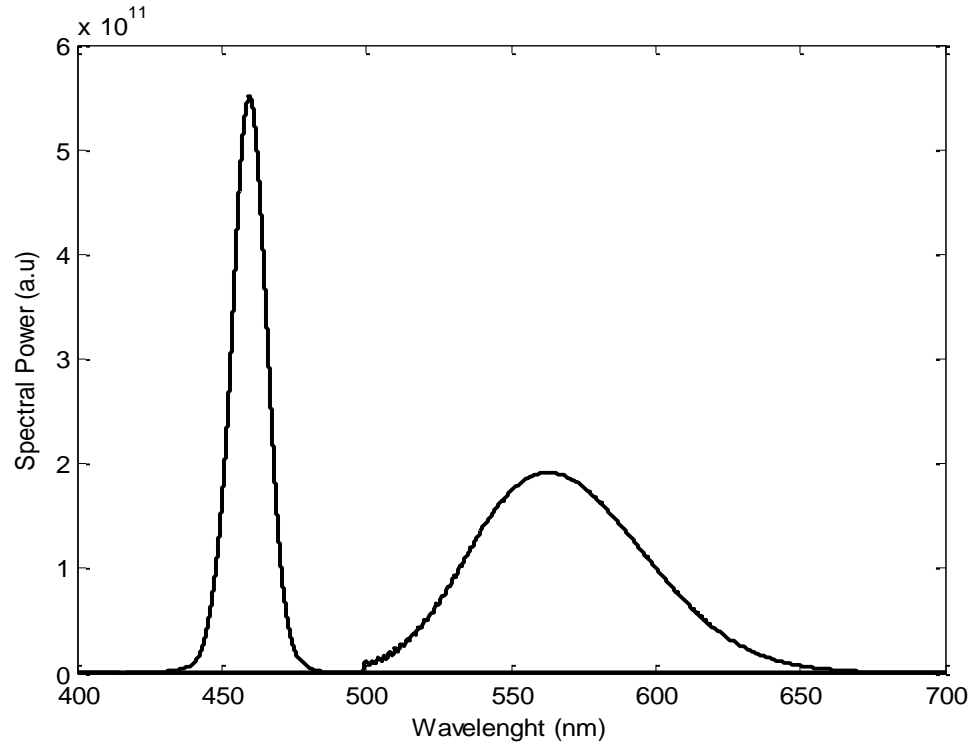


Figure 4.14 Output Spectrum of white LED for 5%age occupied sites.

4.3 Summary and Discussion

The different steps for modeling the yellow phosphor converted GaN LEDs are described in this chapter. The material specific rate equations are used to model the electron transitions processes among different energy levels. The coupling procedure for interaction of rate equation model and Maxwell's equations is discussed using current density function in terms of dipole sources. The broadening of emission spectrum is represented by line shape functions. The concept of saturation in yellow phosphor is introduced on the basis of density of the Ce^{3+} sites. The final output of white LED shows that the proposed model has a capability to give physical insight of white light generation phenomena based on phosphor material.

CHAPTER 5

PLASMONIC STRUCTURES FOR ENHANCED WHITE

LIGHT GENERATION

This chapter highlights the importance of plasmonic structures for enhanced white light conversion. The scattering properties of metallic nanoparticles and rectangular arrays are studied at a particular wavelength. It also investigates the plasmonic effect of metallic nanostructures on white light conversion process in yellow phosphor (YAG:Ce) coated GaN LEDs. The silver rectangular array configuration is designed at the emission wavelength of GaN LED to enhance the yellow emission of phosphor converted GaN LED.

5.1 Overview of Plasmonics for enhanced field confinement

Plasmonics is a booming area of science and technology that explores the interaction of light with nano-metallic surfaces to manipulate light at subwavelength scales. The distinct properties of nano-metallic structures to maneuver the light are derived from an ability to support collective electromagnetic excitations whose field is confined to near the locality of metal-dielectric interface, known as surface plasmons. In recent years, the research advances in the plasmonics field allowed new science and device technologies and offered dramatic growth in plasmonic applications. Plasmonics may perhaps become

a prevalent technology in few years due to its unusual optical capabilities to accomplish extraordinary levels of interaction between electronic and optical areas. Although there are some inherent resistive heating losses associated with plasmonics due to metals which affect the performance of optical devices, still many useful applications of this technology have recently been realized. The excellent examples are nanoantennas, lenses and resonators and structures for light enhancement and confinement.

The dielectric lenses and resonators have been traditionally used to confine light and enhance the local field intensities. Due to the fundamental laws of diffraction, these devices are unable to confine and enhance the light at subwavelength scale. The metallic nanostructures based devices do not have these limitations in confining light due to their different nature as compared to dielectric counterparts. They have the ability to transform electromagnetic radiations into intense localized fields through surface plasmons. Various plasmonic structures such as nanogrooves, nanospheres, nanocones and bow-tie antenna to confine and enhance the electromagnetic field have been investigated both experimentally and analytically. It has been shown that electromagnetic field can be enhanced 10^2 - 10^3 times due to resonant plasmon oscillations in these structures. Two gold rectangular rods were used to enhance the local field strength around 200 times at a wavelength of 830 nm as reported in [41]. The field enhancement up to 160 times at a wavelength of 700 nm using gold prisms was demonstrated in [42]. In [43], gold and silver grooves were used to achieve the 20–30 times local field enhancement at the wavelengths of 620–670 nm and 27–29 times enhancement at wavelengths of 550–570 nm respectively. The realization of this effect considerably depends on the design of

metallic nanostructures which control the interaction between light and surface plasmon modes to yield the interesting optical effects in integrated photonic devices.

5.2 Plasmonics cavities for enhanced field confinement

The concept of plasmonic cavities is used to enhance and confine the electromagnetic field by embedding the silica nanoparticles in nano-metallic film [44]. The proposed structure for enhanced field confinement is shown in Figure 5.1. The configuration consists of silicon, silver and air layers. The silica nanoparticles of 40 nm radius are partially embedded between silicon and silver interface. The thickness of Ag metallic film is 100 nm and the spacing between the nanoparticles is varied from 10 nm to 90 nm.

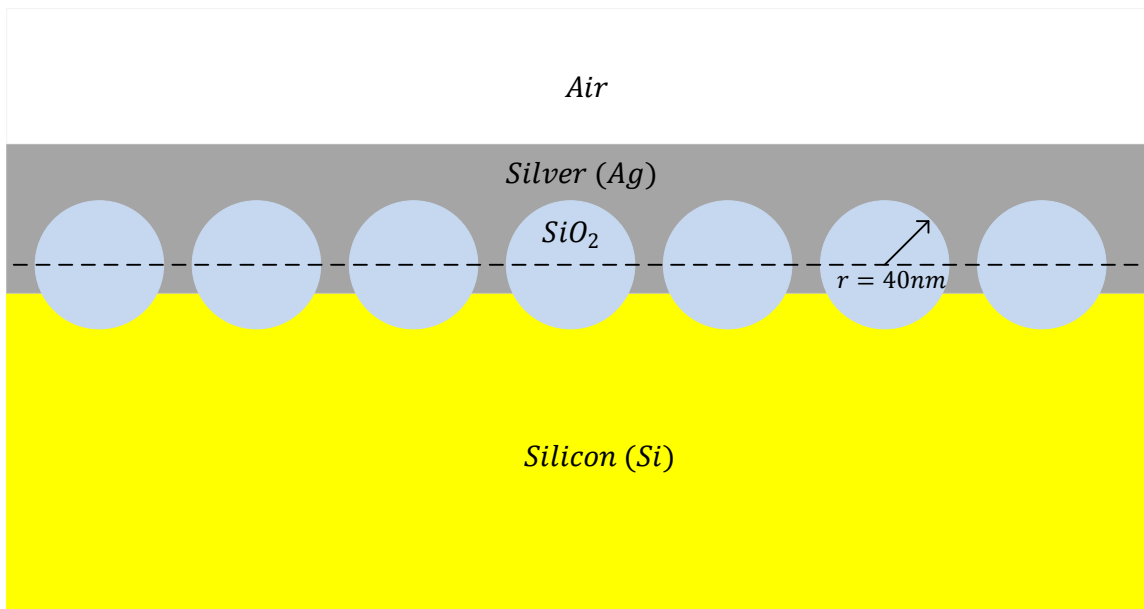


Figure 5.1 Structure of SiO₂ nanoparticles embedded in Ag Film.

When an incident wave strikes the interface between the silicon and the nanoparticles it gets trapped inside the nanoparticles by the lensing effect, and surface plasmon polaritons (SPPs) are excited within the cavities. These cavities enhance the electromagnetic field due to localized surface plasmon resonance (LSPR) and cavity resonance. The resonance condition of plasmonic cavities at a particular wavelength is matched by tuning the shape, size and spacing between the nanoparticles.

5.2.1 Enhanced Optical Confinement

Enhanced optical confinement can be described using enhancement factor which is defined as intensity within the nanoparticles with Ag metallic film divided by corresponding intensity within the nanoparticles without Ag metallic film:

$$F_{\lambda} = \frac{I_{\lambda,with Ag}}{I_{\lambda,without Ag}} \quad 5.1$$

The value of F_{λ} determines the enhancement in intensity within the nanoparticles at given wavelength in presence of plasmonic cavities. The silica nanoparticles behave like plasmonic cavities in the presence of silver metallic film due to excitation of surface plasmons. Therefore, it is essential to determine the resonance frequency of these cavities to confine light efficiently. To calculate the resonances of the plasmonic cavities, an isolated nanoparticle is considered in the presence of silver layer and the result is shown in Figure 5.2.

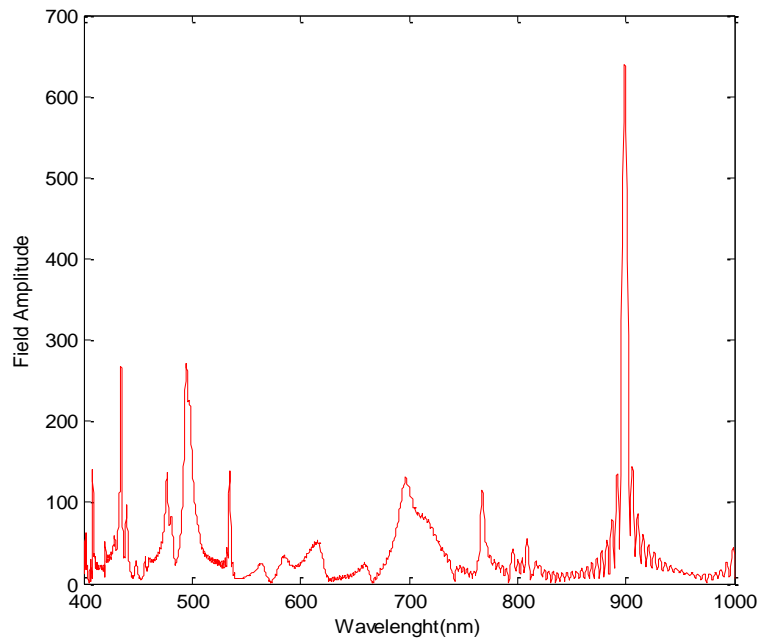


Figure 5.2 Resonance of Plasmonic cavity.

It is evident from Figure 5.2 that resonance frequency of a nanoparticle of radius 40 nm is 3.38×10^{14} Hz corresponding to the wavelength 898.7 nm. The resonance wavelength of the nanoparticles is dependent on the location and size of nanoparticle embedded in silver layer.

A continuous wave (CW) excitation is applied at resonance frequency of plasmonic cavity to calculate the intensity of the trapped field within the silica nanoparticles. The intensity is calculated within the nanoparticles with Ag metallic film and without metallic film as shown in Figure 5.3. The radius of nanoparticle is 40 nm and spacing between the particles is 50 nm. The sharp peaks show that energy is confined within the nanoparticles due to surface plasmon resonances. It is observed that intensity is enhanced over a hundred times as compared to intensity in the absence of plasmonic resonance.

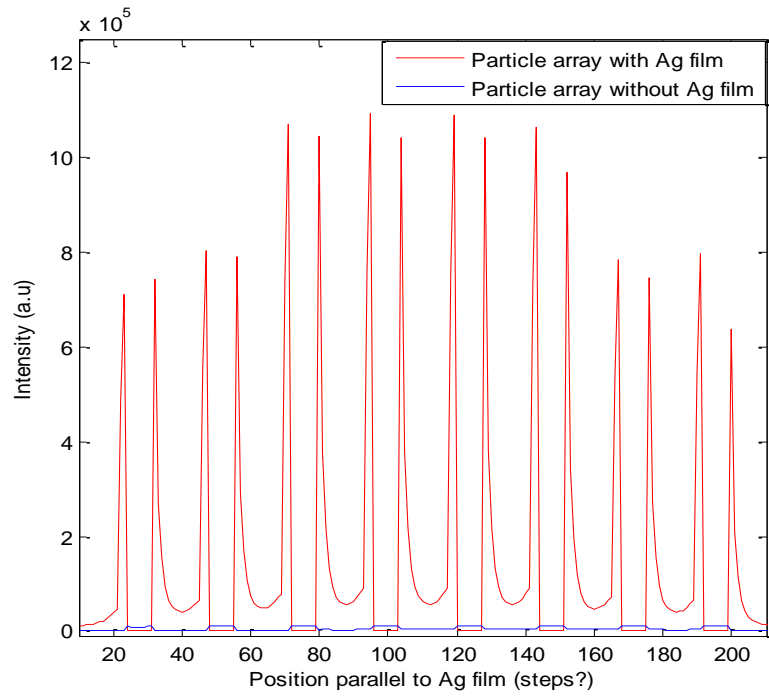


Figure 5.3 Variation of intensity inside plasmonic cavities with position.

The intensity profiles within the nanoparticles in the presence and absence of metallic silver film are also shown in Figure 5.4 and Figure 5.5.

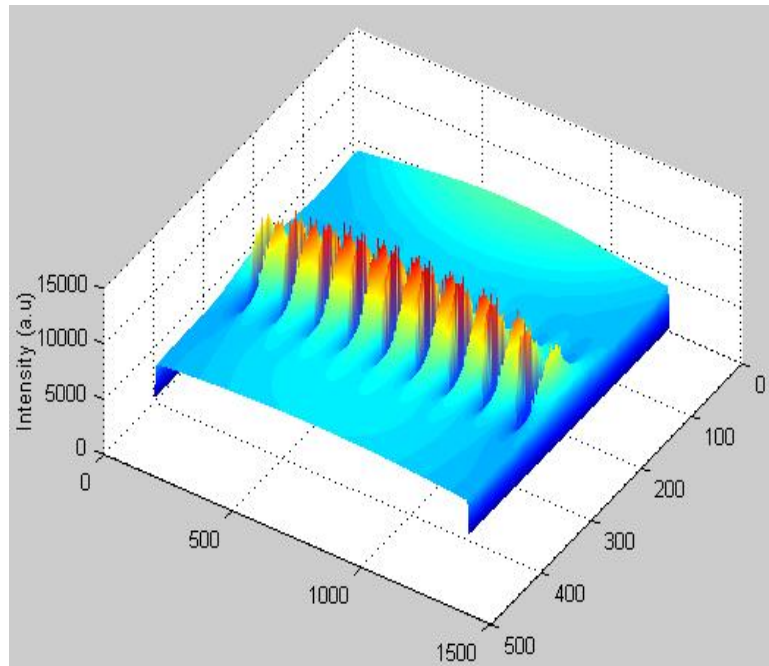


Figure 5.4 Intensity profile without the metallic silver film.

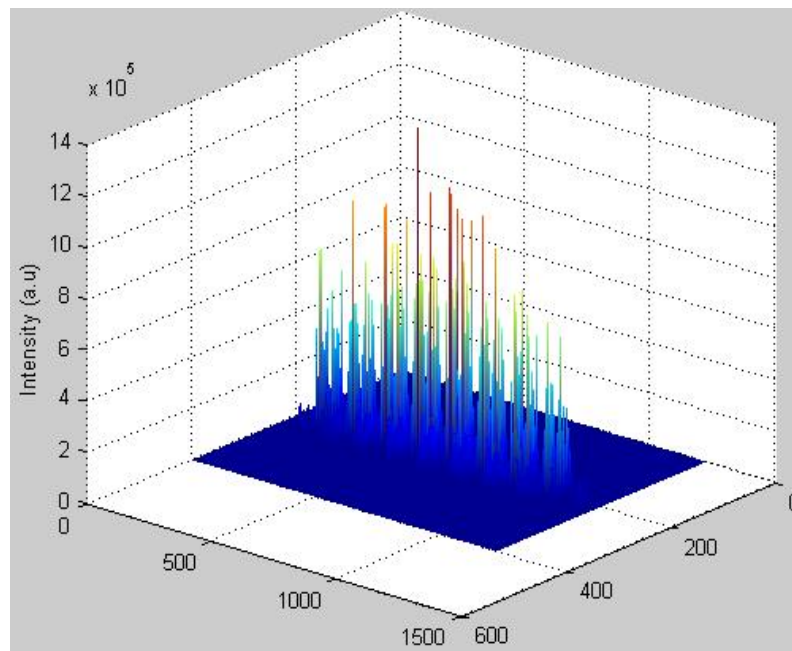


Figure 5.5 Intensity profile with metallic silver film.

The enhancement factor is determined as a function of wavelength as shown in Figure 5.6. It is found that the maximum enhancement factor is obtained by matching the resonance condition at 898.7 nm for nanoparticles of radius 40 nm with interparticle spacing 50 nm. The off resonance wavelength are unable to resonate the cavities which result in small optical enhancement and confinement of the optical field.

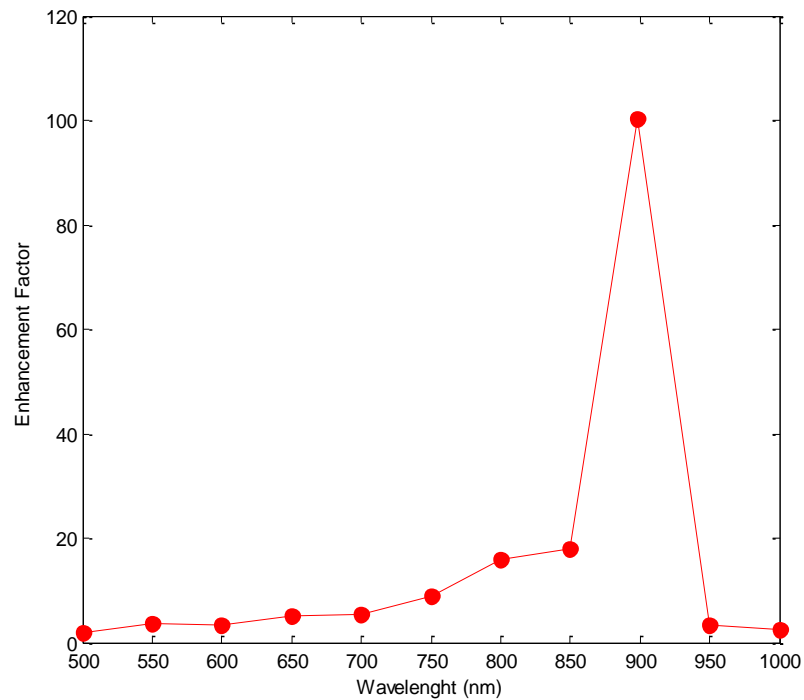


Figure 5.6 Variation of enhancement factor with wavelength.

The enhancement factor is also determined as a function of spacing between the particles to optimize the interparticle spacing as shown in Figure 5.7. The structure is excited at resonance frequency and enhancement factor is calculated for varying the spacing between the nanoparticles from 10 nm to 90 nm. The enhancement factor is found to be small in range of 10-30 nm spacing and increased significantly with increasing the interparticle spacing due to the decrease in the intensity in the absence of metallic film. It

is observed that the maximum enhancement is obtained at 50 nm spacing between the particles as shown in Figure 5.7. Thus, optimal value of interparticle spacing is found to be 50 nm for plasmonic cavity of radius 40 nm.

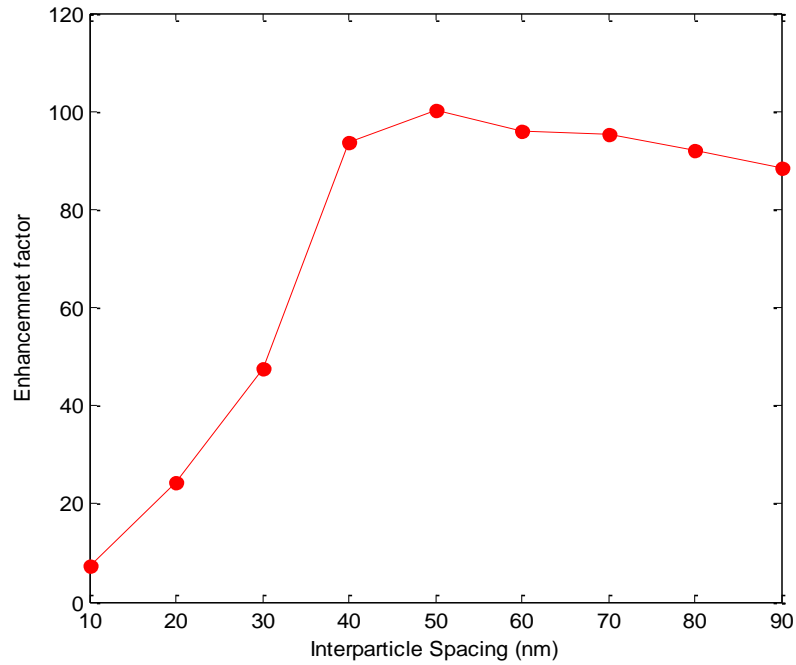


Figure 5.7 Variation of enhancement factor with interparticle spacing.

5.3 Scattering Properties of metallic nanoparticles

The color effects due to colloidal Gold particles are firstly explained in the famous paper published by Gustav Mie in 1908 [45]. He gave a first outline of how Maxwell's electromagnetic theory can be applied to compute light scattered by small spherical particles. With his first computations he succeeded to explain the color of gold colloids changing with diameter of the Gold spheres, which was later interpreted in terms of surface plasmon resonances. According to Mie theory, the scattering and extinction cross

sections of spherical particles with diameters smaller than the wavelength of light are defined as

$$\sigma_{sca} = \frac{2\pi}{|k|^2} \sum_{L=1}^{\infty} (2L + 1)(|a_L|^2 + |b_L|^2) \quad 5.2$$

$$\sigma_{ext} = \frac{2\pi}{|k|^2} \sum_{L=1}^{\infty} (2L + 1)[Re(a_L + b_L)] \quad 5.3$$

$$\sigma_{abs} = \sigma_{ext} - \sigma_{sca} \quad 5.4$$

where k is the wave vector and L is an integer representing the dipole, quadro-pole and higher multi-poles oscillations and a_L and b_L are composed of Ricatti-Bessel functions.

The scattering properties of nanoparticles are necessary to describe the response of these particles under the interaction of electromagnetic field. TFSF is used to find the scattered field response of the nano-particles.

5.3.1 Verification of scattering properties of Silver nanoparticle

Silver nanoparticles have the ability to absorb and scatter light with extraordinary efficiency. Upon the excitation by light at specific wavelength, the conduction electrons on metallic nanoparticles undergo collective oscillation, known as a surface plasmon resonance (SPR), due to strong interaction of light with these particles. The absorption and scattering intensities of silver nanoparticles are higher as compared to their identically sized non-plasmonic nanoparticles due to these surface plasmon resonances.

The different parameters such as particle size, shape, and particle surrounding local refractive index are necessary to tune for controlling the scattering and absorption properties of silver nanoparticles.

The scattering properties of a single silver nanoparticle are verified by calculating the scattering cross-section using FDTD and analytical formulation. The scattering cross-section of a silver nano-particle with a radius 40 nm placed in free-space is determined. The input source is Gaussian pulse in time centered at $\lambda = 400 \text{ nm}$ wavelength with $t_p = 0.5 \text{ fs}$ and $t_o = 3t_p$ given as;

$$\text{source pulse}(t) = \exp\left(\frac{t - t_o}{t_p}\right)^2 \cos\left(\frac{2\pi}{\lambda}(t - t_o)\right) \quad 5.5$$

The source Gaussian pulse in time domain is shown in Figure 5.8. The spectrum of the pulse covers the entire optical domain as shown in Figure 5.9. It is found that the scattering cross-section calculated using FDTD and analytically is well matched to each other as shown in Figure 5.10. The scattering cross section of a single nanoparticle has two dominant modes with resonant wavelengths at 250.8 nm and 364 nm .

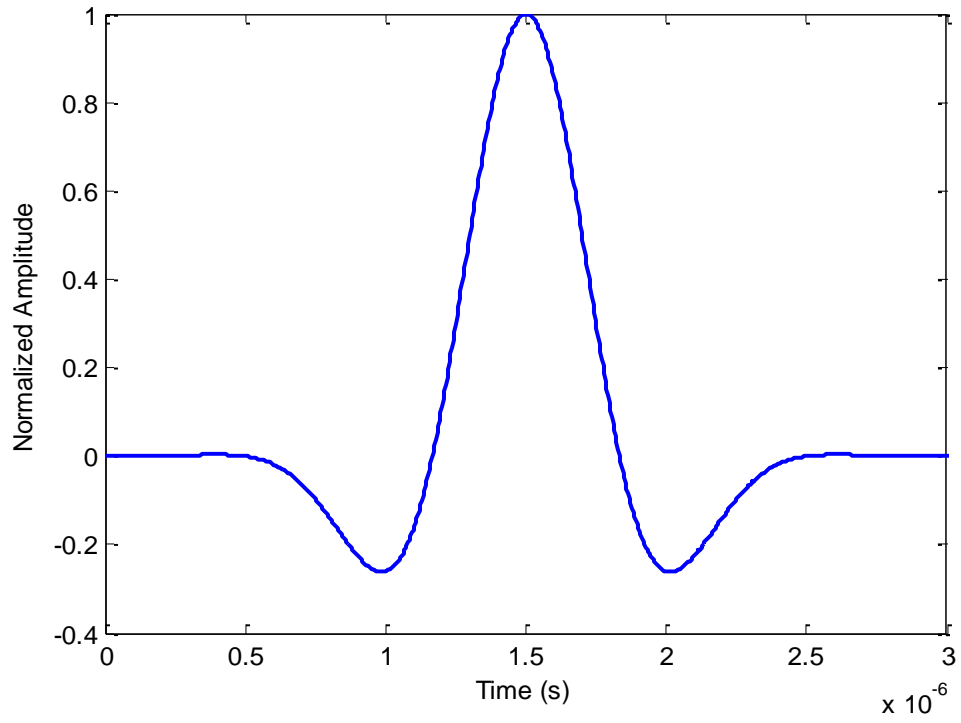


Figure 5.8 Time domain signal of modulated Gaussian with cosine

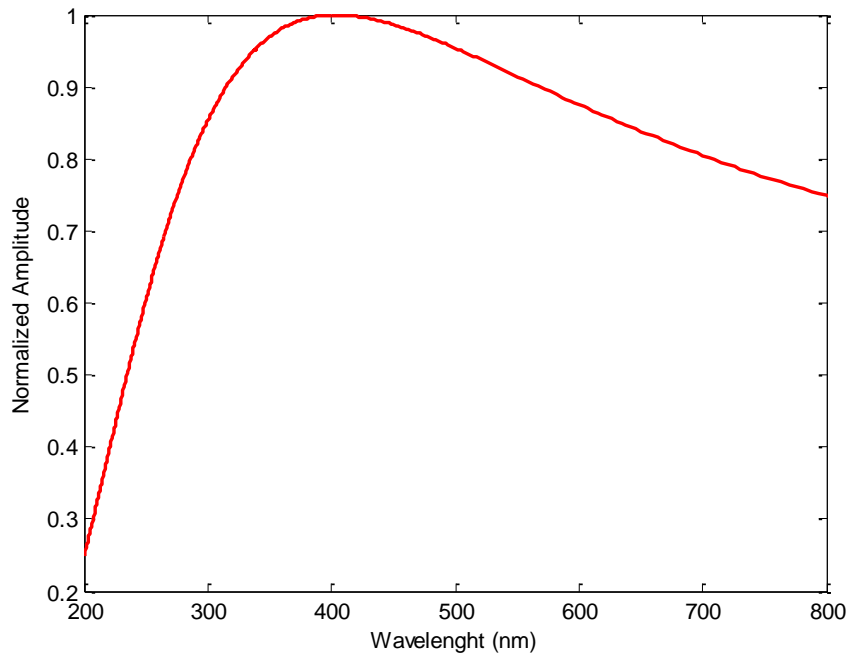


Figure 5.9 Spectrum of modulated Gaussian with cosine

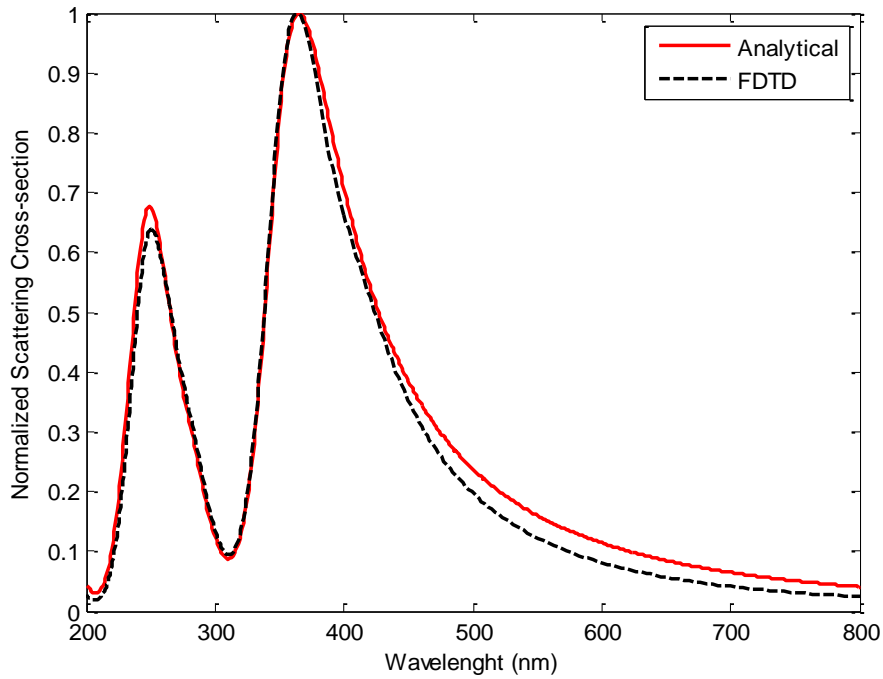


Figure 5.10 Scattering Cross-section for 40nm radius single Ag nanoparticle.

5.4 Metallic nanostructures for enhanced phosphor conversion

The emission characteristics of materials are determined by intrinsic material properties and the surroundings that interact with these materials. It means that the emission properties can also be tailored by the emission environment. In this scenario, the field of nanophotonics provides two fundamental approaches that are focused on modifying the emission environment to enhance spontaneous emission. These two approaches are based on either by controlling the density of states or introducing the intense localized electromagnetic field in the vicinity of emitting material. The density of states can be controlled using photonic crystal and intense localized electromagnetic field can be introduced using the metallic nanostructures.

The concept of intense localized electromagnetic field using metallic nanostructure is used to enhance the conversion in phosphor converted GaN LEDs. The yellow phosphor doped with cerium has strong absorption at 460 nm which is well matched with the excitation wavelength of GaN LEDs. In this situation, it is essential to find a suitable shape and arrangement of the metallic nanostructure having resonance at 460 nm to enhance the conversion process in white LEDs. The optical properties of these metallic nanostructures are dependent on features like shape, size, dielectric environment and number of particles. In this work, a periodic silver rectangular array embedded in the phosphor layer is used to enhance the emission of white GaN LEDs. Therefore, it is necessary to investigate the optical properties of silver rectangles to design a configuration that resonate with the emission wavelength of GaN LEDs.

5.4.1 Silver Rectangular Array Configuration

The resonance behavior of metallic nanostructures can easily be determined by the investigating its scattering properties using TFSF. Therefore, the first step is to study the scattering properties of single silver rectangle to design a suitable configuration that can resonate at 460 nm. The dependence of resonance wavelength of silver rectangles on features like length, height, dielectric environment and number of silver rectangle is studied to find the suitable arrangement for optimized configuration.

First, a single silver rectangle is embedded in the dielectric environment of yellow phosphor for examining its scattering properties. The height of silver rectangle is

considered 10nm and length of the silver rectangle is varied from 10 nm to 20 nm to observe how it affects its resonance behavior. The scattering cross-section of a single rectangle as a function of length is shown in Figure 5.11. It is found that single silver rectangles have a red shift with increasing length. Another test is performed on a silver rectangle by varying the height of the rectangle from 10 nm to 20 nm while considering the length 10nm.

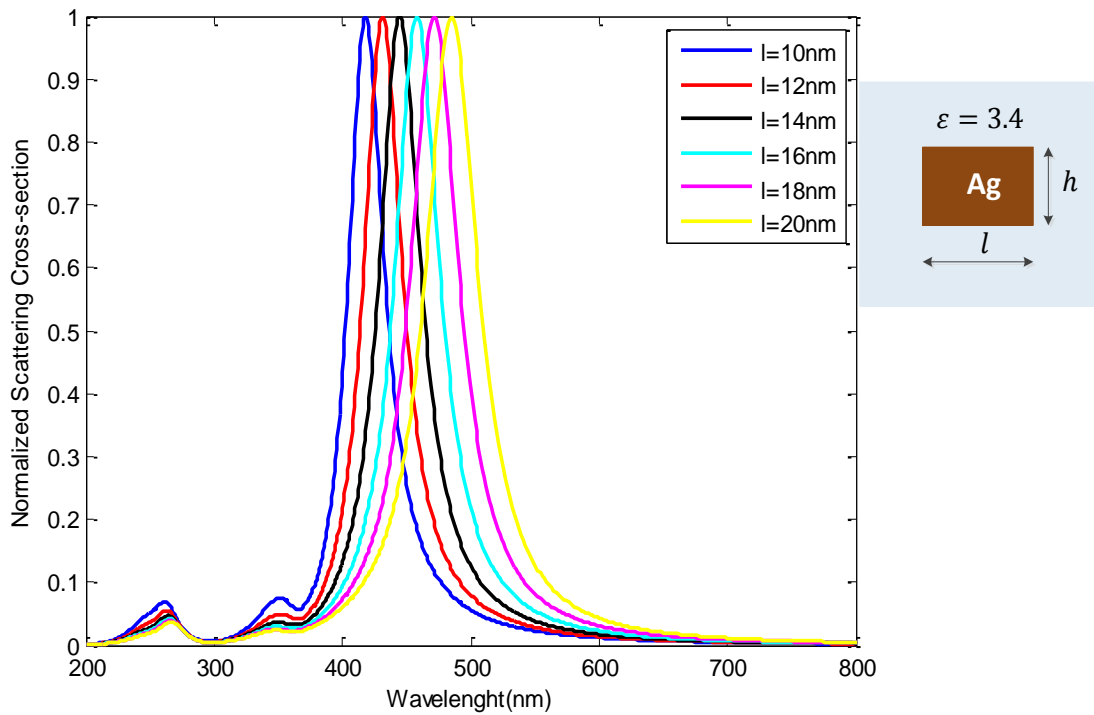


Figure 5.11 Variation of scattering cross section of silver rectangle with length.

The scattering cross-section of a single silver rectangle with the function of height is shown in Figure 5.12. It is found that the spectrum is shifted toward blue wavelength and other modes are also dominant with increasing the height of the silver rectangle.

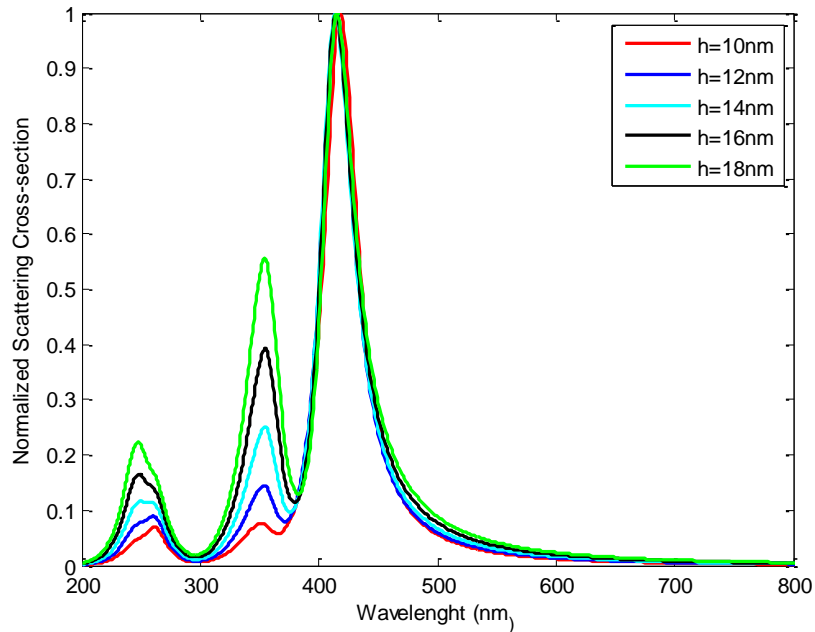


Figure 5.12 Variation of scattering cross section of silver rectangle with height.

Another configuration by embedding two silver rectangles in yellow phosphor medium for examining the scattering properties is tested. The height and length of the silver rectangles are 10 nm. The spacing between two rectangles is varied from 10 nm to 20 nm to observe resonance behavior. The scattering cross-section of two rectangles as a function of spacing between rectangles is shown in the Figure 5.13. It is found that scattering cross-section have the blue shift with increasing the distance between two rectangles. It is also obvious that the spectrum of scattering cross-section is sharpened with increasing the distance.

Another configuration by increasing the embedded number of silver rectangles (N_p) in yellow phosphor medium for examining the scattering properties is tested. The height,

length and spacing between silver rectangles are 10 nm. The parameter that is varied is number of silver rectangles. The scattering cross section of the silver rectangles with increasing number of the rectangles is shown in Figure 5.14. It is found that the scattering cross-section have a red shift with increasing number of particles. It is also observed that the spectrum of scattering cross-section is also broadened with the increasing number of rectangles.

With this experience in hand regarding the resonance behavior of the silver rectangles, a configuration has been designed which has a resonance close to the emission wavelength of the GaN LEDs. The configuration is based on embedding an array of silver rectangles in yellow phosphor with length, height and equidistant spacing of 16 nm, 12 nm and 30 nm as shown in Figure 5.15.

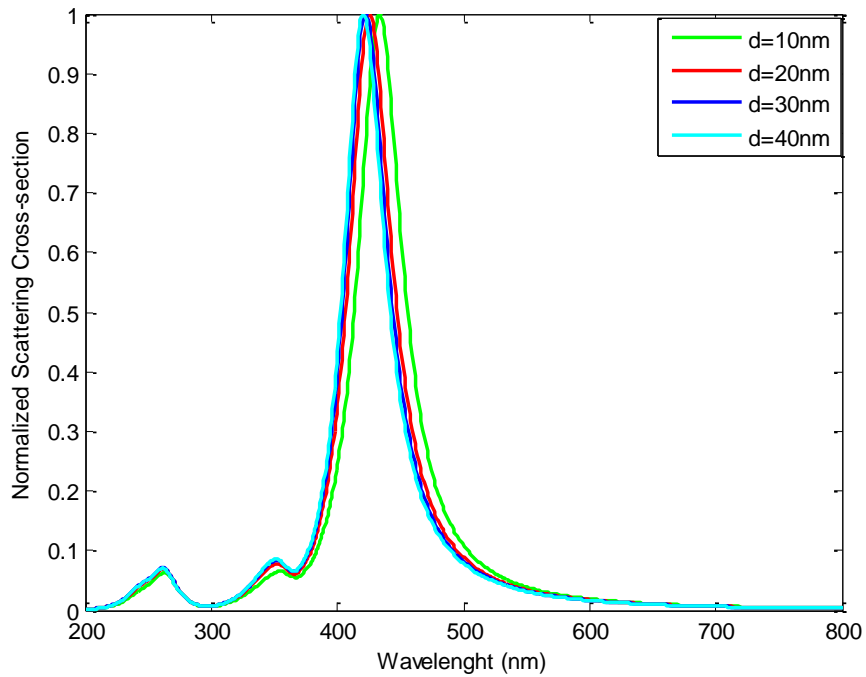


Figure 5.13 Variation of scattering cross section with spacing between two silver rectangles.

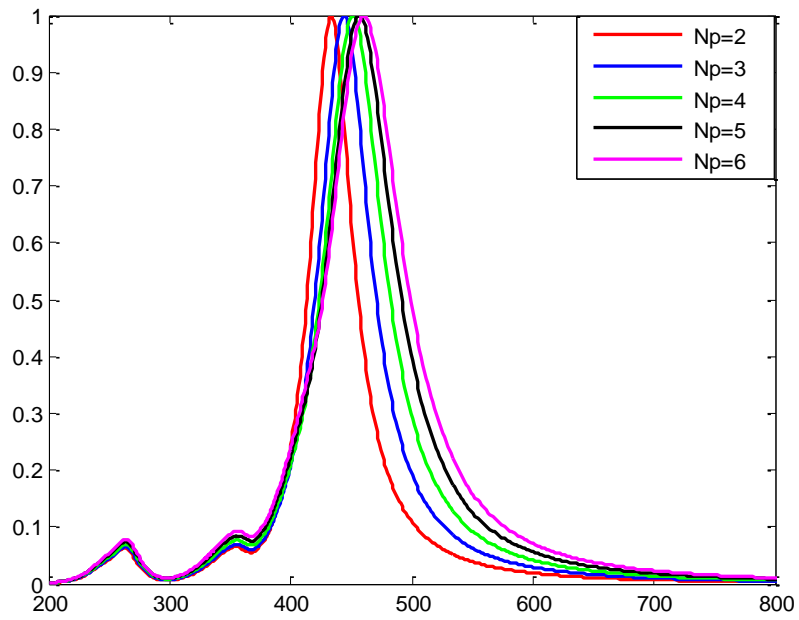


Figure 5.14 Variation of scattering cross section with number of silver rectangles.



Figure 5.15 Optimized Configuration with silver rectangles embedded in phosphor layer.

The scattering cross-section of the optimized configuration is determined as shown in the Figure 5.16. It is found that the configuration has the resonance at 459.6 nm which is very close to the emission wavelength of 460 nm.

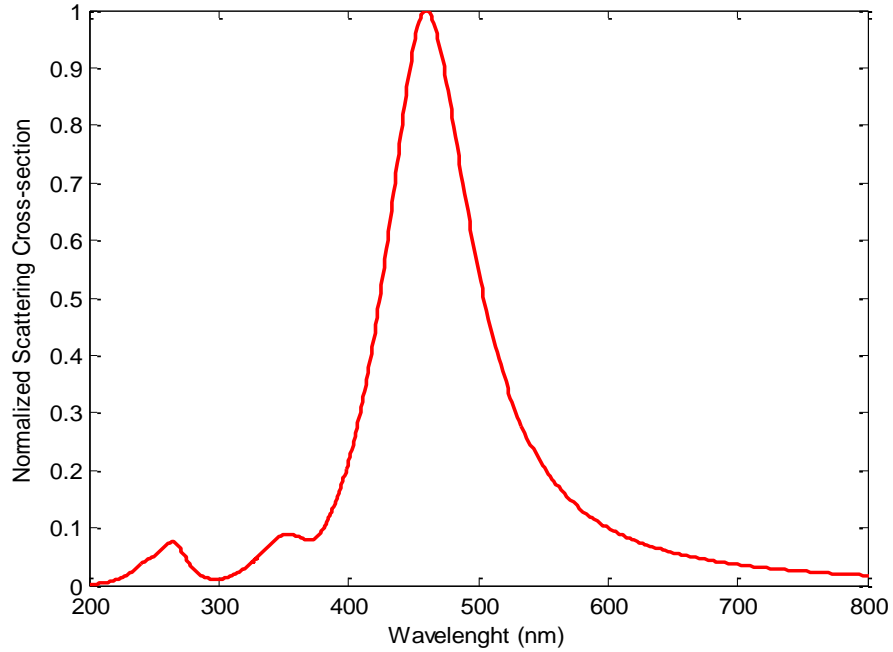


Figure 5.16 Scattering cross section of optimized configuration.

5.4.2 Plasmon-enhanced Conversion in phosphor converted GaN LEDs

The optimized arrangement of rectangular silver is integrated with the basic structure of phosphor converted white LEDs as shown in Figure 5.17. The silver rectangular array is embedded into the phosphor layer to change the emission environment by resonating the silver array at 460 nm with the incoming light from GaN layer. Most of the light emitted from the GaN layer is collected by the metallic rectangular array due to resonance. It is found that the population of energy level N_2 is increased significantly near the rectangular arrays due to intense localized electromagnetic field. This intense

electromagnetic field is produced due to the surface plasmons created by resonating the metallic nanostructure. As a result, the conversion of yellow light is enhanced in the presence of metallic rectangular arrays.

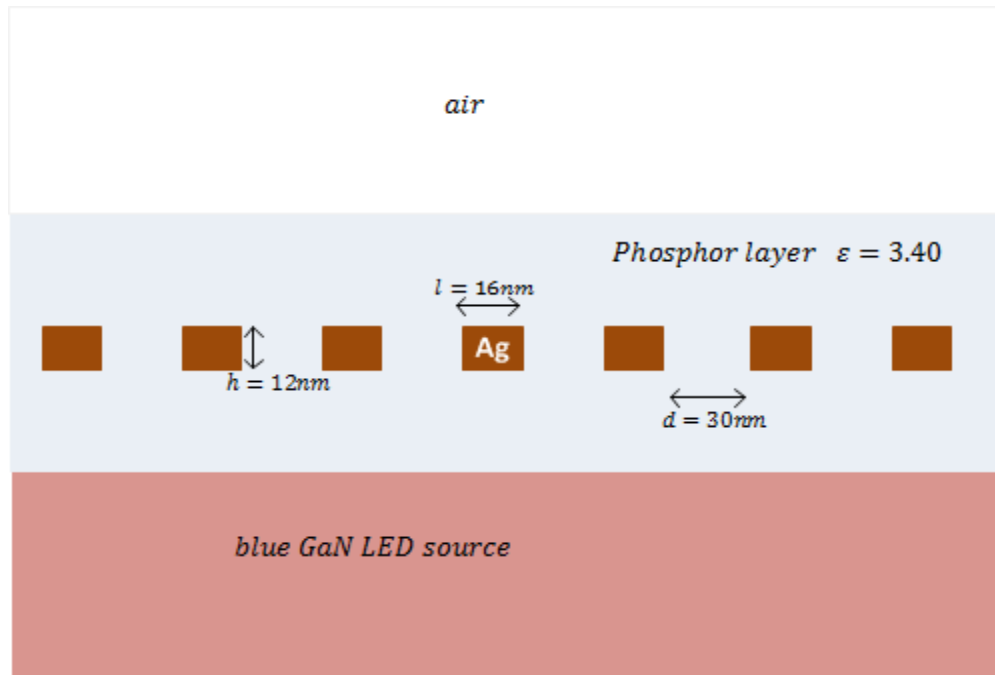


Figure 5.17 Structure with silver rectangles for phosphor converted white LEDs.

The emission spectrum of yellow phosphor is determined with and without the plasmonic structure as shown in the Figure 5.18 and Figure 5.19 respectively. It is observed that the emission is increased by increasing the number of occupied sites in the phosphor layer. It is also found that the emission is enhanced in the presence of the plasmonic structures due to strong electromagnetic field in the vicinity of the rectangular array.

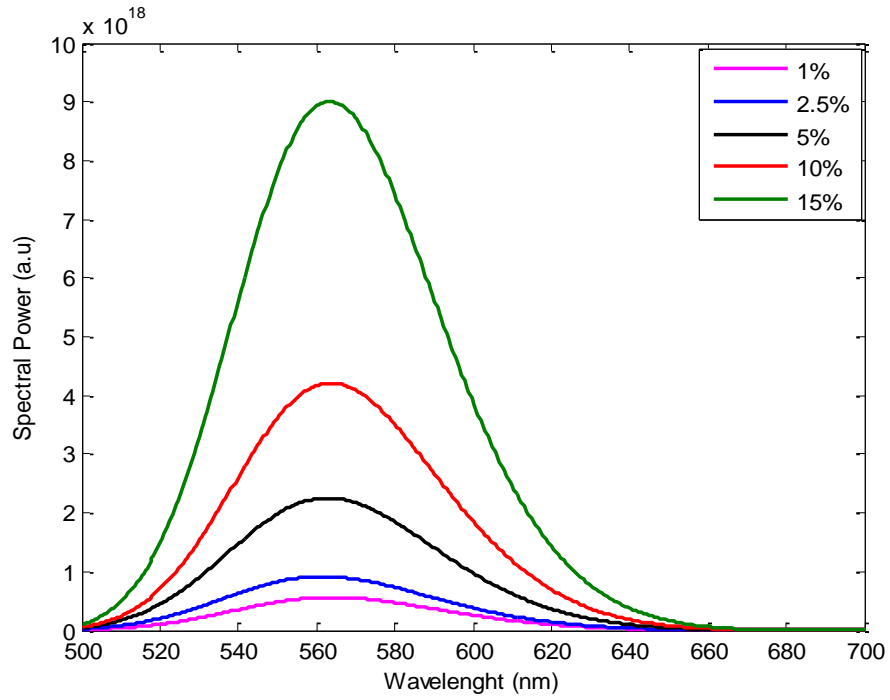


Figure 5.18 Emission Spectrum of YAG: Ce³⁺ without saturation and no plasmonic array.

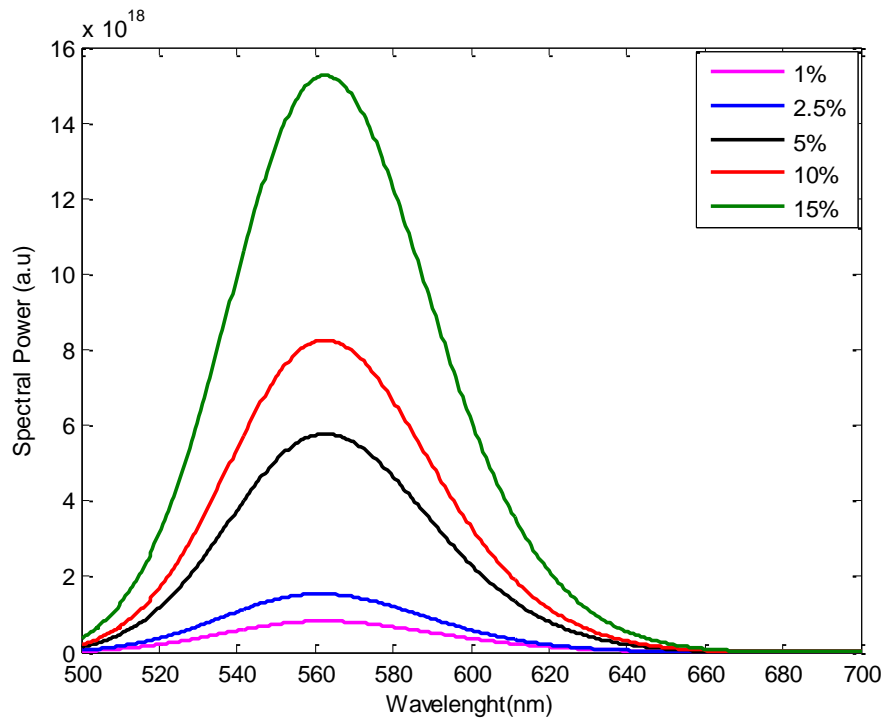


Figure 5.19 Emission Spectrum of YAG: Ce³⁺ without saturation and presence of plasmonic array.

The emission spectrum of the yellow phosphor is also determined for both cases with and without plasmonic array and introducing the saturation effect as shown in Figure 5.20 and Figure 5.21 respectively. The saturation density of Ce^{3+} for both cases is considered 5% which is defined on the basis of number of occupied Ce^{3+} sites in the phosphor layer. It is found that the emission almost remains constant after saturation density of Ce^{3+} for both cases.

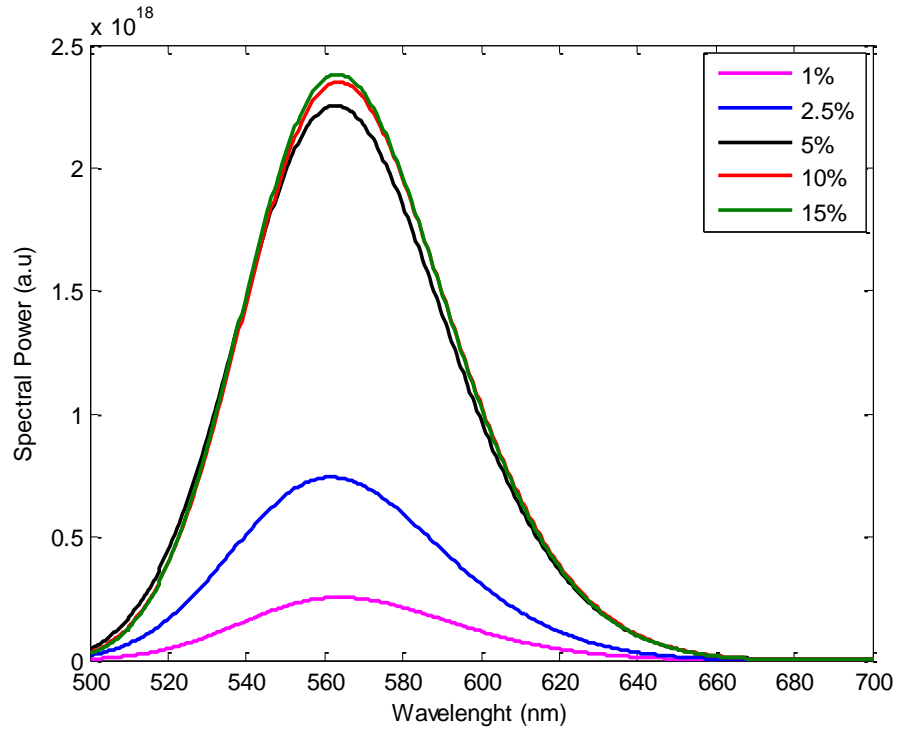


Figure 5.20 Emission Spectrum of YAG: Ce^{3+} with saturation and no plasmonic array.

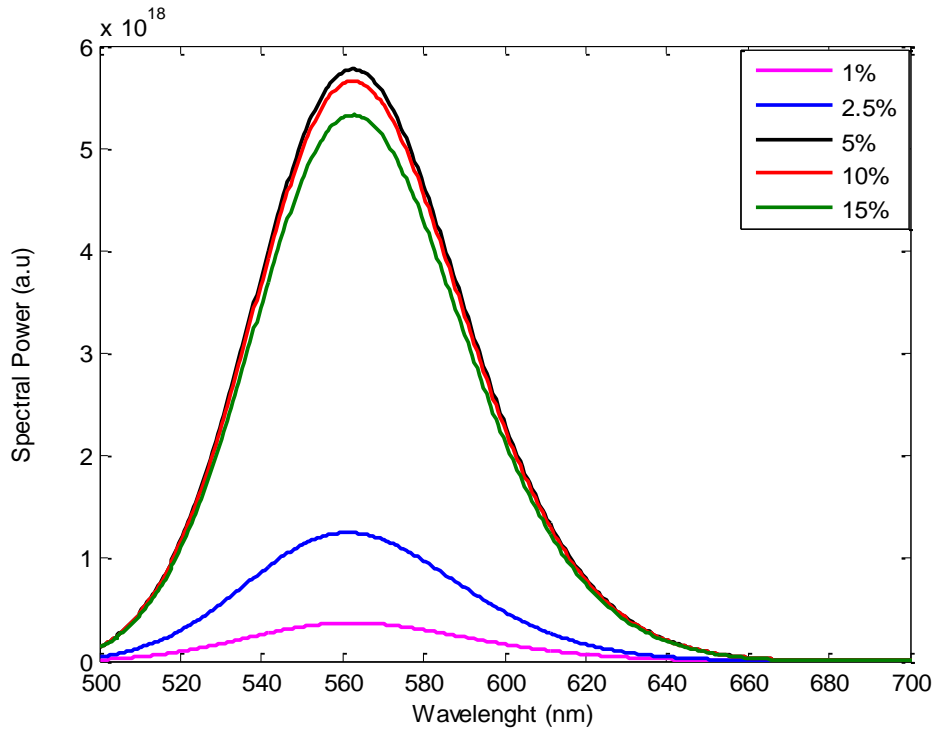


Figure 5.21 Emission Spectrum of YAG: Ce³⁺ with saturation in presence of plasmonic array.

The emission intensity with incorporating the saturation effect is also calculated as shown in Figure 5.22. The intensity of YAG:Ce³⁺ increases with density of Ce³⁺ sites in the phosphor layer until it reaches constant values after the saturation point. The output of the yellow phosphor converted GaN LED with and without plasmonic array is shown in Figure 5.23 and Figure 5.24 respectively. It is found that the conversion is enhanced in the presence of metallic array due to localized surface plasmons. The comparison of final output spectrum for white LED is shown in Figure 5.25. In case of plasmonic array, more blue light is absorbed by metal doped phosphor due localized surface plasmon resonance and, as a result, the converted yellow light is increased as compared to without metal doping in phosphor layer.

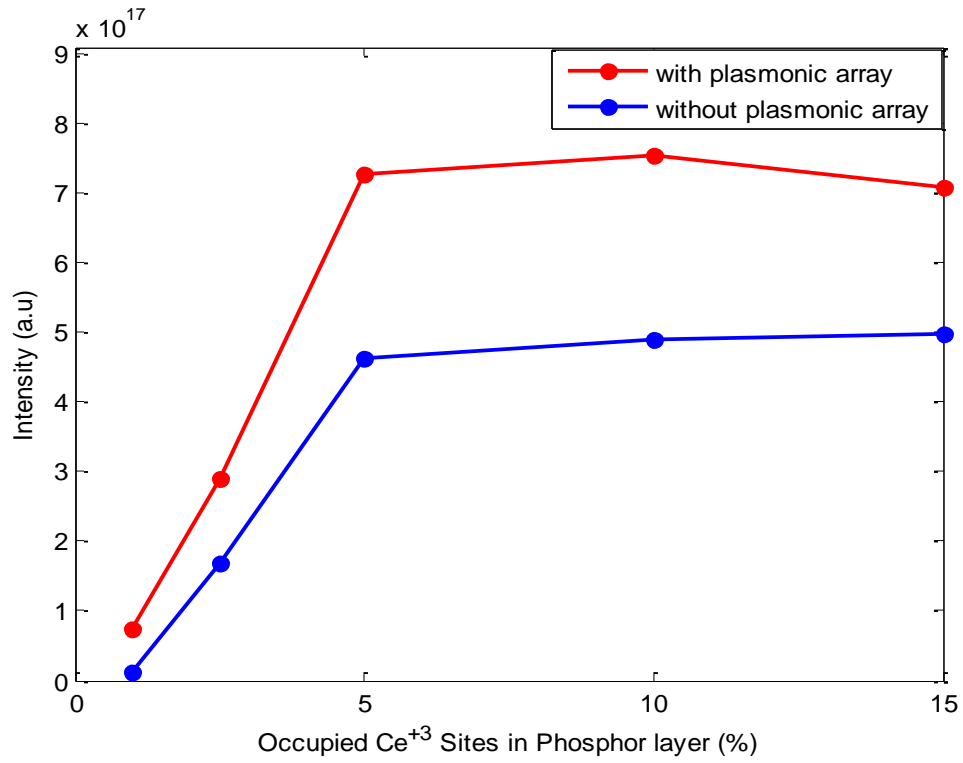


Figure 5.22 Emission Intensity of YAG: Ce^{3+} with and without plasmonic array.

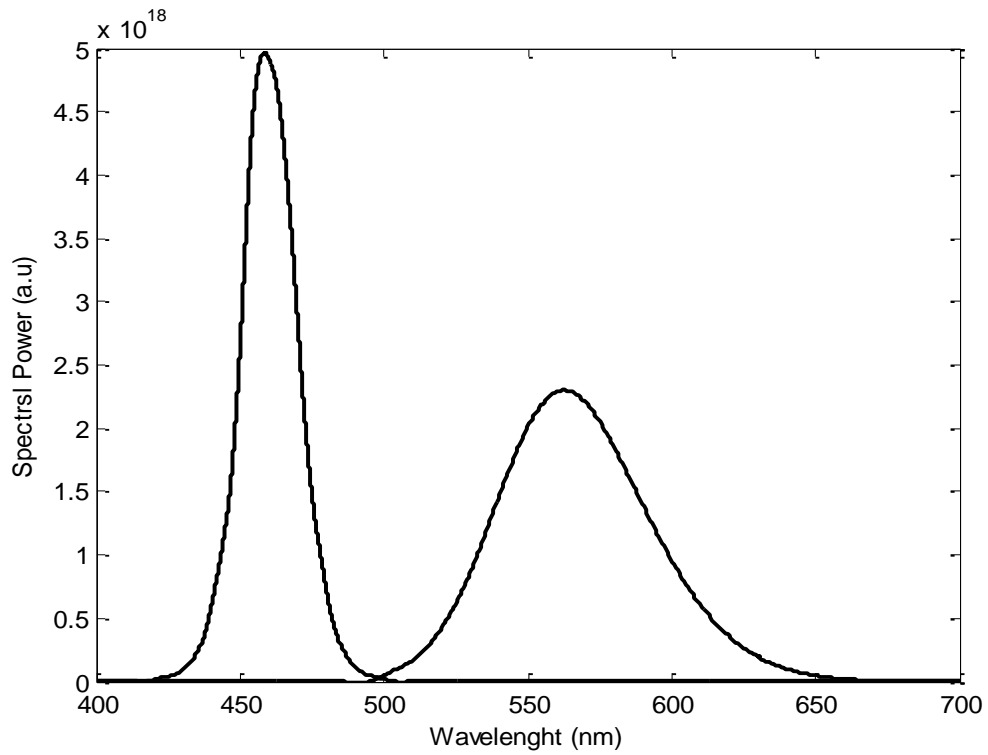


Figure 5.23 Final Output spectrum of white LED without plasmonic array.

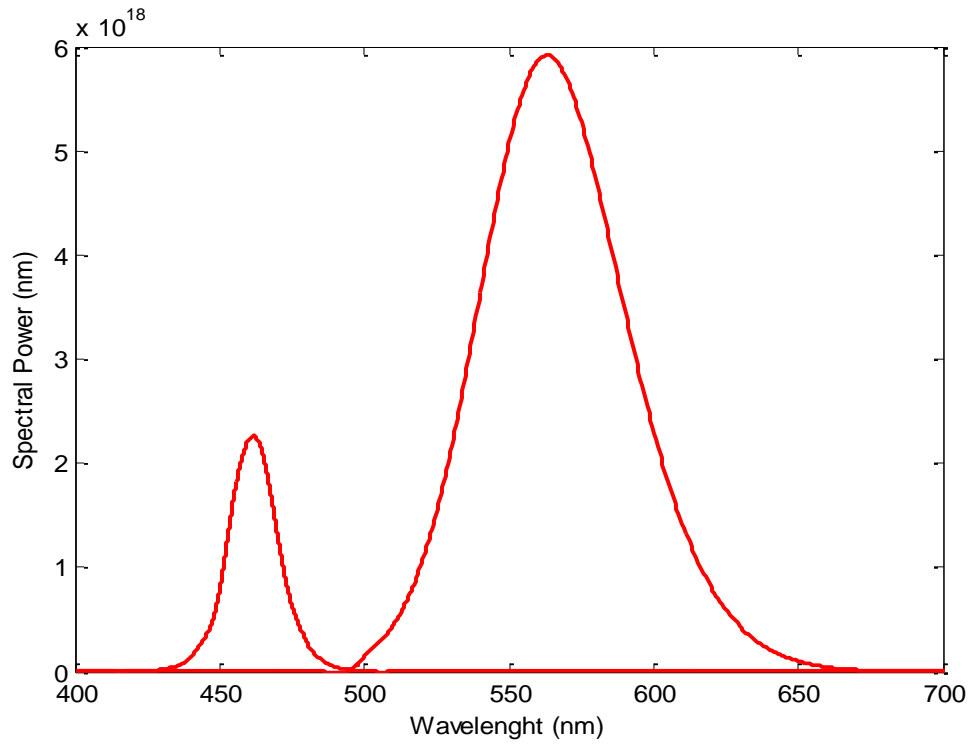


Figure 5.24 Final Output spectrum of white LED with plasmonic array.

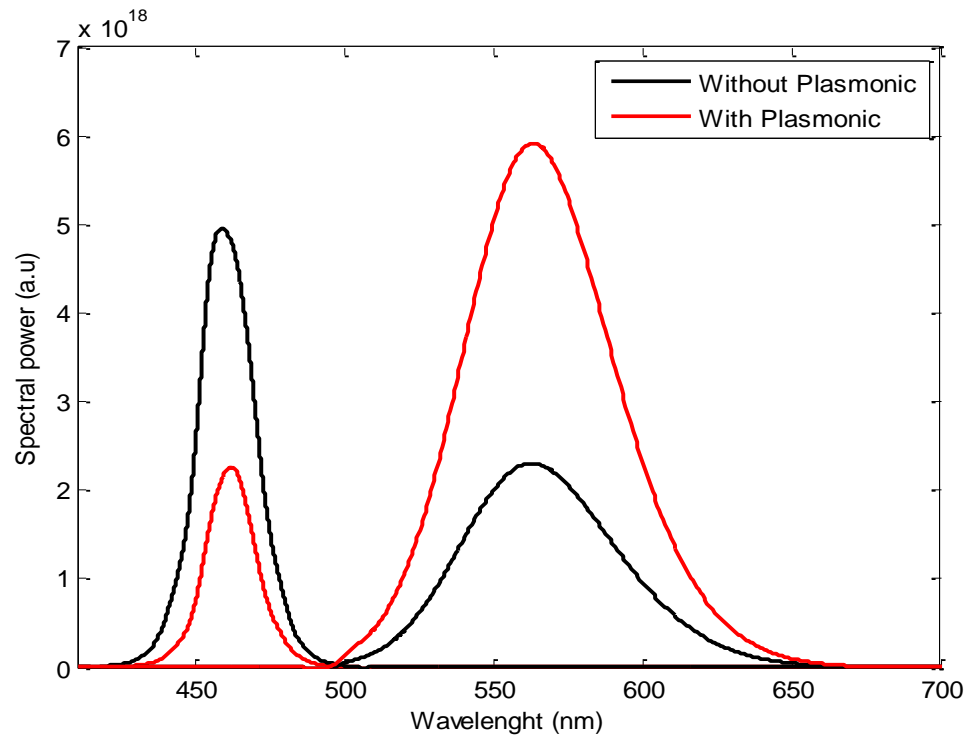


Figure 5.25 Comparison of Final Output spectrum of white LED with and without plasmonic array.

Another configuration was tested for investigating the emission properties of yellow phosphor converted GaN LEDs by coating a layer of polystyrene on the surface of phosphor as shown in. The silver rectangular array was embedded in the polystyrene layer. The optimization of the configuration is needed before investigating the emission properties of the device. The optimization of the device is done in two steps. The first step involves finding the suitable arrangement and parameters of rectangular array with polystyrene as a surrounding medium to resonate at 460 nm. This step is done by determining the scattering properties using TFSF. The second step involves optimizing the thickness of polystyrene (PS) layer so that maximum light is transmitted into air with minimal reflection from the interface. The scattering cross-section of optimized arrangement of rectangular array is shown in the Figure. It is obvious from scattering section that the designed arrangement has resonance at 460 nm.

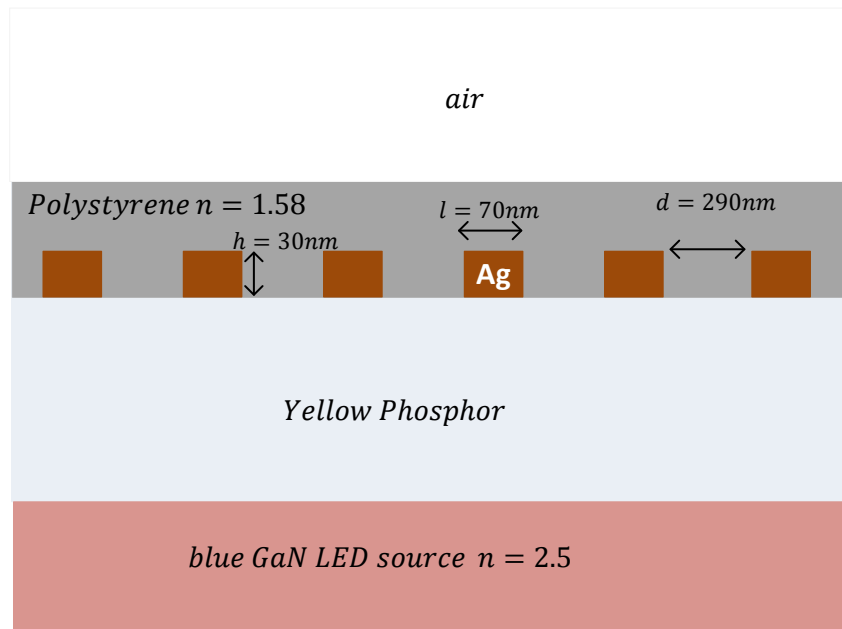


Figure 5.26 Structure of phosphor converted GaN LED coated with metal doped polystyrene layer.

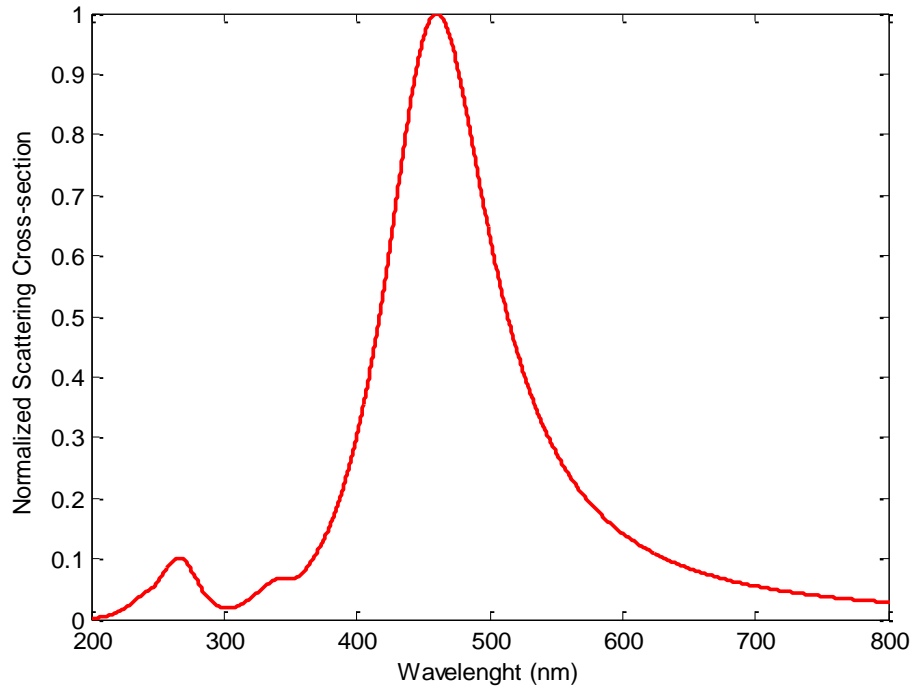


Figure 5.27 Scattering Cross-section of optimized arrangement of silver array in polystyrene media.

In the optimization step of PS layer, the random dipole sources are distributed in the phosphor layer with random phases to calculate the emission power in air with various thickness of PS layer (PS) as shown in Figure 5.28.

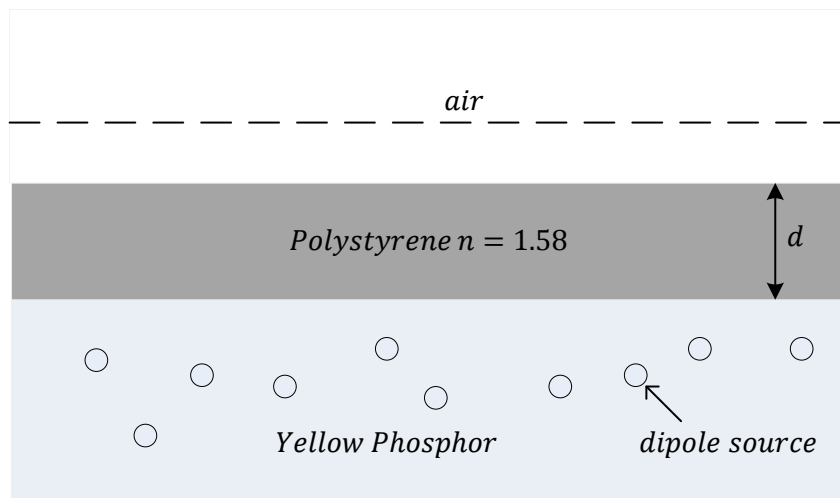


Figure 5.28 Structure for PS thickness (d) optimization.

The spectral emission power calculated in air for various thicknesses is shown in the Figure 5.29. PS layer of 250 nm thickness is used as optimized thickness for phosphor converted white LED configuration.

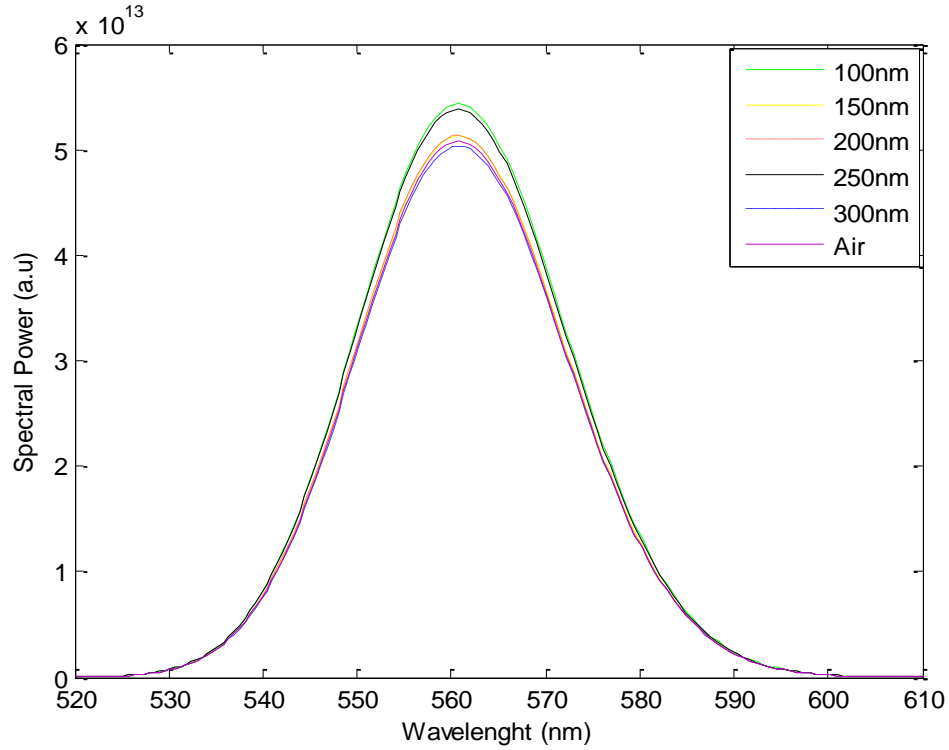


Figure 5.29 Spectral power for different PS thickness (d).

The emission spectral power is calculated for the optimized structure by considering three different cases. In the first case, the emission is determined only in the presence of air as shown in Figure 5.30. In the second case, the emission is calculated in the presence of PS layer as shown in Figure 5.31. It is observed that the PS layer does not affect the conversion process significantly and only facilitates the transmission of light in the air. In the third case, the emission is determined by embedding the silver rectangular array in PS layer as shown in Figure 5.32. The emission is enhanced in this case due to evanescent field that interact with phosphor via localized surface plasmon resonance.

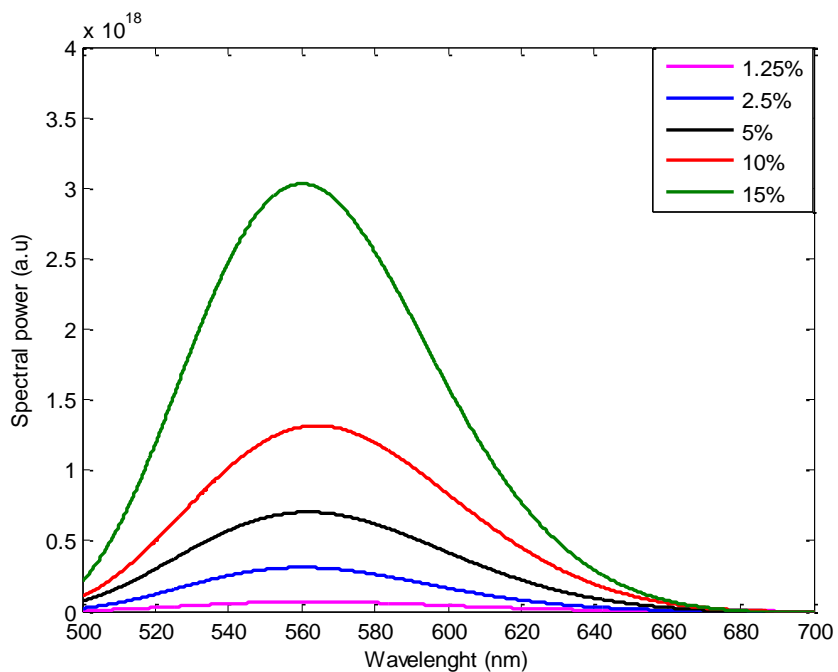


Figure 5.30 Emission Spectrum of YAG: Ce³⁺ without plasmonic array and PS layer.

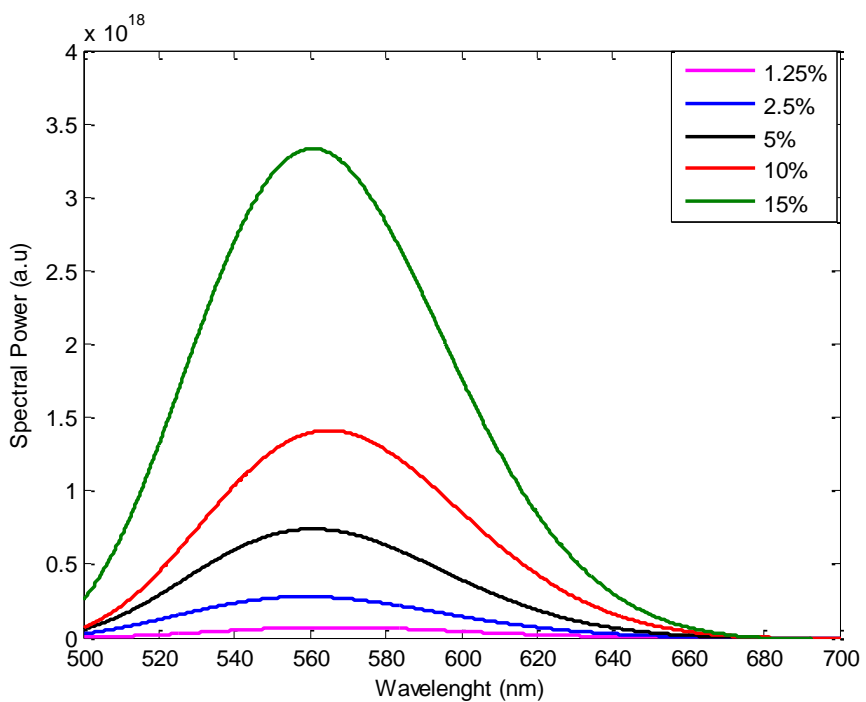


Figure 5.31 Emission Spectrum of YAG: Ce³⁺ with PS layer and no plasmonic array.

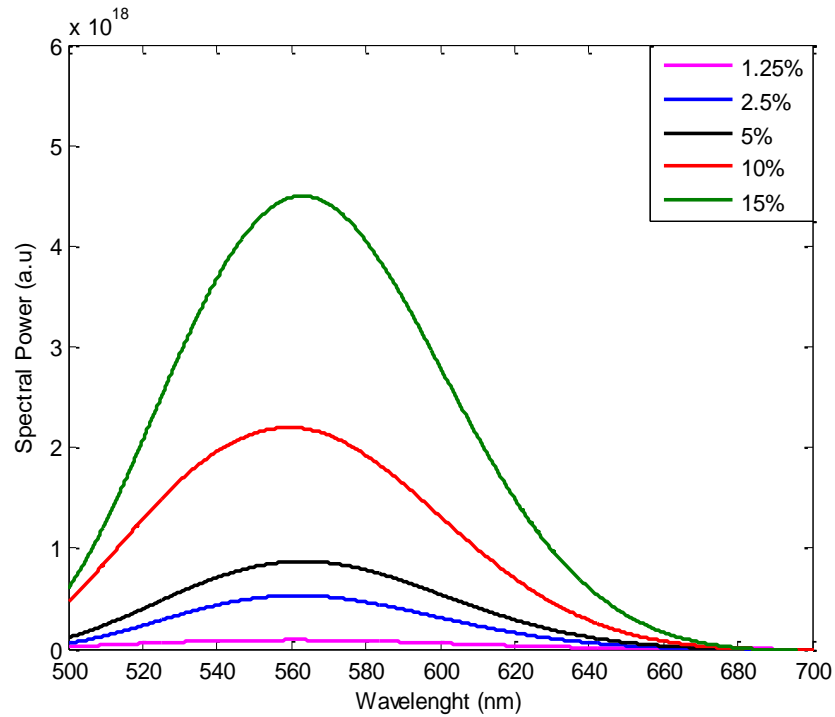


Figure 5.32 Emission Spectrum of YAG: Ce³⁺ with PS layer and plasmonic array.

Then emission properties of the optimized structure as also calculated for all above mentioned three cases with introducing the saturation factor. The spectral power for three cases with saturation effect is shown in Figure 5.33, Figure 5.34 and Figure 5.35 respectively. The saturation density of Ce³⁺ occupied sites is considered 5% for all cases. It is obvious that the emission is constant after the saturation density of Ce³⁺ sites in phosphor medium.

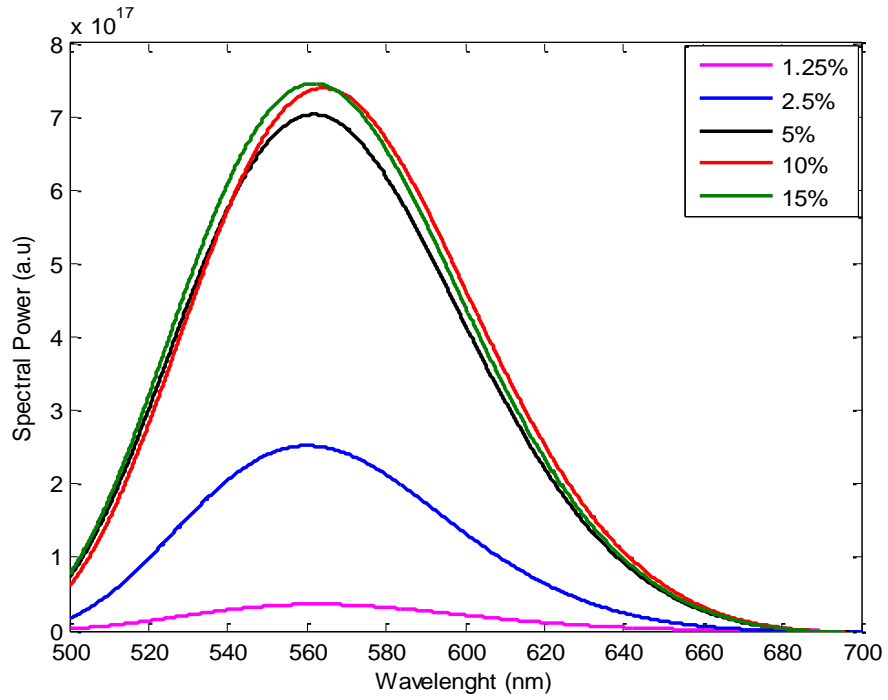


Figure 5.33 Emission Spectrum of YAG: Ce³⁺ with saturation in absence of plasmonic array and PS layer.

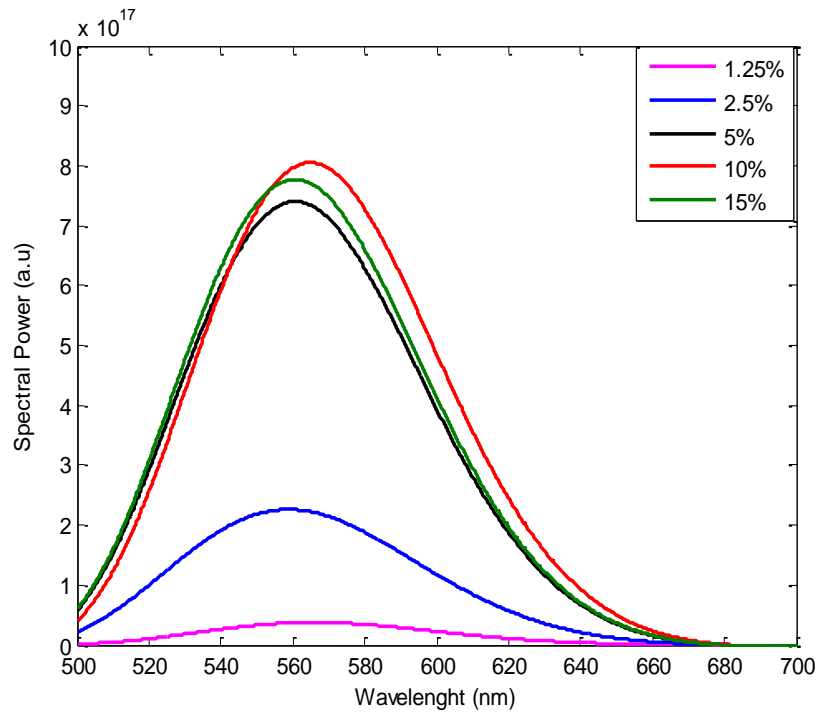


Figure 5.34 Emission Spectrum of YAG: Ce³⁺ with saturation in presence of PS layer and no plasmonic array.

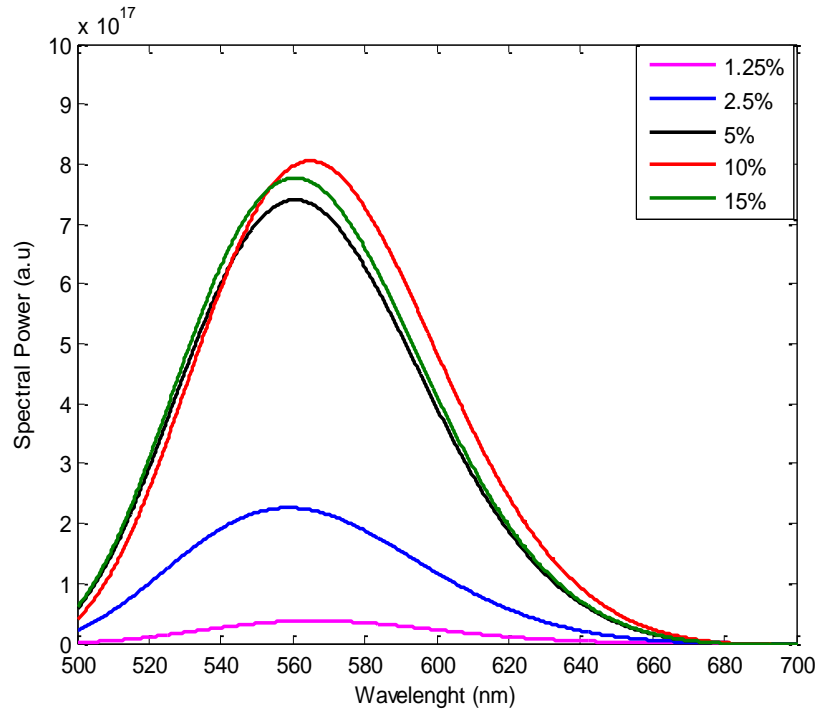


Figure 5.35 Emission Spectrum of YAG: Ce³⁺ with saturation in presence of PS layer and plasmonic array.

The final output of optimized structure for all three cases is shown in Figure 5.36. It is observed that introduction of PS layer acts as a transformer to facilitate the transmission from the phosphor converted LED. It is found that the metal doped PS layer on the surface of phosphor converted LED enhanced the conversion of yellow light due to localized surface plasmonic resonance. At the resonance condition, the localized surface plasmons are generated which interact with phosphor layer near to the interface and population of N₂ is significantly increased which results in enhancement of conversion process in designed configuration as shown in Figure 5.36.

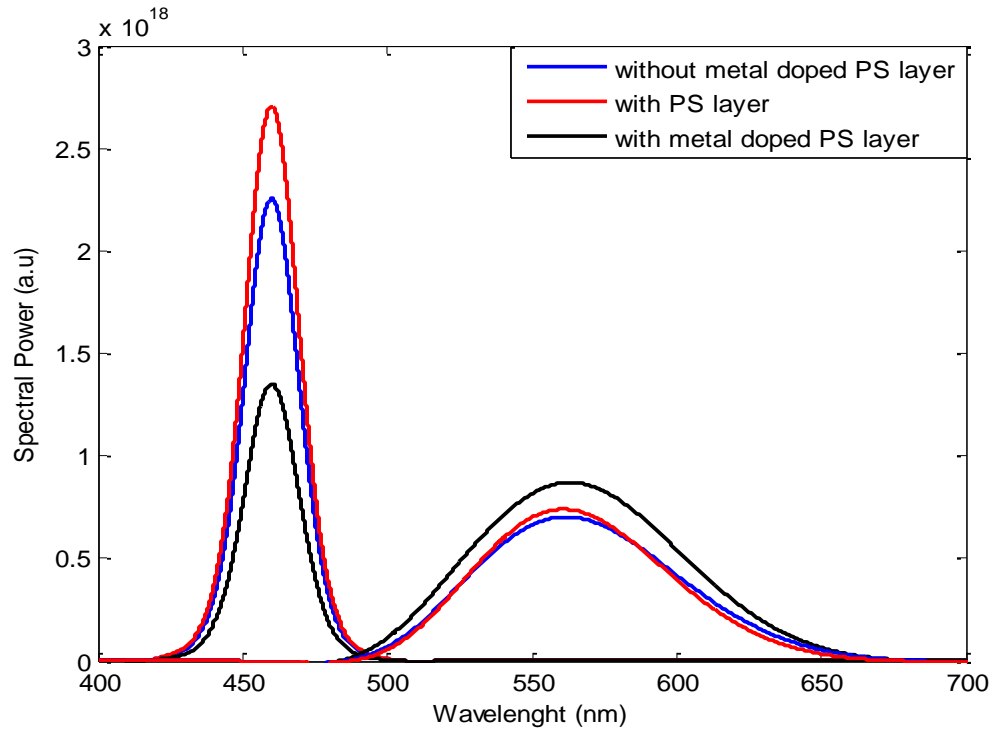


Figure 5.36 Comparison of Final Output spectrum of optimized configuration with metal doped PS layer.

5.5 Summary and Discussion

The metallic nanostructures are investigated to study the enhancement of optical field by matching the resonance condition which depends on the size, shape, dielectric environment of nano-metallic surfaces. The device based on silica particles embedded in silver metallic film shows 10^2 times enhancement due to combined effect of cavity resonance and localized surface plasmon resonance. The other two configurations based on rectangular array integrated with yellow phosphor converted LEDs are optimized to match the resonance condition at 460 nm. It is found that white light conversion is enhanced significantly by embedding the rectangular array in phosphor layer as compared to coated metal doped PS layer on the surface of phosphor converted LED.

CHAPTER 6

CONCLUSIONS AND FUTURE WORK

Phosphor converted white LEDs have been attracting a lot of interest by researchers with ultimate limits of efficiency still not achieved. The modeling of structures and phenomenon associated with white light generation is an important step for further research in solid state lighting technology and meet the current demand of highly efficient white LEDs. Therefore, modeling of electrodynamics of phosphor converted GaN LEDs is presented in this thesis. The overall summary, conclusions and future work is discussed in this chapter.

6.1 Summary

In this thesis, yellow phosphor is considered as wavelength conversion material for white light generation in GaN LEDs. The unique optical characteristics of yellow phosphor are modeled using ADE-FDTD algorithm for phosphor converted GaN LEDs. The work that has been done can be summarized as follows:

- An electromagnetic coupled model that describes the physics behind the wavelength down conversion process using yellow phosphor for white light generation was developed using material specific rate equations.

- The spontaneous emission process of yellow phosphor was modeled by coupling the rate equations with the Maxwell's equations using current density function in the form of random dipole sources.
- ADE-FDTD algorithm was formulated for simulating the yellow phosphor converted GaN LEDs.
- The dispersion of YAG:Ce³⁺ was incorporated using Lorentzian function in general algorithm.
- The linewidth in emission spectrum was introduced using line-shape models in the proposed algorithm. The line-shape models are based on combined contribution of Lorentzian and Gaussian functions.
- The density saturation effect was included on the basis of the density of occupied Ce³⁺ sites in emitting layer using weibull distribution function.
- A device based on an array of silica nanoparticles embedded in the silver metallic film was investigated to study the enhanced field confinement.
- Nano-metallic structures were used to tailor the emission environment of yellow phosphor material to enhance the conversion process. The configuration of plasmonic rectangular array was optimized to resonate at the emission wavelength of GaN LEDs using scattering properties.

- The polystyrene doped with metallic rectangular array based configuration was investigated to enhance the transmission and as well as conversion process in yellow phosphor converted GaN LEDs.

6.2 Conclusions

The conclusion obtained from the simulation results of different proposed configurations for yellow phosphor converted GaN LEDs are as follows:

- The rate equation based electromagnetic model is a powerful tool to represent the electrodynamic of phosphor materials. It also offers fundamental physical insights to improve the performance of phosphor converted white LEDs.
- The strength of spontaneous emission in yellow phosphor mainly depends on the population of energy level N_2 . The variation in population density is considered as a function of wavelength due to discrete nature of energy levels.
- The broadening and asymmetry of final emission spectrum can be attributed to Doppler broadening, collisions broadening and radiation damping defined by Lorentzian and Gaussian line shape function.
- The modeling of spontaneous emission using dipole sources is more realistic due to introduction of randomness in terms of phases and polarization.

- The density of Ce^{3+} is an important factor in determining the emission characteristics of yellow phosphor converted LEDs. The saturation effect can be avoided by considering the optimal value of Ce^{3+} density in yellow phosphor.
- Plasmonic structures can be used to enhance and confine the electromagnetic field by utilizing the combined effect of localized surface plasmons resonance (LSPR) and cavity resonance.
- The white light conversion can be enhanced in yellow phosphor converted GaN using plasmonic rectangular array which change the emission environment of phosphor layer by creating intense electromagnetic field via localized surface plasmon resonance (LSPR).

6.3 Future Work

In this thesis, we have attempted to model the phosphor conversion process using simple ADE-FDTD approach for white light generation in GaN LEDs. The proposed model can be extended and improved in many ways given below:

- The model can be extended by incorporating the electron transition process due to some other dopants in yellow phosphor such as Eu^{3+} in rate equation model which improve the conversion efficiency and lack of red part in the emission spectrum of phosphor converted GaN LEDs

- The model can be improved by investigating the intensity saturation effect as a function of intensity rather than the density of Ce^{3+} sites in yellow phosphor.
- The model can be extended to 3-D domain so that the random polarization in the spontaneous emission process in the model includes both TE and TM waves which give more realistic results.
- The model can also be tested using the random mixing of plasmonic nanoparticles in the phosphor layer for enhanced white light conversion.

References

- [1] M. S. Shur and A. Zukauskas, "Solid-State Lighting: Toward Superior Illumination," *Proc. IEEE*, vol. 93, no. 10, pp. 1691–1703, Oct. 2005.
- [2] S. Pimputkar, J. S. Speck, S. P. DenBaars, and S. Nakamura, "Prospects for LED lighting," *Nat. Photonics*, vol. 3, no. 4, pp. 180–182, Apr. 2009.
- [3] D. A. Steigerwald, J. C. Bhat, D. Collins, R. M. Fletcher, M. O. Holcomb, M. J. Ludowise, P. S. Martin, and S. L. Rudaz, "Illumination with solid state lighting technology," *IEEE J. Sel. Top. Quantum Electron.*, vol. 8, no. 2, pp. 310–320, Mar. 2002.
- [4] J. Brgoch, "Rapid identification of advanced phosphors for solid-state white LEDs," *SPIE Newsroom*, Feb. 2014.
- [5] B. Valeur and M. N. Berberan-Santos, "A Brief History of Fluorescence and Phosphorescence before the Emergence of Quantum Theory," *J. Chem. Educ.*, vol. 88, no. 6, pp. 731–738, Jun. 2011.
- [6] P. Jaffe, "Fluorescence and Phosphorescence," *IEEE Trans. Compon. Parts*, vol. 11, no. 3, pp. 3–7, Sep. 1964.
- [7] R.-J. Xie and N. Hirosaki, "Silicon-based oxynitride and nitride phosphors for white LEDs—A review," *Sci. Technol. Adv. Mater.*, vol. 8, no. 7–8, p. 588, Oct. 2007.
- [8] J. W. M. Verwey and G. Blasse, "Luminescence efficiency of ions with broad-band excitation in lithium lanthanum phosphate glass," *Chem. Mater.*, vol. 2, no. 4, pp. 458–463, Jul. 1990.
- [9] J.-W. Pan and C.-S. Wang, "Light extraction efficiency of GaN-based LED with pyramid texture by using ray path analysis," *Opt. Express*, vol. 20 Suppl 5, pp. A630–640, Sep. 2012.

- [10] F. Bertoluzza, N. Delmonte, and R. Menozzi, "Three-dimensional finite-element thermal simulation of GaN-based HEMTs," *Microelectron. Reliab.*, vol. 49, no. 5, pp. 468–473, May 2009.
- [11] S.-K. Kim, H.-S. Ee, K.-D. Song, and H.-G. Park, "Design of out-coupling structures with metal-dielectric surface relief," *Opt. Express*, vol. 20, no. 15, pp. 17230–17236, Jul. 2012.
- [12] P. Zhu, G. Liu, J. Zhang, and N. Tansu, "FDTD Analysis on Extraction Efficiency of GaN Light-Emitting Diodes With Microsphere Arrays," *J. Disp. Technol.*, vol. 9, no. 5, pp. 317–323, May 2013.
- [13] S. Nakamura, S. Pearton, and G. Fasol, *The Blue Laser Diode: The Complete Story*. Springer, 2000.
- [14] S. Nakamura, T. Mukai, and M. Senoh, "Candela-class high-brightness InGaN/AlGaIn double-heterostructure blue-light-emitting diodes," *Appl. Phys. Lett.*, vol. 64, no. 13, pp. 1687–1689, 1994.
- [15] G. Blasse and A. Bril, "Investigation of Some Ce³⁺-Activated Phosphors," *J. Chem. Phys.*, vol. 47, no. 12, pp. 5139–5145, Dec. 1967.
- [16] W. M. Yen, S. Shionoya, and H. Yamamoto, *Phosphor handbook*. Boca Raton, FL: CRC Press/Taylor and Francis, 2007.
- [17] A. S. Nagra and R. A. York, "FDTD analysis of wave propagation in nonlinear absorbing and gain media," *Antennas Propag. IEEE Trans. On*, vol. 46, no. 3, pp. 334–340, 1998.
- [18] B. Redding, S. Shi, T. Creazzo, and D. W. Prather, "Electromagnetic modeling of active silicon nanocrystal waveguides," *Opt. Express*, vol. 16, no. 12, pp. 8792–8799, 2008.
- [19] S. V. Zhukovsky and D. N. Chigrin, "Numerical modelling of lasing in microstructures," *Phys. Status Solidi B*, vol. 244, no. 10, pp. 3515–3527, Oct. 2007.

- [20] G. M. Slavcheva, J. M. Arnold, and R. W. Ziolkowski, "FDTD Simulation of the Nonlinear Gain Dynamics in Active Optical Waveguides and Semiconductor Microcavities," *IEEE J. Sel. Top. Quantum Electron.*, vol. 10, no. 5, pp. 1052–1062, Sep. 2004.
- [21] P. Song and C. Jiang, "Modeling of downconverter based on Pr^{3+} - Yb^{3+} codoped fluoride glasses to improve sc-Si solar cells efficiency," *AIP Adv.*, vol. 2, no. 4, p. 042130, 2012.
- [22] K. Ishida, I. Mitsuishi, Y. Hattori, and S. Nunoue, "Numerical Simulation on Light Output of UV-based White Light-Emitting Diodes with Multicolor Phosphor Blends," *Appl. Phys. Express*, vol. 1, p. 082201, Jul. 2008.
- [23] C. Jiang and W. Xu, "Modeling Multiple Rare Earth-Doped System for White Light Generation," *J. Disp. Technol.*, vol. 5, no. 12, pp. 431–437, Dec. 2009.
- [24] C. Jiang and W. Xu, "Theoretical Model of Yb^{3+} - Er^{3+} - Tm^{3+} -Codoped System for White Light Generation," *J. Disp. Technol.*, vol. 5, no. 8, pp. 312–318, Aug. 2009.
- [25] R. Hu, X. Luo, H. Zheng, and S. Liu, "Optical constants study of YAG:Ce phosphor layer blended with SiO_2 particles by Mie theory for white light-emitting diode package," *Front. Optoelectron.*, vol. 5, no. 2, pp. 138–146, Jun. 2012.
- [26] Z. Liu, S. Liu, K. Wang, and X. Luo, "Measurement and numerical studies of optical properties of YAG: Ce phosphor for white light-emitting diode packaging," *Appl. Opt.*, vol. 49, no. 2, pp. 247–257, 2010.
- [27] K. Saxena, V. K. Jain, and D. S. Mehta, "A review on the light extraction techniques in organic electroluminescent devices," *Opt. Mater.*, vol. 32, no. 1, pp. 221–233, Nov. 2009.
- [28] N. Gao, K. Huang, J. Li, S. Li, X. Yang, and J. Kang, "Surface-plasmon-enhanced deep-UV light emitting diodes based on AlGaIn multi-quantum wells," *Sci. Rep.*, vol. 2, Nov. 2012.

- [29] G. Lozano, D. J. Louwers, S. R. Rodríguez, S. Murai, O. T. Jansen, M. A. Verschuuren, and J. Gómez Rivas, "Plasmonics for solid-state lighting: enhanced excitation and directional emission of highly efficient light sources," *Light Sci. Appl.*, vol. 2, no. 5, p. e66, May 2013.
- [30] S. Dang, C. Li, W. Jia, Z. Zhang, T. Li, P. Han, and B. Xu, "Improvement of light extraction efficiency of GaN-based light-emitting diodes using Ag nanostructure and indium tin oxide grating," *Opt. Express*, vol. 20, no. 21, pp. 23290–23299, 2012.
- [31] S. Fujita, A. Sakamoto, and S. Tanabe, "Luminescence Characteristics of YAG Glass-Ceramic Phosphor for White LED," *IEEE J. Sel. Top. Quantum Electron.*, vol. 14, no. 5, pp. 1387–1391, 2008.
- [32] R. Hansel, S. Allison, and G. Walker, "Temperature-dependent luminescence of gallium-substituted YAG:Ce," *J. Mater. Sci.*, vol. 45, no. 1, pp. 146–150, Jan. 2010.
- [33] P. F. Smet, A. B. Parmentier, and D. Poelman, "Selecting Conversion Phosphors for White Light-Emitting Diodes," *J. Electrochem. Soc.*, vol. 158, no. 6, pp. R37–R54, Jun. 2011.
- [34] A. D. Rakic, A. B. Djuricic, J. M. Elazar, and M. L. Majewski, "Optical properties of metallic films for vertical-cavity optoelectronic devices," *Appl. Opt.*, vol. 37, no. 22, pp. 5271–5283, Aug. 1998.
- [35] K. S. Yee, "Numerical solution of initial boundary value problems involving Maxwell's equations in isotropic media," *IEEE Trans Antennas Propag.*, pp. 302–307, 1966.
- [36] A. Taflove and S. C. Hagness, *Computational Electrodynamics: The Finite-Difference Time-Domain Method*. Artech House, Incorporated, 2005.

- [37] M. A. Alsunaidi and A. A. Al-Jabr, "A General ADE-FDTD Algorithm for the Simulation of Dispersive Structures," *IEEE Photonics Technol. Lett.*, vol. 21, no. 12, pp. 817–819, Jun. 2009.
- [38] Y. Zorenko, T. Voznyak, V. Gorbenko, E. Zych, S. Nizankovski, A. Dan'ko, and V. Puzikov, "Luminescence properties of $Y_3Al_5O_{12}:Ce$ nanoceramics," *J. Lumin.*, vol. 131, no. 1, pp. 17–21, Jan. 2011.
- [39] H. H. Telle, A. G. Ureña, and R. J. Donovan, *Laser Chemistry: Spectroscopy, Dynamics and Applications*. John Wiley & Sons, 2007.
- [40] H. Rinne, *The Weibull Distribution: A Handbook*. CRC Press, 2010.
- [41] P. Mühlischlegel, H.-J. Eisler, O. J. F. Martin, B. Hecht, and D. W. Pohl, "Resonant Optical Antennas," *Science*, vol. 308, no. 5728, pp. 1607–1609, Jun. 2005.
- [42] R. Marty, G. Baffou, A. Arbouet, C. Girard, and R. Quidant, "Charge distribution induced inside complex plasmonic nanoparticles," *Opt. Express*, vol. 18, no. 3, pp. 3035–3044, Feb. 2010.
- [43] T. Søndergaard, S. I. Bozhevolnyi, J. Beermann, S. M. Novikov, E. Devaux, and T. W. Ebbesen, "Resonant Plasmon Nanofocusing by Closed Tapered Gaps," *Nano Lett.*, vol. 10, no. 1, pp. 291–295, Jan. 2010.
- [44] W. W. Ahmed and M. A. Alsunaidi, "Plasmonic cavities for enhanced optical confinement," in *Electronics, Communications and Photonics Conference (SIECPC), 2013 Saudi International, 2013*, pp. 1–3.
- [45] C. F. Bohren and D. R. Huffman, *Absorption and Scattering of Light by Small Particles*. John Wiley & Sons, 2008.

Vitae

Name : Waqas Waseem Ahmed

Nationality : Pakistani

Date of Birth : 8/3/1987

Email : waqas.waseem291@gmail.com

Address : 12-G Shahjamal , Lahore, Pakistan

Academic Background : BS in Electronic Engineering (2009), GIKI, Pakistan

: MS in Electrical Engineering (2014), KFUPM, KSA

Publications

- (Invited) **W.W. Ahmed**, M. T. Mujahid, M. Ziaullahkhan and M. A. Alsunaidi, “Light extraction enhancement of GaN Light emitting diodes,” 2nd IEEE International Conference on Electronics, Communication, and Photonics (SIECPC), Riyadh, Saudi Arabia, April 2013.
- **W.W. Ahmed** and M. A. Alsunaidi, “Plasmonic Cavities for Enhanced optical Confinement,” 2nd IEEE International Conference on Electronics, Communication, and Photonics (SIECPC), Riyadh, Saudi Arabia, April 2013.

- M.T.M. Mujahid, **W.W. Ahmed** and M. A. Alsunaidi, “Sensing Properties of Plasmonic Ring Resonators,” 2nd IEEE International Conference on Electronics, Communication, and Photonics (SIECPC), Riyadh, Saudi Arabia, April 2013.
- **W.W. Ahmed**, M. T. Mujahid and M. A. Alsunaidi, “Enhanced Optical Confinement using an Array of Silica Nanoparticles Embedded in Ag Metallic Film,” 4th International conference on Metamaterials, Photonic Crystals and Plasmonics (META’13), Sharjah, UAE, March 2013.